Universidad de Navarra

Facultad de Ciencias

Effect of External Fields on the Dynamics of Colloidal Phase Transitions

Moorthi Pichumani

Universidad de Navarra

School of Science

Effect of External Fields on the Dynamics of Colloidal Phase Transitions

Submitted by **Moorthi Pichumani** in partial fulfillment of the requirements for the Doctoral Degree of the University of Navarra

This dissertation has been written under my supervision in the Doctoral Program in Complex Systems, and I approve its submission to the Defense Committee.

Signed on September 12, 2012

Dr. Wenceslao González–Viñas

Declaración:

Por la presente yo, **D. Moorthi Pichumani**, declaro que esta tesis es fruto de mi propio trabajo y que en mi conocimiento, no contiene ni material previamente publicado o escrito por otra persona, ni material que sustancialmente haya formado parte de los requerimientos para obtener cualquier otro título en cualquier centro de educación superior, excepto en los lugares del texto en los que se ha hecho referencia explícita a la fuente de la información.

(I hereby declare that this submission is my own work and that, to the best of my knowledge and belief, it contains no material previously published or written by another person nor material which to a substantial extent has been accepted for the award of any other degree of the university or other institute of higher learning, except where due acknowledgment has been made in the text.)

De igual manera, autorizo al Departamento de Física y Matemática Aplicada de la Universidad de Navarra, la distribución de esta tesis y, si procede, de la "fe de erratas" correspondiente por cualquier medio, sin perjuicio de los derechos de propiedad intelectual que me corresponden.

Signed on September 12, 2012

Moorthi Pichumani

To my Supervisor...

Acknowledgements

Contents

Preface

Crystals – Highly ordered array of repeating sub-units that can be extended to three dimensions. The repeating sub-units can be atoms, molecules or ions. Colloidal crystals are analogous to these *"typical"* crystals, where the repeating units are colloidal particles. Spacing between the identical units can be varied during the crystallization process. Different reasons make the colloidal crystals to be interesting to the scientific community. First of all, the colloidal particles mimic the atomic systems that constitute the basic unit of the matter and thus the colloids can model atomic crystals and glasses. Secondly, highly ordered two dimensional and three dimensional arrays of colloidal particles behave like photonic crystals that can influence the propagation of light. Consequently, the colloidal crystals are good choice of materials in optoelectronics and photonics. A naturally available opal can be considered as an example. Fabrication of photonic band gap materials by simple methods is still under rigorous exploration. Thirdly, the self-assembly mode that these colloidal crystals prefer to follow during their crystallization. The fundamental interparticle interactions, the hydrodynamics and the thermodynamics play a major role during the self-assembly process.

Evaporation induced self-assembly of colloidal particles from stable colloidal dispersions is simple to follow. As a result of phase transition (from liquid phase to solid phase), colloidal deposits are obtained. A critical parameter involved in this phase transition is the time scale at which the transition is occurring; either the liquid phase may transform to a solid phase slowly or the liquid phase can transform to a solid state quickly. In another terms, the rate at which the continuous phase is withdrawn from the dispersion determines the structure. Under close–to–thermal equilibrium, well-ordered colloidal particles can be obtained if the fluid is evaporating slowly from the dispersion (by just allowing a volume of dispersion to evaporate). *Will it be possible to control the final structure of these drying colloids?* Far–from–equilibrium phase transition allows us to tune the final structures by applying the external forces; however, the mechanisms due to the applied forces with the colloidal system are complex to understand. This Thesis investigates the non equilibrium phase transition in the colloidal system of varying properties and nature under the action of applied forces.

The state of the system may become unstable when external forces are applied. The external force can come from a thermal gradient, an electric field, a magnetic field, gravity or rotation, etc.. Here, we apply a force when the colloidal dispersion undergoes a phase transition (from liquid phase to solid phase). In the fist part of the Thesis, the experiments are performed in such a way that the liquid phase is getting transformed to solid phase at a slow rate (evaporation of the continuous phase is slow). We use vertical deposition, a conceptually derived technique from the Langmuir–Blodgett method. The aqueous based dilute colloidal dispersion of polystyrene

particles is allowed to evaporate in an environment of controlled temperature and humidity. External electric fields are applied when the dispersion undergoes the phase transition and the meniscus region is observed. *What are the consequences of the applied electric field to the colloidal system? and why the meniscus region is given attention?* The impact of the electric fields on the colloidal dispersion is studied by correlating the final morphology of colloidal particles with the speed of receding contact line and experimental initial conditions. *Is the existence of a free surface important to consider?* To account this, the above experimental method is simplified (by minimizing the evaporation of the fluid, hence, having a static contact line) to explore the effect of free surface in the colloidal systems while an alternating electric field is applied.

In the second part of the Thesis, the experiments are performed in such a way that the fluid phase is made to evaporate very fast by pipetting a volume of dispersion onto a rapidly spinning substrate (spin-coating method). Spin-coating of concentrate colloidal dispersion provides compact structures (polycrystalline deposits) where the microscopic domains are orientationally correlated (domains arranged in radial orientational registry) due to the axial symmetry from the spin-coating. *How to break this axial symmetry and why to break it?* External alternating electric fields are applied (field direction is stationary in the rotating frame) when the dispersion is pipetted onto the spinning substrate. This may break the axial symmetry imposed by the spin-coating. *How are the compact structures formed in the spin-coated colloids?* It is difficult to understand the mechanisms behind the formation of compact structures in the spin-coating of concentrate colloids. Agglomeration and clustering dynamics are more relevant to understand the structure formation. To investigate this, dilute superparamagnetic colloids are spin-coated under the action of an applied magnetic field. The characterization of the clusters of superparamagnetic particles may help in understanding the structure formation.

External field induced deposition of particles will advance the self assembly process to next level where the multiple-scale structured materials can be fabricated in a straightforward manner. Hence, these contemporary methods could improve the materials that are necessary for the technological applications in an inexpensive way. Consequently, the modern technology will be at a reachable distance to all kinds of people and it will be accessible irrespective of their economic situations.

Regarding the presentation of the Thesis, the subject of study and the related concepts are introduced in the first Chapter. In the second Chapter, experiment methods and procedures for vertical deposition are outlined. The results from the vertical deposition experiments are presented and discussed in the third Chapter. The second part of the Thesis focuses on the spin-coating method. Chapter four introduces the various experimental techniques related to the spin-coating and the results are explained in the fifth Chapter. Finally, the conclusions and the outlook summarize the attained objectives and outline the further studies which can be carried out in the future.

Chapter 1

Introduction

1.1. Langmuir–Blodgett films

A Langmuir–Blodgett (LB) film is obtained when a solid surface is immersed into an aqueous solution of molecules or particles which are, at least partially on the surface. By increasing the surface partial pressure, monolayers are obtained. Subsequently, the monolayer present on the surface of the solution is thus deposited onto a solid surface [1–3]. This process can be repeated many times to get multilayers (fig. 1.1). Langmuir–Blodgett method was employed to fabricate monolayers of materials that finds various applications as reported in [4–6]. In particular, this method was widely used with colloidal dispersions to obtain monolayers and multilayers of colloidal particles [7–13]. Massé *et al.* showed the formation of three dimensional colloidal crystals of well-defined thickness and organization using functionalized silica particles. Also, they demonstrated the multilayer colloidal crystal formation using particles of different size. A schematic representation is shown in fig. 1.2. In this kind of system, the quality of the crystals depends on the surface pressure, the temperature, the surface tension at which the film is formed, and the rate at which the substrates are immersed and pulled out.
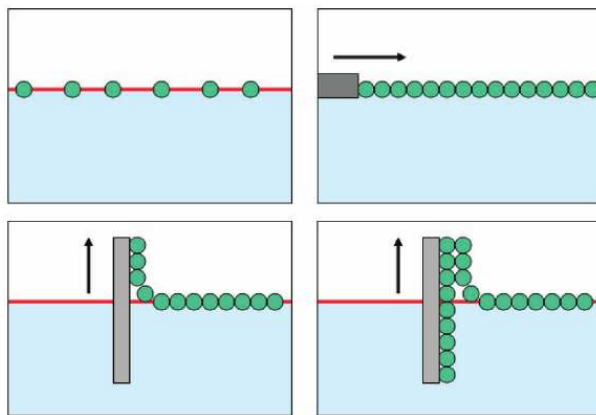
Figure 1.1: Multilayers formation during the LB deposition process. Figure reprinted from [7].

Dip-coating is a technique conceptually similar to LB method, where the surface pressure of the solution may not be controlled. In this technique, the substrate is immersed in a solution
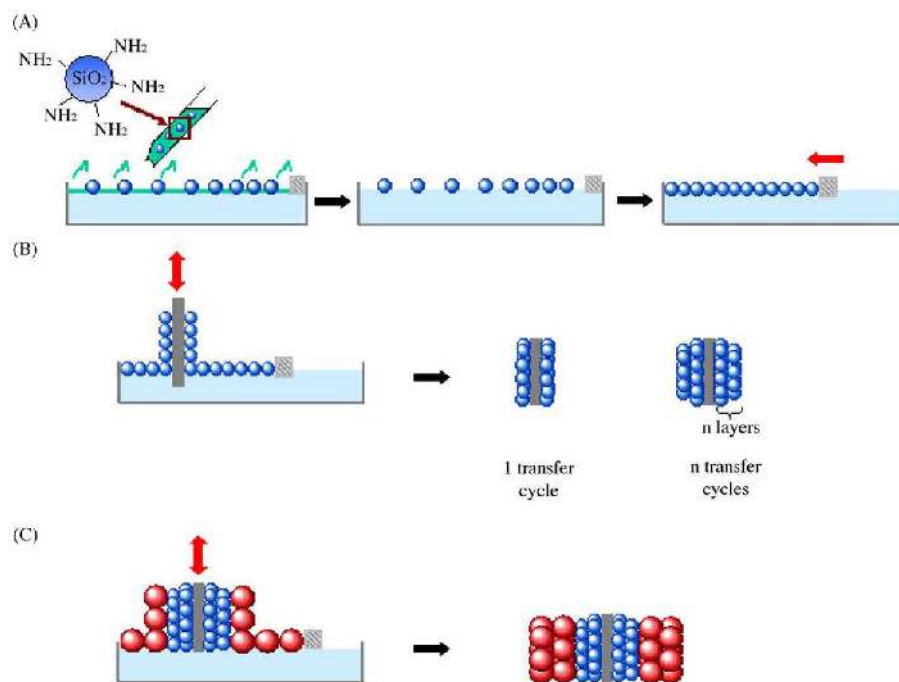
Figure 1.2: Schematic representation of: (A) the formation of a close-packed two-dimensional film of silica particles at the gas/liquid interface; (B) the elaboration of a colloidal crystal through the transfer of the 2D film onto a solid substrate; (C) the elaboration of a multilayer colloidal crystal through the successive transfers of silica particles of different size. Figure reprinted from [11].
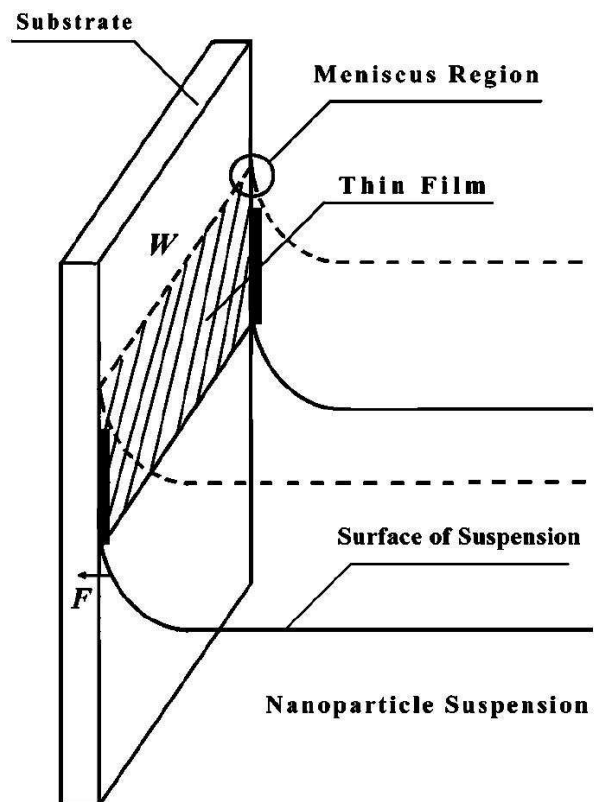
Figure 1.3: Schematic representation of vertical colloidal deposition. The substrate is immersed vertically into the dispersion, and as the surface of the dispersion is lowered, the particles in meniscus region aggregate on the substrate. Diao *et al.* [14] used dispersions with nanoparticles for deposition. Figure reprinted from [14].

of the coating material and then it is pulled. Vertical deposition (VD) of colloids [8, 14–21] is also a technique conceptually derived from LB method where the colloidal particles are deposited onto the substrate that is placed vertically. Compared to the LB method and dip-coating, in VD technique, the substrate remains stationary and the particles are deposited as the fluid phase gets evaporated. The evaporation-driven deposition of particles hence results in colloidal crystals whose thickness and quality can be controlled [8, 15, 16, 21]. A schematic picture of the vertical deposition of colloids is shown in fig. 1.3. The substrate is immersed vertically into the colloidal dispersion. When the fluid phase evaporates, the surface of the dispersion is lowered (see fig. 1.3 dotted lines). The particles in the meniscus region aggregate on the substrate. Dimitrov *et al.* [15] used a similar technique to grow fine particle arrays on the smooth and wettable solid surfaces. They obtained centimeter-size polycrystalline monolayer films that consist of closely packed particles. In relating the LB method and VD technique, sketch of the particle and water fluxes in the vicinity of the monolayer particle arrays growing on a vertical substrate is shown in fig. 1.4. The substrate is withdrawn from the dispersion, like the methods shown in fig. 1.1 and fig. 1.2. The evaporation of the fluid from the wetting film generates an inward flux. The evaporated fluid is replenished by an inward flow of dispersion from the bulk (see fig. 1.3 for meniscus region and fig. 1.4 for flux components.) This inward flux consists of a fluid flux component j_w and of a particle flux component j_p. j_w compensates for the fluid that evaporated from the film j_e (see fig. 1.4 for j_w, j_p and j_e) and the j_p causes the particles to accumulate which then form compact structures (see fig. 1.5).

Pieranski *et al.* [22] and Murray *et al.* [23] suggested that the electrostatic forces are responsible for the interactions between the particles that are confined in thin films which then form compact structures (2D arrays of particles). Later, investigations show that the lateral capillary forces [24–30] are able to gather the particles to form layers. Brief representation of different types of capillary forces are shown in fig. 1.6. Each individual particle causes some perturbation in the shape of a liquid interface. If we consider the system of two particles (see fig. 1.6), the perturbation from individual particle overlaps with the neighborhood and forms menisci. This gives rise to a lateral capillary force between the particles (see b, c, d and e in fig. 1.6). The force could be either attractive or repulsive depending on the geometry of the menisci around the two particles. The particles aggregate where the lateral capillary forces are attractive. Successive monolayers and multilayers can be formed as the particle flux j_p fills up the space between the substrate and the film surface (see fig. 1.4). This space is beneath the meniscus region and is termed as particle pool zone (PPZ) [19] which will be explained in the following.

Shimmin *et al.* [8] reported results based on the experiments performed by vertical deposition technique. In their experiments, a vertical substrate was immersed in the aqueous colloidal dispersion. The dispersion was allowed to evaporate (experiments were performed at 45°C) and they controlled the evaporation rate of the solvent by adding the solvent (water) in the bottom of the colloidal dispersion. They showed that the formed colloidal crystals depend on the particles that accumulate close to the solvent-air interface (a region near the free surface). Recently, Giuliani *et al.* [19] investigated the region (particle pool zone, PPZ) and they correlated it with the morphology of the structures deposited on the substrate. They used dilute aqueous colloidal dispersion of polystyrene particles. When the evaporation was favored (in their case, the experiments were performed at 63°C) the solvent got evaporated and the contact line receded. They explained the relevance in the speed of the receding contact line with the obtained deposits
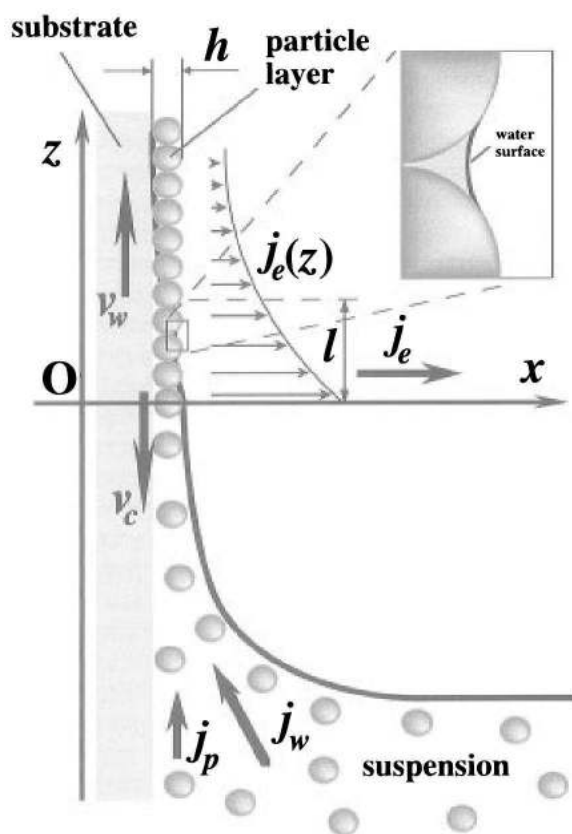
Figure 1.4: Sketch of the particle and water fluxes in the vicinity of monolayer particle arrays growing on a substrate that is being withdrawn from the dispersion. The inset shows the meniscus shape between neighboring particles. Here, v_w is the substrate withdrawal rate, v_c is the array growth rate, j_w is the water influx, j_p is the respective particle influx, j_e is the water evaporation flux, and h is the thickness of the array. Figure reprinted from [15].
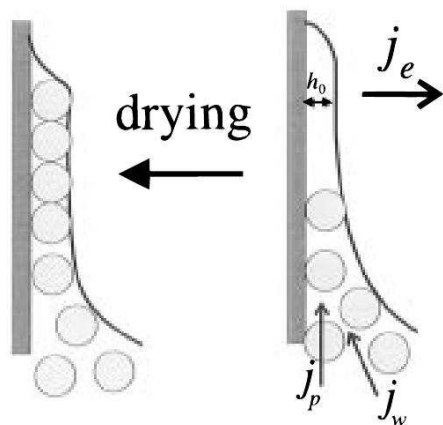
Figure 1.5: Particle array formation in a wetting film. The particle diameter is slightly larger than the wetting film thickness h_0. The fluid evaporation from the film causes inward flux in the dispersion from the bulk towards the film. The particle arrays are thus initiated and their growth may continue. See fig. 1.4 for flux components. Figure reprinted from [15].
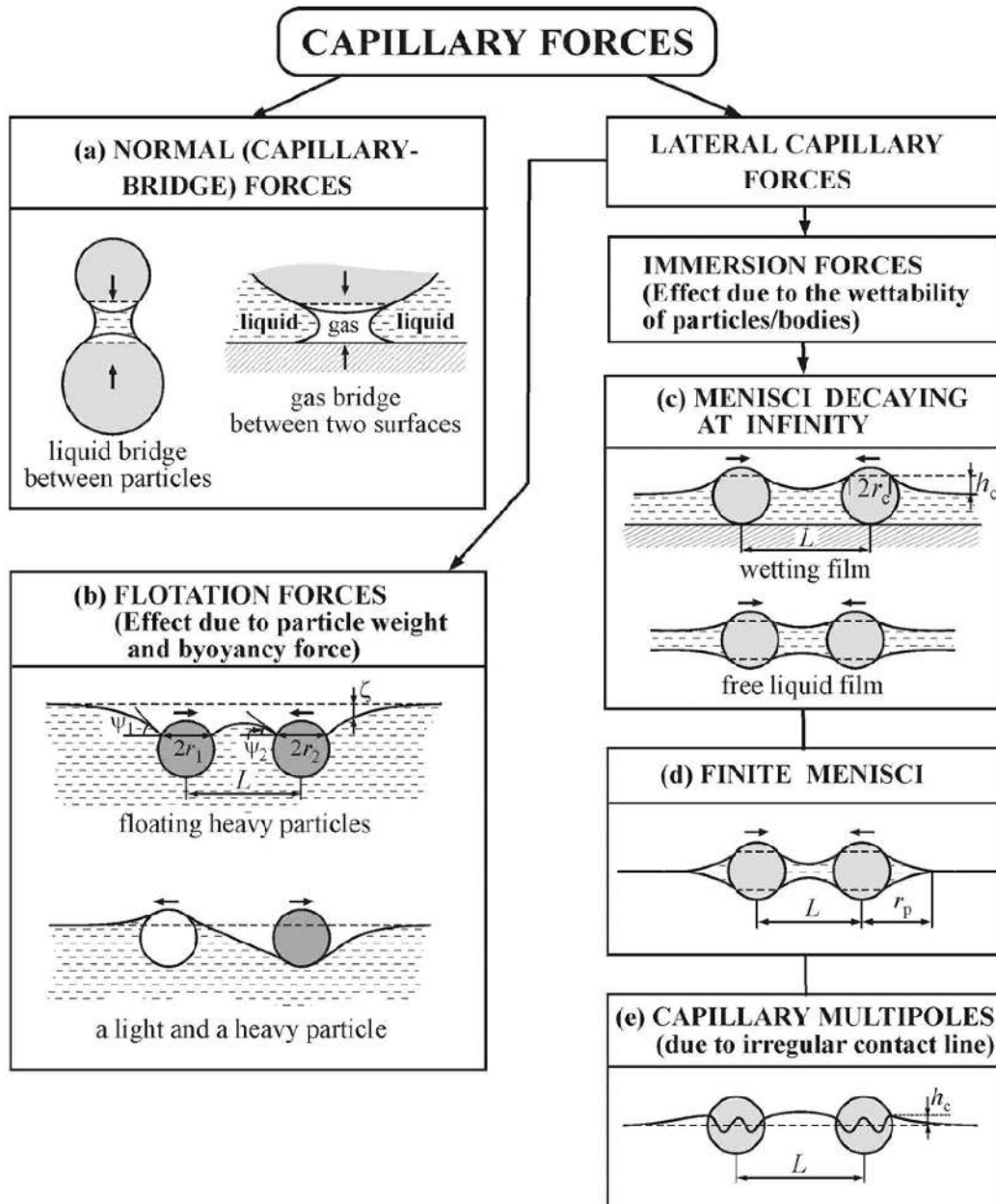
Figure 1.6: Brief representation of the different types of capillary forces: (a) Normal capillary force; (b, c, d and e) The lateral capillary forces that consider the (i) particle weight and buoyancy (see b) (ii) immersion forces, position of the contact line, shape of the contact line, and magnitude of the contact angle (see c, d and e). Figure reprinted from [30].

of colloidal particles through PPZ. The report [19] suggests that the PPZ plays an important role in supplying the particles for deposition. Within their experimental resolution, they distinguished two kinds of contact line speed which correspond to different types of morphology. Shimmin *et al.* [8] and Giuliani *et al.* [19] suggested the importance of PPZ (solvent-air interface) to the forming colloidal deposits. Influencing the PPZ has great advantage as it is directly related with the supply of particles for deposition. The PPZ depends on the initial concentration of the colloidal dispersion. Our motivation in the experiments is to control the PPZ and consequently the morphology of the colloidal particles in the dried deposit. We performed vertical deposition experiments with applied weak DC electric fields. We use water based dilute colloidal dispersion where the polystyrene particles are negatively charged (section 2.2.1). We measure the speed of the receding contact line while the external field is applied. The results are explained (see chapter 3) through the role of PPZ with electric fields and the types of morphology of colloidal particles (section 3.2). In the following, effects of electric fields to the colloidal system are presented.

1.2.   Physical interactions in colloids

Physical interactions in the colloidal system are caused by forces of gravity, electrostatic, electric dipolar, magnetic dipolar and hydrodynamics. Controlling the interactions by applying external fields changes the equilibrium state of the stable colloidal system through influencing the entropy and the energetics in the colloidal free energy [31]. A summary of the colloidal interactions and its physical effects are shown in table 1.1. Parameters used are the electron charge e, the ion valency z, the ion concentration in the bulk c_0^*, the viscosity of the fluid η_f, the shear rate $\dot{\gamma}$, the electric field strength E_0, the particle and the fluid dielectric constant ε_p and ε_f, respectively, the dielectric mismatch parameter $\beta = \frac{-1+\frac{\varepsilon_p}{\varepsilon_f}}{2+\frac{\varepsilon_p}{\varepsilon_f}}$, the particle-fluid density mismatch $\Delta\rho = (\rho_p - \rho_f)$, the particle radius a and the acceleration of the gravity g.

In our experiments, the major interactions in the colloidal system are between the fluid flows, particles in the dispersion and the external field. Relevant dimensionless numbers to our experimental conditions can be estimated. The estimated order of magnitude for these numbers in similar experimental conditions is obtained from [32] and presented in the following as well as in the chapters 3 and 5.

Reynolds number: Reynolds number is the ratio of the inertial forces to the viscous ones. It considers the fluid properties like density, viscosity and the characteristic length.

$$Re \sim \frac{\rho V L}{\mu} \tag{1.1}$$

where ρ and μ are the density and dynamic viscosity of the fluid, respectively. V and L are the characteristic velocity and the length, respectively. In our case, $Re \sim 10^{-6}$ and hence the flow around the particle can be laminar and the forces acting on the particles are balanced by the viscous ones.

Capillary number: Capillary number relates the effects from viscous forces with the surface tension (γ) that acts at the interface. Capillary forces dominate over the viscous ones when Ca is smaller than 10^{-4} [33].

Lengths and Numbers	Formula	Physical Effects
Gravitational height	$h_{grav} = \frac{k_B T}{\frac{4}{3}\pi a^3 \Delta \rho g}$	Thermal–gravitational
Debye–Hückel length	$k^{-1} = \sqrt{\frac{\varepsilon_0 \varepsilon_f k_B T}{2e^2 z^2 c_0^*}}$	Electrostatic screening
Colloid capillary length	$\xi_{cap} = \sqrt{\frac{k_B T/a^2}{\Delta \rho g}}$	Interfacial tension–gravitational
Lambda parameter	$\Lambda = \frac{\pi \varepsilon_0 \varepsilon_f a^3 \beta^2 E_0^2}{2k_B T}$	Electric dipolar–thermal
Gamma parameter	$\Gamma = \frac{\frac{\mu_0}{4\pi}(\pi n)^{3/2}\left(\chi_{eff}B\right)^2}{k_B T}$	Magnetic dipolar–thermal
Mason number	$Mn = \frac{\eta_f \dot{\gamma}}{\varepsilon_0 \varepsilon_f \beta^2 E_0^2}$	Hydrodynamic–electric dipolar
Péclet number	$Pe = \frac{3\pi a^3 \eta_f \dot{\gamma}}{k_B T}$	Hydrodynamic–thermal

Table 1.1: Lengths and dimensionless numbers that express the relative importance of some relevant physical interactions like the gravitational, the electrostatic, the electric dipolar, the magnetic dipolar and the hydrodynamics in colloidal systems. Parameters used are the electron charge e, the ion valency z, the ion concentration in the bulk c_0^*, the viscosity of the fluid η_f, the shear rate $\dot{\gamma}$, the electric field strength E_0, the particle and the fluid dielectric constant ε_p and ε_f, respectively, the dielectric mismatch parameter $\beta = \frac{-1+\frac{\varepsilon_p}{\varepsilon_f}}{2+\frac{\varepsilon_p}{\varepsilon_f}}$, the particle-fluid density mismatch $\Delta \rho = (\rho_p - \rho_f)$, the particle radius a, the effective magnetic susceptibility χ_{eff}, the magnetic flux density B and the acceleration due to the gravity g. The Mason and the Péclet numbers are relevant even in a quiescent dispersion because the colloidal particles inside the dispersion are constantly in motion. In this case, the shear rate $\dot{\gamma}$ can be replaced with $\frac{V}{L}$ where V is the characteristic velocity of the particle and L is the typical length, that can be often considered as the particle radius a. Table reprinted from [31].

$$Ca \sim \frac{\mu V}{\gamma} \tag{1.2}$$

The order of magnitude for Reynolds, Capillary and Péclet numbers in our experimental conditions are $\ll 1$ [32].

1.3.   Electric fields and colloids

1.3.1.   Electrical double layer

The amount and the type of ions in a given solution govern the conductivity and can influence the permittivity. The conduction mechanisms in a solution are more complicated than for an ideal dielectric. The ions have a finite size and their mobility in solution is affected by the high permittivity of the water (by considering water as the suspending medium). At any interface between a charged surface (for e.g. particle or electrode) and the solution, the ions gather in a thin layer (around the particle or electrode) to maintain electro-neutrality. This layer is referred as the electrical double layer [34]. On one hand, the presence of the double layer in the electrode can affect the electric field interactions with the bulk solution and leads to the motion of the fluid (electroosmosis). On the other hand, with the particles, this layer has a complex structure and affects the electrical forces acting on the particle (by hindering the surface charge of the particle) and consequently, changing the effective charge on the surface of the particle. In the case of very small particles, the size of the electrical double layer can be large compared to the radius of the particles and hence it plays a important role in the electrokinetic properties associated with the particles. A surface carrying a net charge creates an electrostatic surface potential ϕ_0 local to the interface. When the surface is placed in an continuous medium (e.g. a fluid phase or solvent), this electrostatic potential attracts ions of opposite charge (counterions) from the solution and repels ions of the same sign (co-ions). A schematic representation is shown in fig. 1.7–A. The figure shows the distribution of free charges in a solution close to a charged surface. The fluid region near the interface has a higher density of counterions and a lower density of co-ions. This region is called as the diffuse region of the electrical double layer. The change in the distribution of ions near the surface is determined by the spatial distribution of the surface electrostatic potential. In our vertical deposition experiments (see chapters 2 and 3), we use negatively charged polystyrene particles dispersed in ultra pure water. The ions present in water can thus form an electrical double layer over the polystyrene particles. The surface charge is balanced by an equal and opposite amount of excess charge in the double layer. Hence, the countercharge from the solution effectively screens the surface charge so that the overall charge is zero on a global scale. A thin layer of counterions is between the surface and the diffuse layer, which is called Stern layer, see fig. 1.7–B. This layer is of the order of one or two ions (from the solution). In this region, it is assumed that the potential decreases linearly from the surface value ϕ_0 to ϕ_d, the value of the potential at the interface between the diffuse layer and the Stern layer (see fig. 1.7–B). The potential decreases exponentially across the diffuse layer with a characteristic distance given by the Debye length, κ^{-1} (see fig. 1.7–A). The Debye length is a measure of the thickness of the ionic atmosphere around the particle that screens the charge, and is typically a few nm thick [34]. Also, in table 1.1, the electrostatic screening effect is included. The electrical double layer concept has been explained in depth in [34–36].
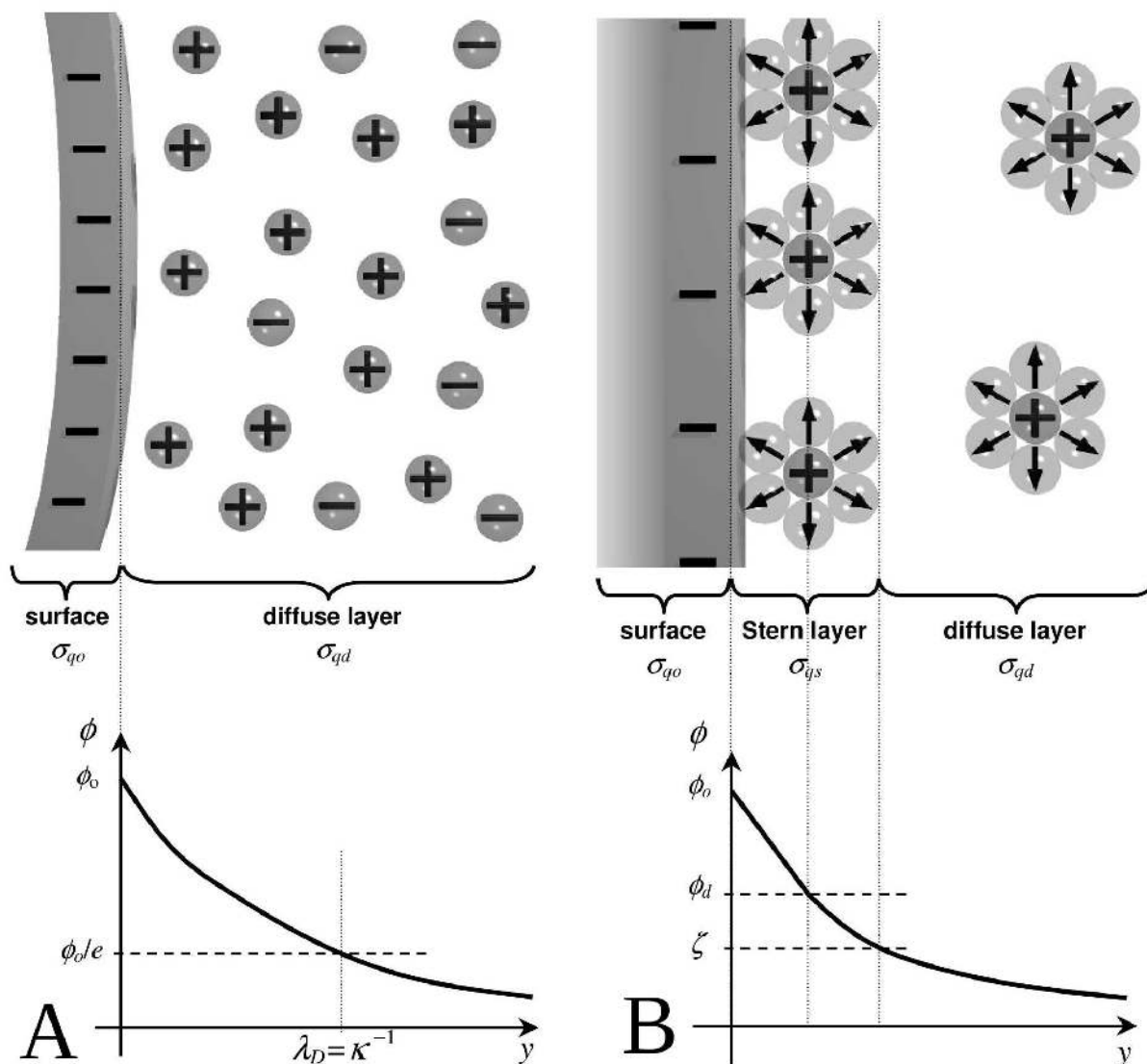
Figure 1.7: Schematic representation of electrical double layer that consists of counterions and co-ions. A: The change in the concentration of ions in the solution close to a charged surface and the variation in the potential with distance y from the surface; B: The Stern layer and the diffuse layer at a charged surface. The variation in the electrical potential with distance y from the surface, highlighting the diffuse layer potential ϕ_d and the zeta potential at the hydrodynamic slip plane ζ. σ_{qo}, σ_{qs} and σ_{qd} are the surface charge density, the Stern layer charge density and the diffuse layer charge density, respectively. Figure reprinted from [34].

1.3.2.   Electrokinetic phenomena

Electrokinetics refers to the relative motion between two charged phases. Electrokinetic phenomena occur when there is a perturbation in the diffuse layer of the electrical double layer (see fig. 1.7–A). This local displacement of ions in the electrical double layer makes the charged surface to move in the one direction while the ions in the diffuse layer of the electrical double layer undergo a net migration in the opposite direction, carrying the solvent along with them (causing the movement of the solvent). Consequently, an electric field (electric dipole) is produced if the charged surface and the diffuse layer of the electrical double layer are made to move relative to each other [37, 38]. In our experiments, we apply weak DC and AC electric fields on the dilute colloidal dispersion (of negatively charged particles) placed between the two electrodes (ITO substrates). We study the influence of the external fields on the evaporative colloidal phase transition. The results are explained through the interaction of the electric field with the colloids. Also, experiments are continued to understand the role of free surface in the colloidal systems with applied electric fields. Of several electrokinetic phenomena, we will focus on electrophoresis, dielectrophoresis and electroosmosis, which are the most relevant in our experiments.
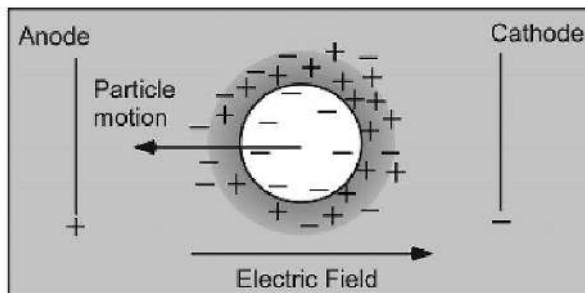
Figure 1.8: Electrophoresis of a charged particle in an external electric field. Figure reprinted from [39].

Electrophoresis: The movement of a charged surface (e.g. colloidal particle) relative to the stationary fluid in a uniform electric field is referred as electrophoresis (fig. 1.8). The presence of the cathode and anode create electric field E in the direction from anode to cathode. Under the external electric field, the negatively charged colloidal particle migrates towards the anode. A charged particle in an electric field experiences a force given by $F = qE$, where q is the surface charge and E is the applied field. In viscous medium, the presence of friction leads asymptotically to the movement of the particle with a constant velocity V. The electrophoretic mobility (μ_E) of a particle is a measure of its velocity response to a uniform electric field.

$$\mu_E = \frac{\mid V \mid}{\mid E \mid} \tag{1.3}$$

When a particle is in an aqueous suspending medium, the presence of the electrical double layer keeps the particle electroneutral. Thus, the excess of charge in the double layer is exactly equal and opposite to the charge on the particle [34]. The particle therefore appears to have zero net charge. But it moves in a uniform electric field. If the ions in the double layer are held tightly with the surface of the particle, then the particle motion will be approximately zero. With the

applied electric field, the ions in the diffuse layer of the electrical layer start to move. These ions (counterions) have opposite sign to the surface charge of the particle and they move in the direction opposite to the direction of the particle motion (if the particle were unscreened). The ion movement gives rise to fluid motion around the particle (electroosmosis). On a global scale, the viscous forces from the suspending medium keep the fluid stationary. As a result, the moving ions push the particle in the opposite direction thus the electrophoretic mobility of a colloidal particle depends on the dimensions of the double layer (thickness of the electrical double layer compared to the radius of the particle). By considering the Smoluchowski [40] theory (valid for thin electrical double layer when the particle radius a is much larger than the Debye length, $a\kappa \gg 1$), equation 1.3 becomes,

$$\mu_E = \frac{\epsilon_0 \epsilon_r \zeta}{\eta} \tag{1.4}$$

where ϵ_r is the dielectric constant of the suspending medium, ϵ_0 is the permittivity of vacuum, η is the dynamic viscosity of the suspending medium and ζ is the zeta potential. In our vertical deposition experiments, the radius of the polystyrene particles is $0.7\,\mu m$ ($a \gg \kappa^{-1}$). An estimation of the order of magnitude for electrophoresis in our experimental conditions is presented in the chapter 3.

Dielectrophoresis: The motion of a particle produced by the interaction of a non-uniform electric field and the induced effective dipole moment of the particle is referred as dielectrophoresis [41]. If the electric field is uniform, the forces acting on each of the two poles in a dipole are equal and opposite and hence there is no motion. But, if the electric field is non-uniform, the forces acting on each of the two poles in a dipole are not equal and therefore the particle moves. To represent the dielectrophoresis in different polarizable cases for particles and different field geometries, numerically calculated electric field lines with the particles are shown in fig. 1.9. The direction in which the particle moves not only depends on the properties of the particle and the suspending medium but also significantly on the applied frequency as the induced dipoles depend on the applied frequency. The expression for time-averaged dielectrophoretic force is [34]

$$\langle F_{DEP} \rangle = \pi \epsilon_m a^3 Real \left\{ \frac{\tilde{\epsilon_p} - \tilde{\epsilon_m}}{\tilde{\epsilon_p} + 2\tilde{\epsilon_m}} \right\} \nabla \mid E \mid^2 \tag{1.5}$$

where ϵ_m is the electrical permittivity of the medium; $\tilde{\epsilon_p}$ and $\tilde{\epsilon_m}$ are the complex permittivity of the particles and the medium, respectively; a is the radius of the particle; and E is the applied field strength. Clausius–Mossotti factor (relates the dielectric constants of two different media and gives the frequency dependence of the polarization effect) is given by

$$f_{CM} = \frac{\tilde{\epsilon_p} - \tilde{\epsilon_m}}{\tilde{\epsilon_p} + 2\tilde{\epsilon_m}} \tag{1.6}$$

The frequency dependence of real part of the Clausius–Mossotti factor for polystyrene particles dispersed in water is shown in fig. 1.10. Positive and negative dielectrophoretic force depends on this factor. When the factor is positive, the dielectrophoretic force acts along the direction of the positive gradient of the electric field intensity (see fig. 1.9–(c)) and when the factor is negative, the force acts along the negative gradient of the field intensity (see fig. 1.9–(d)). The dielectrophoretic forces are present when a spatial gradient of the electric field intensity exists.
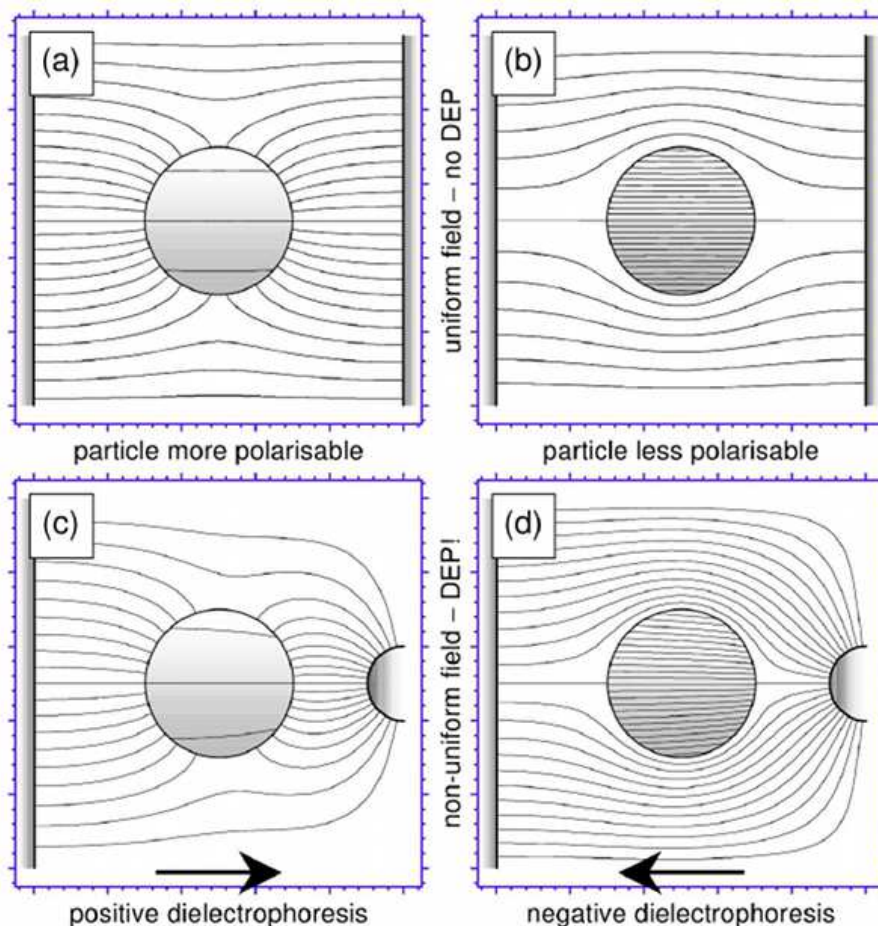
Figure 1.9: Numerically calculated electric field lines for four different cases, defined by the particle that is more polarizable (a) and (c) or less polarizable (b) and (d) than the suspending medium, in a uniform (a) and (b) or a non-uniform electric field (c) and (d). For the more polarizable particle (a) and (c), the field lines are drawn to the surface of the particle, becoming increasingly perpendicular as the polarizability increases, and the field strength inside the particle is low. For the less polarizable particle (b) and (d), the field lines are bent around the particle and the field strength inside the particle is high. In the uniform electric field (a) and (b), the particles will not move as the force acting on each of the two poles in a dipole are equal and opposite. In the non-uniform electric field (c) and (d), the electric field strength on one side of the particle is greater than on the other which generates imbalance forces on the dipoles and they will move. The arrows show the direction of the force and movement in each case. Figure reprinted from [34].
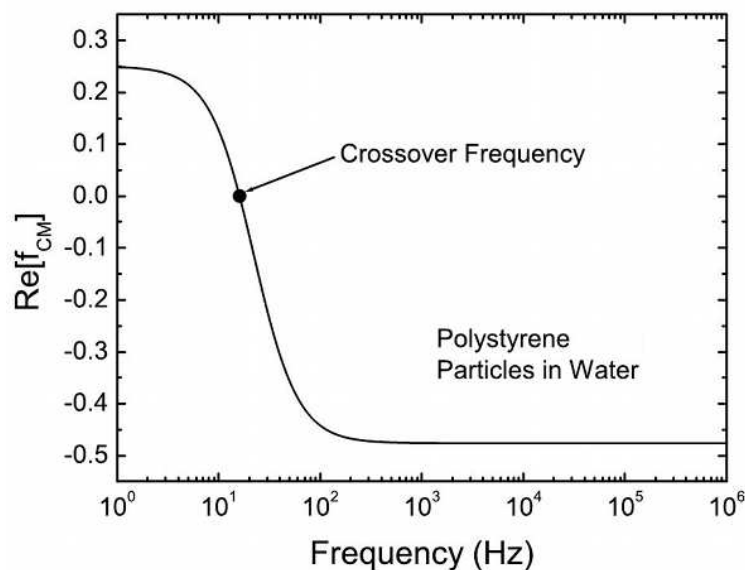
Figure 1.10: Variation of the real part of the Clausius–Mossotti factor as a function of frequency (AC signal) for polystyrene particles dispersed in water. The crossover frequency differentiates the two regimes of dielectrophoresis. At lower frequencies, the system will exhibit positive dielectrophoresis. At higher applied frequencies, the same system will exhibit negative dielectrophoresis (see text for explanation). Figure reprinted from [39].

The forces are absent for the spatially uniform electric fields. To produce the dielectrophoretic force, one needs the field of the order of 10^3 V/mm [39]. In our vertical deposition experiments (see chapter 3), we apply electric fields (DC and AC) which are of the order of 1 V/mm. Thus, we assume the dielectrophoretic effects are negligible in our vertical deposition experiments. An estimation of the order of magnitude for dielectrophoresis in similar experimental conditions is presented in [32].

Electroosmosis: When an electric field is applied tangential to a surface immersed in a fluid, the charges in the electrical double layer at the interface of the surface and the fluid experience a force. Consequently, the charges in the electrical double layer move and drag the fluid along with it. This generates a fluid flow which is referred as electroosmosis. In DC field, the electroosmotic mobility can be given by [34]

$$\mu_x = \frac{u_x}{E_x} = -\frac{\epsilon\zeta}{\eta} \tag{1.7}$$

where u_x is the velocity of the fluid in x direction; E_x is the applied electric field in x direction; ϵ is the permittivity; ζ is the Zeta potential and η is the viscosity.

Experiments with microelectrodes explained that AC electric fields can generate local fluid flow [42–47]. The fluid motion is related to the charges in the electrical double layer. Experimental and theoretical work done with the simple parallel finger microelectrodes are reported in [45–47]. Green *et al.* [47] showed the electroosmotic flow for different kinds of electrode designs with fluorescently labelled latex spheres of sub-micron size. The applied voltage and the frequency were of the order of 1 Vpp and 100 kHz respectively (conductivity of the electrolytic solution was
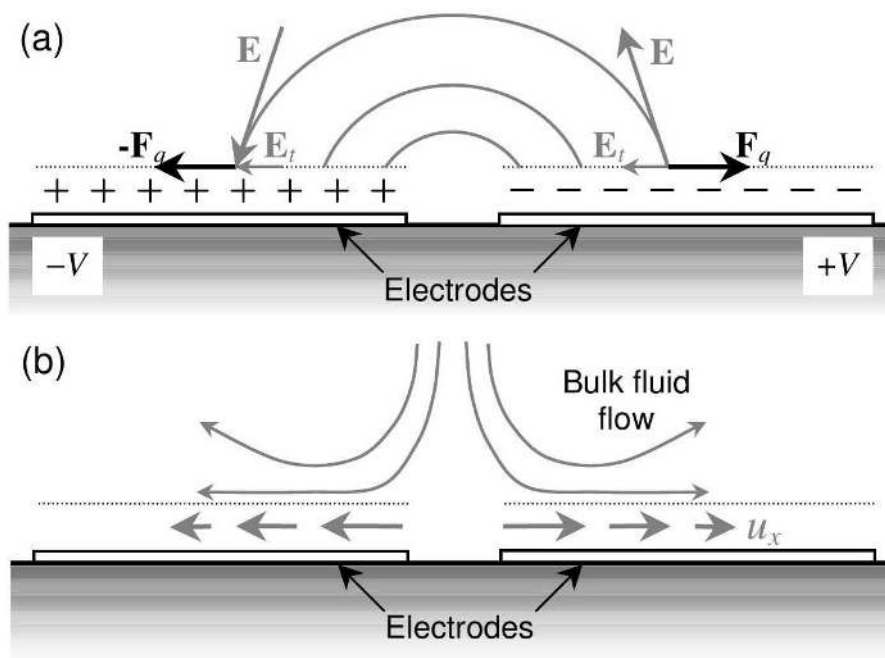
Figure 1.11: Schematic diagram which outlines the mechanism of AC electroosmosis. (a) Induced charges are shown as + and – symbols. The interaction of the tangential field, E_t, at the surface with the charge in the electrical double layer gives rise to a surface fluid velocity u_x and (b) a sketch of the resulting bulk flow is shown. Figure reprinted from [34].

5 mS/m).

   If the electric field is nonuniform, then there is a non-zero time-averaged flow [34]. The mechanism responsible for the electrode polarization is the key idea to understand the AC electroosmosis. The polarization process governs both the potential at the outer edge of the electrical double layer (that gives the tangential electric field) and the potential drop across the double layer (that gives the charge at the surface.) The AC electroosmosis mechanism is sketched in fig. 1.11. The voltages $\pm V$ are applied to either electrode, which give rise to the electric field E with tangential components E_t outside the electrical double layer. Consequently, the charges are induced on the surface of each electrode. The induced charge experiences a force F_q due to the action of the tangential field which results in a fluid flow. Fig. 1.11–(a) shows the system for one half cycle of an AC field. In the other half cycle, the direction of the tangential field and the sign of the induced charge are all opposite. As a consequence, the direction of the force vector remains the same giving a non-zero time-averaged force. A steady state fluid flow occurs which is sketched in fig. 1.11–(b). The velocity of AC electroosmotic flow depends on the applied frequency. At low frequencies, the potential across the suspending medium is zero, hence E_t is zero. Since the tangential field must be continuous and the electrical double layer is very thin, $E_t = 0$ in the double layer and the velocity of the fluid is zero. At high frequencies, the potential across the double layer and the induced charge are both zero and there is no AC electroosmotic flow. To summarize, the velocity profile for AC electroosmosis on perfectly polarizable electrodes is zero at high and low frequencies, and maximum at an intermediate characteristic frequency (of the order of kHz) [34]. In our experiments (see page 56), AC electric fields are of the order of 1 V/mm

and 1 Hz are applied. Hence, we assume that the effects due to electroosmosis are negligible due to the applied low frequency; however, an ongoing collaborative work with similar experimental conditions is in progress to provide quantitative relevance of this effect in our system.

1.3.3. Electrowetting

In addition to the electrokinetic phenomena, the applied electric field can influence the system by modifying the wetting properties of the substrate through electrowetting. Schematic drawing of an electrowetting experiment is shown in fig. 1.12. When an electric field is applied between the conducting droplet (solid circular line in fig. 1.12) and an electrode placed underneath the droplet (rectangle hatch in fig. 1.12), the contact angle of the droplet on the electrode surface can be reduced, which is referred as electrowetting [48–55]. The applied electric field results in a distribution of charge (see magnified portion in fig. 1.12) that varies the free energy of the droplet [48]. Consequently, the droplet wets the electrode surface (dashed circular line in fig. 1.12). In systems where the liquid is in direct contact with the solid electrode surface, the potential drop is across the diffuse layer of the electric double layer at the interface. In systems where an insulating layer of thickness d is between the electrode surface and the liquid (fig. 1.12), the potential drop is across the insulating layer. Hence, the properties of the insulating layer such as the thickness and the permittivity are significantly important.
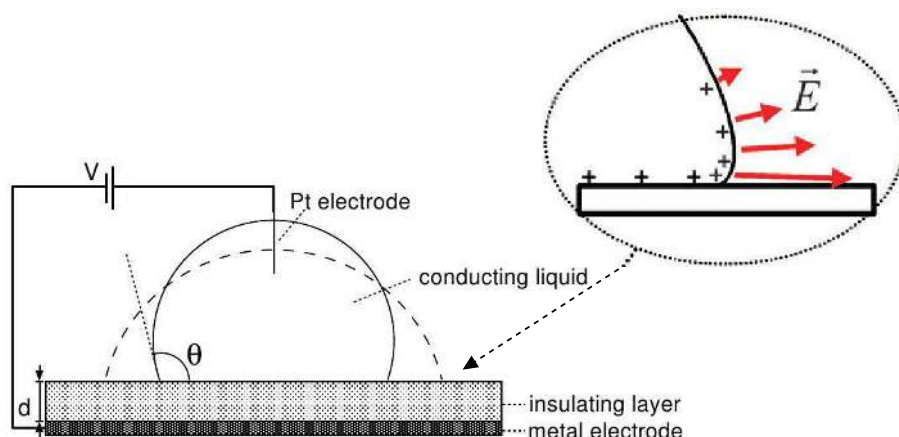
Figure 1.12: Schematic drawing of an electrowetting experiment. A droplet of a conducting liquid is placed on an insulating layer of thickness d, which is deposited on a metal counter electrode. Application of a potential V between the droplet and the metal electrode changes the free energy of the droplet and results in a decrease of the contact angle θ. The resulting droplet shape is indicated by the dashed circular line. The magnified view shows the bent surface profile and the diverging charge density in the vicinity of the contact line. Red color arrows indicate the electric field. Modified figure reprinted from [48] and [55].

The equation for electrowetting relates the change in contact angle of a liquid droplet with the applied electric field. It can be obtained by considering the minimum free energy required for the thermodynamic equilibrium conditions which is explained in [48]. The equation for electrowetting is (by considering the contact line does not recede)

$$cos\theta = cos\theta_0 + \frac{\epsilon V^2}{2\gamma_{12}d} \tag{1.8}$$

where θ_0 is the mean contact angle without externally applied electric potential; θ is the mean contact angle when the electric field (V) is applied; ϵ is the electric permittivity of the dielectric layer of thickness d beneath the droplet (see fig. 1.12); γ_{12} is the interfacial tension between the liquid droplet and the surrounding medium (air).

(a) f = 1 kHz   (b) f = 18 kHz   (c) f = 128 kHz
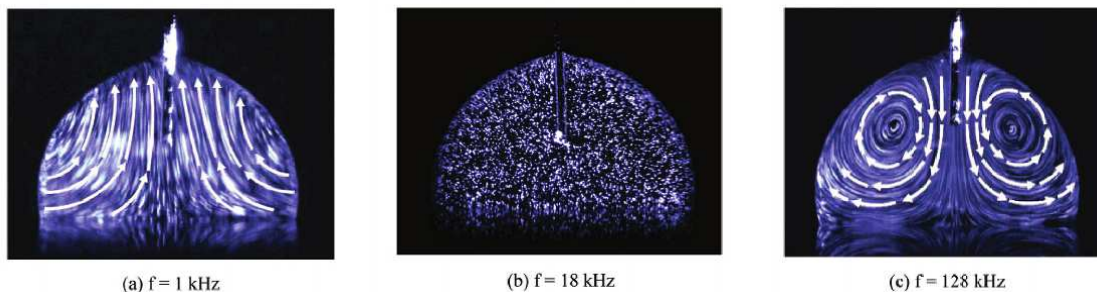
Figure 1.13: Frequency dependence of the flow pattern for the applied field of 226 Vpp in a NaCl droplet of concentration 10^{-3} M. Figure reprinted from [53].

Research groups reported the presence of hydrodynamic flows in electrowetting [52, 53, 56]. In our vertical deposition experiments, where the contact line does not recede significantly, these flows are relevant and they explain the observed behavior (see page 53). Ko *et al.* [53] gave evidences on hydrodynamic flows in electrowetting. They used sub-micron fluorescent polystyrene particles as tracers. The particles were dispersed in NaCl solution. They showed two distinctive flow patterns that appear with their experimental system and the flow patterns depend on the applied frequency. Frequency dependence of flow patterns for the applied field of 226 Vpp in a NaCl droplet of concentration 10^{-3} M is shown in fig. 1.13. They conclude that the oscillation of the droplet interface (see instantaneous images obtained using a high-speed camera in fig. 1.14) is responsible for the flows that appear at applied low frequencies. They explained the origin of the flows (at applied low frequencies) through the electrical stress acting on the edge of a droplet (fig. 1.14–(a) and (b). The applied AC electric field gives time-periodic force acting on the edge of the droplet and in turn the force generates a subsequent oscillation of the droplet interface [53]. Flows that appear in high frequency range (fig. 1.13–(c)) can be due to the effects from electrohydrodynamics [53] and the electrothermal effects [52] (also, the oscillation of the droplet interface is absent at the applied high frequency, see fig. 1.14–(d)). Flows that appear in low frequency range (fig. 1.13–(a)) can be relevant to our experiments; however, in our case we apply weak alternating electric fields (of square wave form) of the order of 1 Vpp/mm and 1 Hz. Clusters of colloidal particles may form near the horizontal contact line due to the flows produced by electrowetting. We use the colloidal dispersion of concentration 0.5% w/w (polystyrene particles are dispersed in ultra pure water).
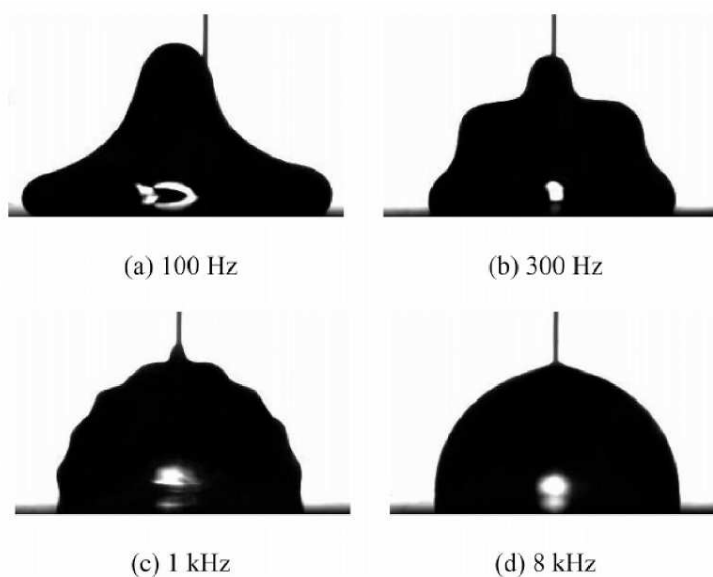
Figure 1.14: Snapshots of the oscillating droplets obtained using a high-speed camera for different applied frequencies. Figure reprinted from [53].

1.4.   Shear stresses and colloids

1.4.1.   Shear induced order
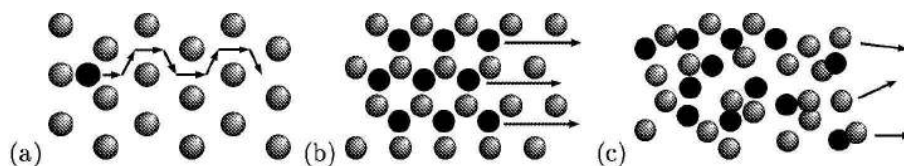
Figure 1.15: Flow phases of a sheared colloidal dispersion of hard spheres: (a) at low shear rates, the black particle, representative of a second hexagonally close-packed layer of particles, hops between interstices of the layer below (follow the arrows); (b) at higher shear rates hexagonal layers slide over each other; (c) at still higher shear rates, the particle microstructure becomes disordered. Figure reprinted from [57].

The relationship between the fluid flow and the structure formation has been studied well by both theory and experiments [57–65]. Below a critical volume fraction, colloidal particles have Brownian motion and they behave liquid-like structure at equilibrium. When the shear forces dominate on the forces associated with the Brownian motion, the microstructure is distorted. Unlike the dispersions of low volume fraction, concentrated dispersions of colloidal particles can undergo dynamic phase transition under shear stresses [58, 63, 64]. Hoffmann [65] reported the first evidence that the application of shear flow can induce order in the colloidal system of hard spheres. He showed that the suspended particles align into layers at low shear rates and the alignments are destroyed on increasing the shear rate to a certain value, giving rise to a large discontinuous increase in the viscosity of the dispersion. This behavior is commonly referred as

shear thickening [66] and it can be understood along with the jamming and glass transitions. In many colloidal dispersions, shear induced order can be obtained but the viscosity decreases with the increasing shear rate called shear thinning behavior [66].

At small shear rates, the Brownian motion and the interparticle interactions dominate the formation of microstructures. For large shear rates, the hydrodynamics influences the microstructure. The dimensionless Péclet number (see table 1.1) characterizes the relative importance of hydrodynamics to the Brownian motion. For the dispersions of hard spheres, the transition between the hydrodynamic and the Brownian motion dominance occurs at Péclet number$\sim$1 [67]. Ackerson *et al.* [60] provided detailed explanation on the microstructure states in the colloidal dispersion and its relation with the rheology of dispersion. A schematic drawing for the flow phases of a sheared colloidal dispersion of hard spheres is shown in fig. 1.15. At low shear rates (fig. 1.15–(a)), a second hexagonally close-packed layer of particles (black particle) hops between the interstices of the layer below (particles with hatch). At high shear rates (fig. 1.15–(b)), the hexagonal layers slide over each other. On further increasing the shear rates, the particle microstructure gets distorted (fig. 1.15–(c)).
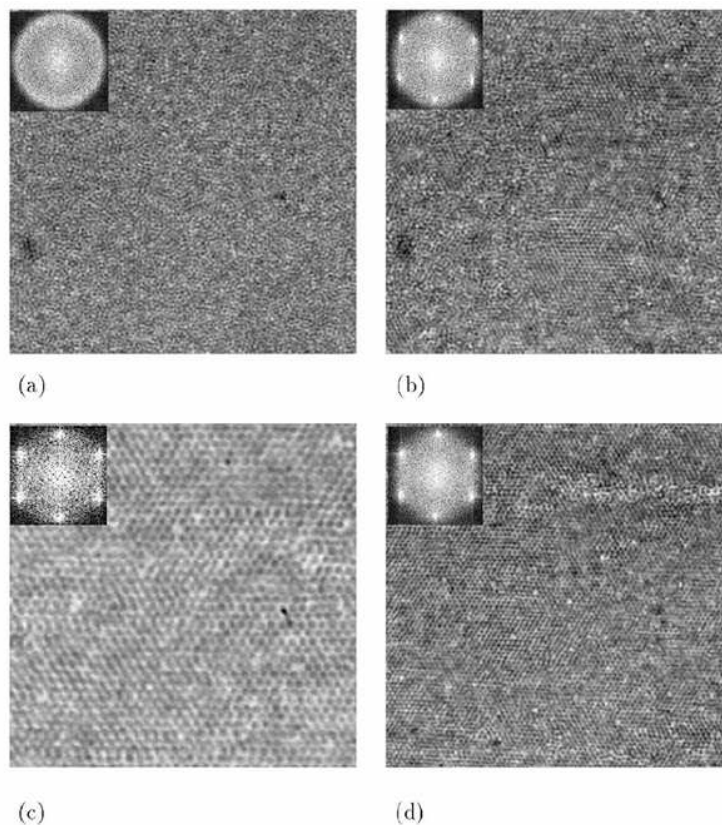
Figure 1.16: Micrographs from a shear experiment at high strain, γ=3.1 using 100× objective. The velocity direction is horizontal. The shear frequency is 0.2 Hz. Times after the beginning of shear are (a) 0 (immediately before shear), (b) 2 minutes and 50 seconds, (c) 7 minutes and 30 seconds (magnification doubled using an eyepiece lens in front of the charge coupled device camera), and (d) 13 minutes and 25 seconds. The insets show the calculated Fourier transforms of the respective images. Figure reprinted from [63].

Haw *et al.* [63] showed the ordering in concentrated colloidal dispersions of hard spheres subjected to oscillatory shear in a parallel plate geometry. They used concentrated dispersions of PMMA (poly methyl methacrylate) particles of diameter 970 nm suspended in cis-decalin. A droplet of the dispersion is sheared and it is observed directly using optical microscope. They report that the ordering inside the dispersion depends on the strain amplitude. At high strain amplitude, the particles arrange quickly into hexagonal planes in the plane of shear. The close-packed direction is parallel to the velocity axis. At low strain, they obtained a polycrystalline structure consisting of hexagonally ordered regions with a distribution of different orientations. Here the close-packed direction is perpendicular to the velocity axis. Micrographs obtained at high strain γ=3.1 and frequency of 0.2 Hz are shown in fig. 1.16. The velocity direction is horizontal. There is no order visible in the sample before applying the shear (see fig. 1.16–(a)). On applying the shear, hexagonal order oriented with a close-packed direction parallel to the velocity axis appeared (see fig. 1.16–(b) and (c)) and reaching high degree of hexagonal order (see fig. 1.16–(d)). The insets in fig. 1.16 show the calculated two dimensional Fourier transforms of respective micrograph. The sharp hexagonal peaks in the inset of (c) and (d) in fig. 1.16 indicate the planes are strongly ordered. Fig. 1.17 illustrate that the duration of oscillatory shear force has an effect on the ordering process. The sample is sheared at γ=1 and a frequency of 5 Hz. Images from left to right in fig. 1.17 represent an unsheared sample, a sample sheared for 2 minutes and a sample sheared for a total of 5 minutes. The insets are 2D fast Fourier transforms that show the evolution of Bragg peaks in the samples. The 3D renderings at the bottom of the figure (see fig. 1.17) show the spatial degree of ordering for the entire image volume.

1.4.2.   Spin-coating

First spin-coating was performed in the year 1922 by Walker *et al.* [68]. They poured paints and emulsions over the rotating glass / steel disks. The poured fluid got sheared and the solvent dried up, leaving the deposit of the material over the disk. They used the spin-coating process to study the physical properties of paints. Later on, many research groups studied the spin-coating process (fluid on a rotating disk problem) by theory as well as by experiments [69–82]. Spin-coating of polymer solutions [83–85] is well established and gains commercial interest. The key variables in the spin-coating or the rotating disk systems are the spinning rate, the viscosity, the density and the evaporation rate of the fluid. These variables are highly related to the final thickness of the spin-coated film or deposit. Reported theoretical models give information on the flow and fluid properties for the rotating disk systems [69–72]. In the spin-coating or rotating disk systems, the thickness of the film (final deposit) is very small when compared to the other two dimensions. The lubrication approximation [86] can be used to study the flow of a viscous fluid bounded below by a horizontal disk (substrate) and above by an interface (between the fluid and the atmosphere). In the following, we summarize the continuum models [69, 70, 79] for spin-coating or rotating disk system.

Emslie *et al.* [69] reported the equation which takes into account the governing forces in the rotating disk systems. The reported dominant forces are the viscous forces due to fluid properties and the centrifugal forces from spinning.

$$-\eta\frac{\partial^2 v}{\partial z^2} = \rho\omega^2 r \tag{1.9}$$
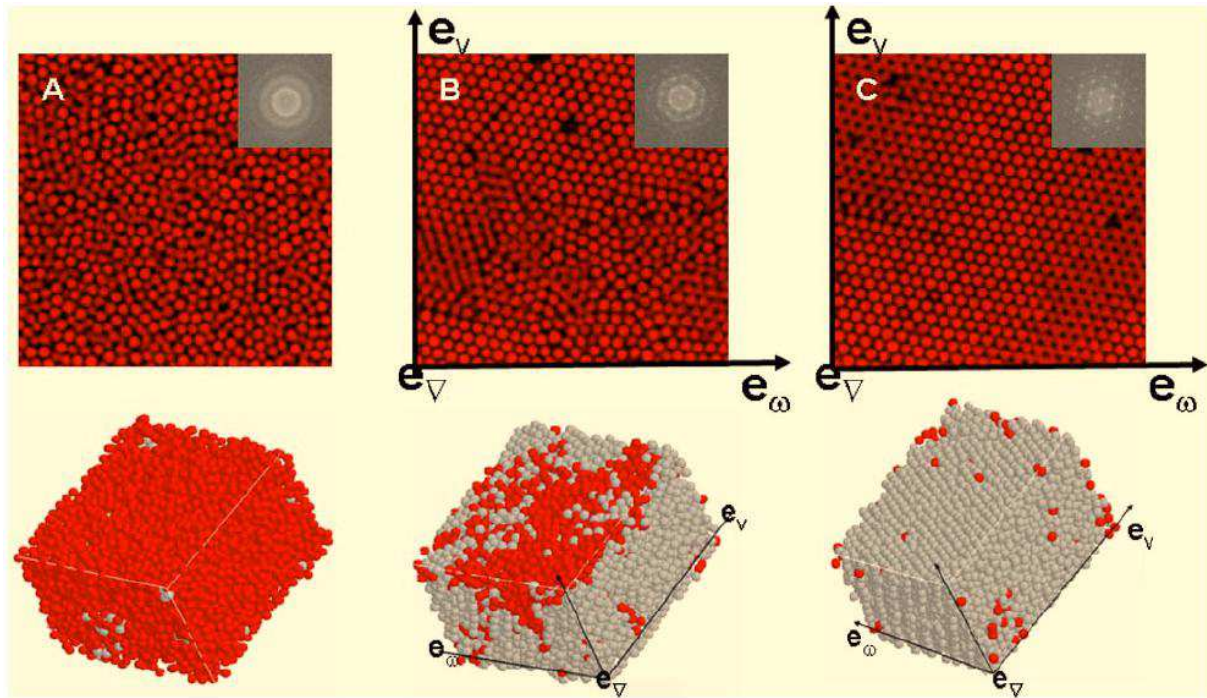
Figure 1.17: 2D micrographs with insets (fast Fourier transforms) and 3D renderings illustrating the effect of shearing time on the degree of crystallization for $\gamma=1$ and a frequency of 3 Hz. (A) Unsheared sample, (B) t=2 minutes, and (C) t=5 minutes. e_ω, e_∇, e_v represent vorticity, gradient, and velocity directions, respectively. Figure reprinted from [64].

where η, ρ are the viscosity and the density of the fluid respectively, v is the radial velocity of the fluid at any point (r,θ,z) rotating with the spinning disk at angular velocity ω.

With the assumption of a homogeneous thickness, eq. 1.9 [69] leads to

$$\frac{dh}{dt} = -2Kh^3 \tag{1.10}$$

where $K = \frac{\rho\omega^2}{3\eta}$ and h is the thickness of the layer

whence, Eq. 1.10 becomes,

$$h = \frac{h_0}{\left(1 + 4Kh_0^2 t\right)^{\frac{1}{2}}} \tag{1.11}$$

where the constant h_0, independent of r, corresponds to the initial height of a fluid layer.

When fluids like polymer solutions, emulsions, dispersions are spun, they leave a thin layer of deposit. The deposit composes of solute and trace elements from solvent present in the solution. In some cases, the solute might have reacted with the solvent and the final product can be deposited. This behavior might indicate that the continuous phase (solvent) has been evaporated during the spin coating process.

By considering the evaporation, Meyerhofer [70] included a correction, E, to Eq. 1.10.

The rate of change in volume of the solvent to the time is given as

$$\frac{dL}{dt} = -(1 - C_s)\frac{2\omega^2 h^3}{3\nu} - E \tag{1.12}$$

where L is the volume of the fluid per unit area, C_s is the concentration of the solid, h is the thickness and ν is the kinematic viscosity (η/ρ).

The approximation by Meyerhofer [70] is based on the assumption that the spin-coating process consists of two different stages. Initial stage is a flow dominated one, which is then followed by an evaporation of the solvent.

Later, Cregan et al. [79] proposed a study, where they consider that the evaporation of solvent is simultaneous at once the dispersion is being pipetted onto the spinning substrate. Hence the thickness of the final dimensional layer is given by the equation 1.13.

$$h^* = \frac{S_0}{L_0}\left(\frac{E}{\alpha}\right)^{\frac{1}{3}} \tag{1.13}$$

where S_0 and L_0 are the initial solute and the solvent thickness respectively ($S_0 + L_0$ is the initial film thickness), $\alpha = \frac{2\omega^2}{3\nu}$, h^* is the thickness of the final layer and E corresponds to the evaporation rate of the solvent. This comes from an asymptotic expression of Meyerhofer's equation [70] which assumes planarity. We proposed a spin-coating model for the colloidal systems (spin-coating of colloidal dispersion) based on the equation 1.13. The model is discussed in chapter 5.

1.4.3. Spin-coating of colloidal dispersions

Jiang et al. [87] fabricated wafer-size colloidal crystal using spin-coating technique. They spin-coated a solution of silica particles (of diameter 325 nm) dispersed in a polymer matrix (to prepare macroporous polymers by removing silica particles). From this method, they obtained 3D colloidal crystals, which are trapped inside a polymer matrix. Also, the thickness of the colloidal
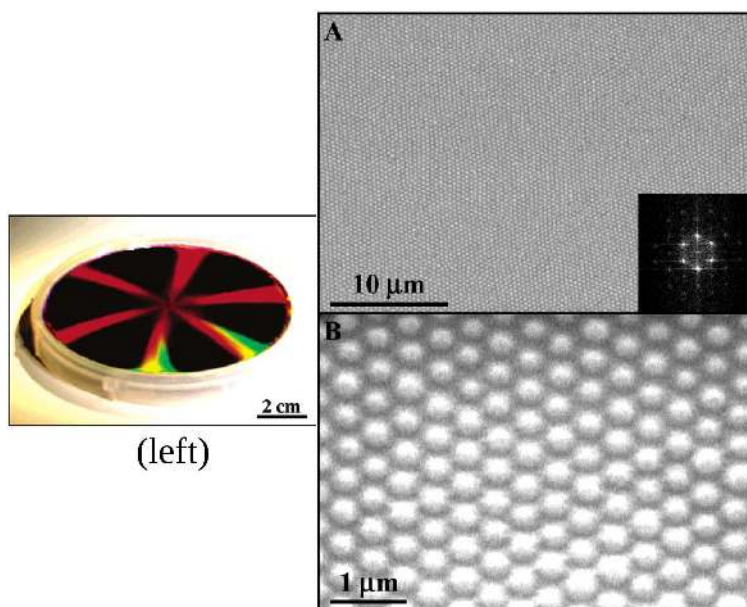
Figure 1.18: (left) Photograph of a 3D ordered film on a 4-inch silicon wafer illuminated with white light. The sample is made from 325 nm diameter colloidal spheres and spin-coated at 600 rpm for 120 seconds. (A) and (B) SEM images of a spin-coated colloidal crystal-polymer film. (A) Top-view image of the sample shown in the left. The inset showing a Fourier transform of a $40{\times}40$ μm^2 region. (B) Higher magnification SEM image of the same sample. Modified figure reprinted from [87].

crystal-polymer film was highly uniform. They reported that the thickness can be controlled by changing the spinning speed and the time. Fig. 1.18 shows the fabricated colloidal crystals in different views of observation, macroscopic and microscopic. Fig. 1.18–left shows a photograph of 3D ordered film of colloidal particles in polymer matrix on a 4-inch silicon wafer illuminated with the white light. Under the illumination, a strong monochromatic diffraction with six arms can be seen, indicating the formation of hexagonally packed spheres parallel to the wafer surface [65]. Multiple reflected colors (see fig. 1.18–left, fig. 1.19–left and fig. 1.20–(A), (B)) are due to the other orders of Bragg diffraction. Higher magnification micrographs (SEM images in fig. 1.18–(A) and (B)) and an inset in (A) confirm the hexagonally packed spheres.
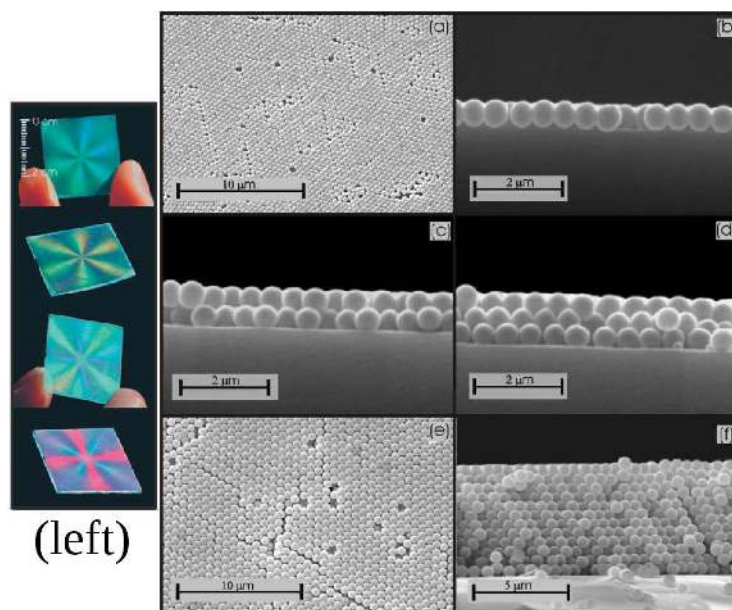
Figure 1.19: (left) Images of the optical diffraction patterns observed in the spin-coated samples under the solar illumination. (a) to (f) SEM images of spin-coated samples at various spinning velocities. (a) Top view of a monolayer of silica spheres packed hexagonally, obtained at ω=10500 rpm; (b) side view of the previously mentioned monolayer; (c) a bilayer obtained at ω = 7500 rpm; (d) a 3 monolayer stacking of silica spheres produced at ω=4500 rpm. Images in (e) and (f) are top and side views of an 12 monolayer colloidal crystal grown at ω=1500 rpm. Modified figure reprinted from [88].

Similar spin-coating experiments were performed with colloidal dispersions of volatile solvent (like ethanol, ethylene glycol, acetone, methyl ethyl ketone etc.). The aims of the reported works [88–90] are to fabricate well ordered colloidal crystals as well as to understand the dynamics of the structure formation in colloidal spin-coating [90, 91]. A summary of the obtained colloidal crystals using volatile solvent is shown in fig. 1.19 and fig. 1.20. Mihi *et al.* [88] used sub-micron silica particles of diameter 400 and 600 nm dispersed in ethylene glycol and ethanol, respectively. They control the spinning rate as well as the time taken by the solvent to evaporate. SEM images of the spin-coated substrates are shown in fig. 1.19–(a) to (f). They control the number of layers of colloidal particles by varying the spinning rate (fig. 1.19–(b), (c), (d) and (f); 10500, 7500, 4500, 1500 rpm, respectively). Arcos *et al.* [89] used silica particles of 458 nm dispersed in ethanol or
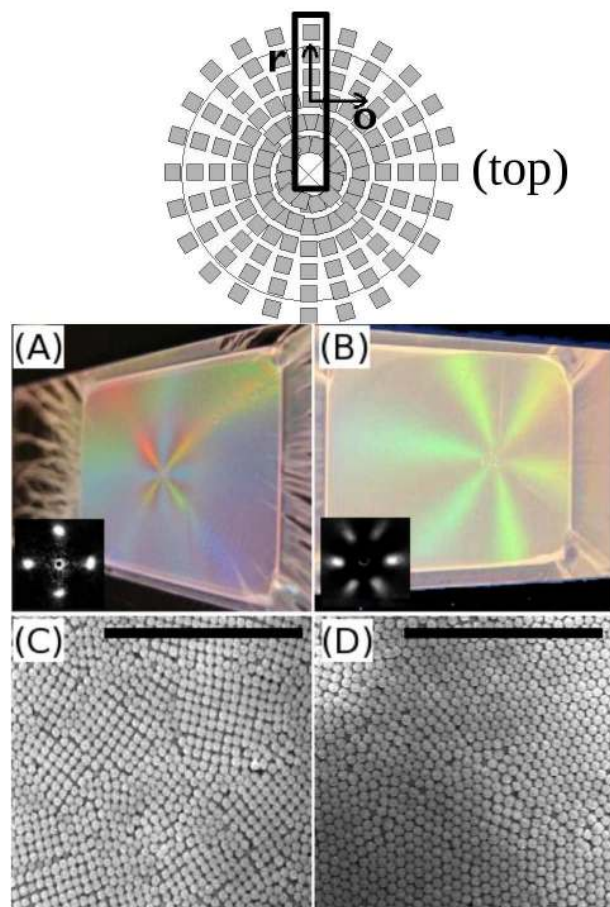
Figure 1.20: (top) Proposed structure of the orientationally correlated polycrystal (OCP): gray squares represent small domains in radial orientational registry. (A) and (B) White-light reflections of colloids spin-coated at 3000 rpm from (A) acetone and (B) ethanol solvents onto 22×30 mm^2 cover slides display fourfold and sixfold symmetry. Laser diffraction patterns (insets) show the fourfold and sixfold symmetries; (C) and (D) SEM images near the center of samples with four-arm and six-arm crosses show planes with square and hexagonal symmetry. Scale bars are 10 μm. Modified figure reprinted from [89].

acetone (see fig. 1.20–(A) to (D) for white light reflections, laser diffraction patterns as insets and SEM images). They performed laser diffraction studies on the spin-coated samples by doing a radial translation (see r in fig. 1.20–top) as well as an off center translation (see o in fig. 1.20–top). They showed that the single crystalline domains are arranged in radial orientational registry (see fig. 1.20–top) and it is termed as orientationally correlated polycrystal (OCP).
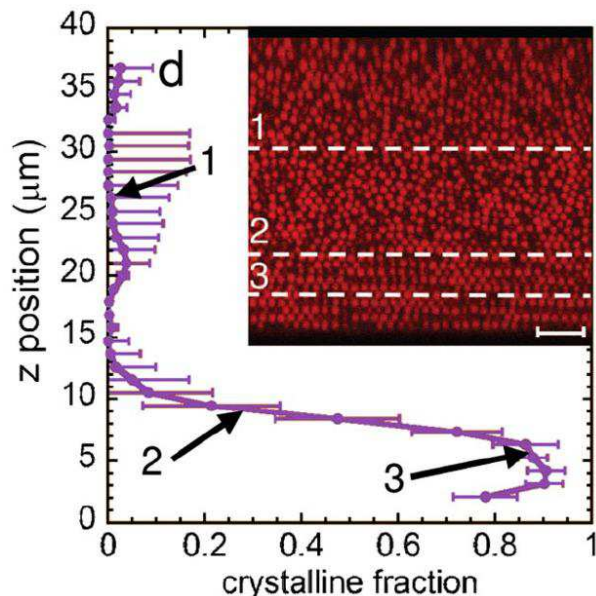
Figure 1.21: Axial variation (vertical axis) of crystal quality in a spin-coated sample through its thickness. The inset is a confocal image acquired perpendicular to the substrate of the sample plotted in (d), Z position. The numbers in the inset of (d) correspond to the heights in (d), Z position. Scale bar is 5 μm. Modified figure reprinted from [91].

Shereda *et al.* [91] demonstrated the spatiotemporal variation in the crystal order of the concentrated colloidal dispersions under shear. By using confocal microscopy, they studied the crystal quality as a function of various positions in vertical Z axis (through the thickness of the spin-coated sample), the spinning speed and the size of the particles. They reported a new method that combines the confocal microscopy with the fast structural quenching (using photopolymers and photoinitiator additives). The local crystalline order throughout the 3D volume of the spin-coated film is shown in fig. 1.21. The crystallinity is varying along the Z direction (direction perpendicular to the substrate). The substrate boundary is at the bottom. The three dashed lines in the inset correspond to the three different positions in the Z axis (Z direction is perpendicular to the substrate) indicated in the fig. 1.21. The local crystallinity is high at the bottom of the film while there is no order as the Z value is increasing (approaching towards the surface of the film). They conclude the study by correlating the Péclet number, the microscopic strain and the crystalline fraction.

Recently, Giuliani *et al.* [90] provided insights on the dynamics of crystal structure formation in the spin-coating of colloids. They used colloidal dispersion of 458 nm silica particles dispersed in methyl ethyl ketone. They reported the transient dynamics of evaporative colloidal spin-coating though high-speed imaging and correlated it with the spinning speed. Sequential images
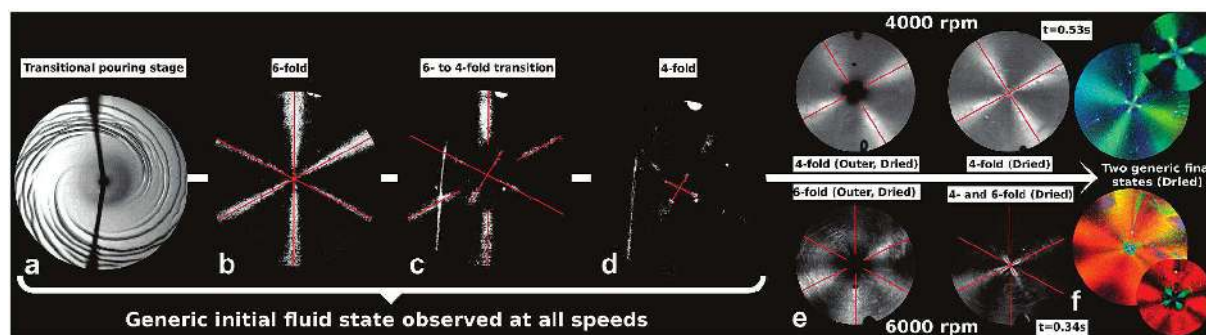
Figure 1.22: Sequential images illustrate the transient dynamics of long-range orientational order. (a) The dispersion is pipetted onto the rotating substrate (b) Six-arm symmetry is observed and to be extended along the whole surface of the substrate. (c) This order prevails for relatively long times but finally transitions to 4-fold symmetry. (d) The four-arm pattern rapidly shrinks toward the center. (e) The drying begins on the periphery, and the drying front (the interface between bright and dark regions) propagates radially toward the center. (f) 4-fold symmetry at low angular speeds and mixed structures, e.g., center 4-fold and the outer area 6-fold, at high angular speeds. Red lines are drawn on the top of the arms as a guide to the eye. Figure reprinted from [90].

illustrating the transient dynamics of long-range orientational order are shown in fig. 1.22. They showed the symmetry transitions and the thinning dynamics of a colloid that pipetted onto the spinning substrate. The report also suggests that the thinning dynamics controls the local volume fraction and the stress profiles which in turn drives the structural transitions. Thickness measurements of the spin-coated films from the center of rotation explain the non planarization phenomenon obtained in these kind of systems [90].

The colloidal crystals obtained by spin-coating method are orientationally correlated [89] due to the axial symmetry from the spinning. We study the spin-coating process with external fields (see chapter 5). The external field is applied when the colloidal dispersion is pipetted onto the spinning substrate. We investigate two kinds of system, spin-coating of superparamagnetic colloids with magnetic fields and spin-coating of non magnetic colloids with electric fields. In the former case (superparamagnetic colloids under shear with magnetic fields), there are numerical reports that study the influence of the external magnetic field on the magnetic fluids under shear [92–96]. In our case, we apply an axial magnetic field during the spin-coating of superparamagnetic colloids. Clusters of superparamagnetic particles form which may be relevant to study the structure formation mechanisms in the spin-coating of colloidal dispersion. The results are discussed in chapter 5. In the later case (non magnetic colloids under shear with electric fields), Hui *et al.* [97] reported a method that combines spin-coating and application of static electric field (in fabricating polymer photovoltaic devices). They used poly (3, 4-ethylenedioxythiophene):poly(styrenesulfonate) solution and the static electric field is applied while spin-coating the solution. In our case, we apply a non uniform alternating electric field (field direction to be stationary in the rotating frame) during the spin-coating of non magnetic colloids. With the electric field, we are able to break the axial symmetry from the spin-coating. The results are also discussed in chapter 5.

1.5.   Objectives of the work

The Thesis aims on the non equilibrium phase transition in the colloidal system (evaporative colloidal phase transition). External fields such as electric, magnetic and centrifugal forces are applied while the phase is getting transferred. We study on how the in-situ variables during the transition can be influenced by these external fields. The colloidal dispersion undergoes the phase transition in different time scales; in the case of experiments of long duration, vertical deposition technique is followed and in the case of experiments of short duration, spin-coating method is used. Colloidal dispersions of dissimilar properties and nature are considered for the experiments. The final deposits of colloidal particles are characterized and correlated with the experimental conditions and the external field.

Chapter 2

Materials and methods for vertical deposition experiments

2.1. Outline

The experiments are performed by modifying the Vertical deposition (VD) technique, that is derived from Langmuir–Blodgett method (see chapter 1). We apply weak DC electric fields to the colloidal dispersion which is kept in an environment of controlled temperature and humidity. In the last part of this chapter, similar VD experiments are performed at room conditions with alternating electric fields. This chapter also explains the experimental procedures to study the contact line region.

2.2. Deposit morphology and statistics of the "macroscopic" speed of receding contact line

2.2.1. Colloidal dispersion

The experiments are performed with aqueous dilute polystyrene (PS) colloidal dispersion. The spherical colloidal particles are of diameter 1.3 μm, polydispersity 0.039 and surface charge -7 μC/cm^2. The stock dispersion was acquired from Dr. Paulke at Fraunhofer-IAP, Germany of concentration 7.43% (w/w). This stock dispersion is diluted to desired concentrations using ultra pure water. The dispersion is maintained inside the refrigerator to reduce the evaporation. Prior to the experiments, dilute dispersion is ultrasonicated for fifteen minutes to obtain an homogeneous dispersion.

2.2.2. Substrates

The substrates used for all the experiments are standard coated glass of size 17×18 mm^2 (purchased from Visiontek systems). The coating consists of a thin conductive layer (150 nm) of Indium Tin Oxide (ITO) on one side of the substrate to apply electric fields. Before starting the experiments, the substrates were wet cleaned.

Wet cleaning

The ITO coated glass substrates are made hydrophilic (ITO coated side) by a soft surface etching using chemical methods. During the course of wet cleaning, the substrates are first treated with acetone in an ultrasonic bath for fifteen minutes and then rinsed with ultra pure water. The substrates are then soft etched with a basic piranha solution of composition 5:1:1 (H_2O:NH_4OH:H_2O_2) at 66°C for thirty minutes. The substrates are finally rinsed with ultra pure water and dried with nitrogen gas blow.

2.2.3. Experiment cell
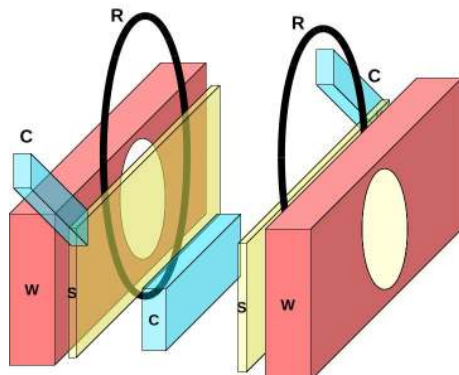
Figure 2.1: Expanded view of the experiment cell which is used for VD experiments. W: Teflon cell wall; C: Ceramic spacers, in which the side of the spacers at the top in contact with the ITO side of the substrate (S) is coated with silver paint for electrical conductivity; S: ITO coated substrates, where the ITO sides are facing opposite to each other; R: Rubber O-rings.
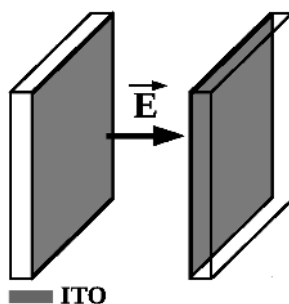
Figure 2.2: Direction of the applied electric field far from the boundaries and from the free surface.

The experiment cell shown in fig. 2.1 is made of Teflon. The cell is designed in such a way that two substrates are placed vertically. Also, the front and back windows allow to track the contact line as the evaporation of the dispersion takes place. A ceramic spacer is used to separate the two substrates by a fixed distance of 1 mm. The spacer is placed at the bottom of the cell. Two more ceramic spacers are placed on the top of the cell (between the ITO substrates). These ceramic spacers have one side which is coated with silver paint for electrical conductivity. This will make a contact with the conductive side of the ITO coated substrate. The conducting sides of the ITO

coated substrates are in contact with the colloidal dispersion. The applied electric field (far from the boundaries and from the free surface) is perpendicular to the substrates (fig. 2.2). Suitable rubber O–rings are used to hold these components (cell, ITO substrates, spacers) tightly which form the complete experiment cell. The cell, spacers and the O–rings are cleaned with ultra pure water and dried before mounting.

2.2.4. Experiment
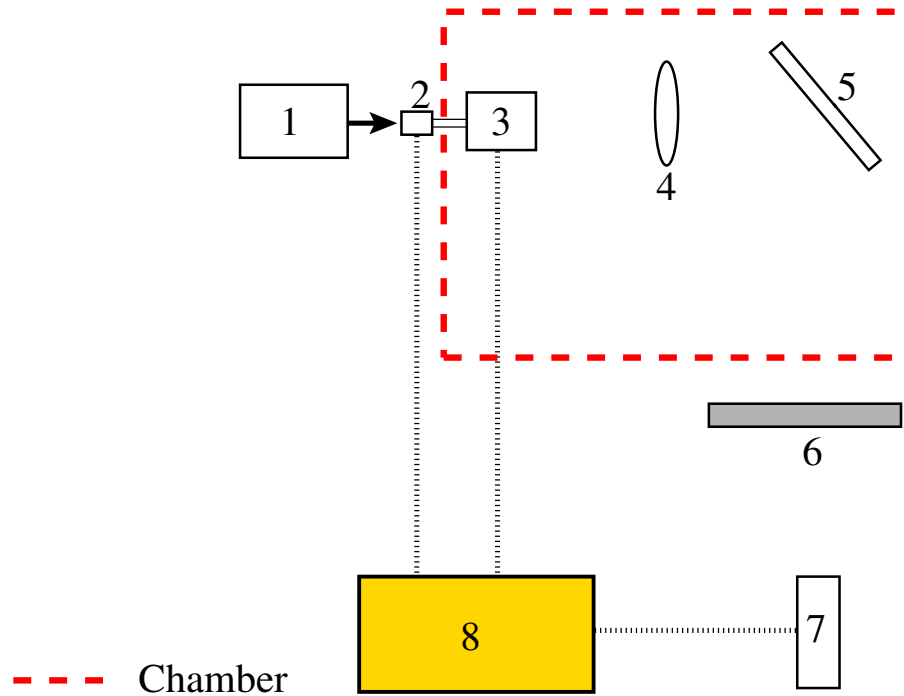
Figure 2.3: Sketch of the experiment setup to track the receding contact line. 1: Cold light source; 2: Linear actuator; 3: Experiment cell; 4: Lens; 5: Mirror; 6: Diffuser; 7: CMOS camera; 8: Computer.

The sketch of the experiment setup is shown in fig. 2.3. The mounted experiment cell is placed in a thermal chamber, where the temperature and the humidity can be controlled. For our experiments, the temperature is maintained at 63°C and the relative humidity is below 2%. The hydrophilic character of the freshly cleaned ITO substrates changes during the initial stages [98–100]. This has an effect on the mean contact angle when the dispersion is loaded into the experiment cell. To stabilize this hydrophilic character of the substrate during the course of the experiments, the cell is kept inside the thermal chamber for four hours [32] (time required to stabilize the mean contact angle for aqueous PS colloidal dispersion on a freshly cleaned ITO coated substrate).

Before loading the dispersion into the experiment cell (which is preheated at 63°C), the dispersion is ultrasonicated for fifteen minutes followed by the thermal treatment of the dispersion (to the working temperature, 63°C) for three minutes. The dissolved CO_2 and air bubbles are removed by nitrogen gas bubbled into the dispersion for one minute. Now the dispersion of volume 420 μl is loaded into the experiment cell and a DC electric field is applied. The experiment cell is

then illuminated by a cold light source (see fig. 2.3). With the provision given in the experiment cell, the contact line region in the central part of the substrate is illuminated. The refracted light is magnified by a convex lens. To focus the contact line region during the experiment, a linear actuator (which is controlled by a computer) is used in moving the experiment cell (see linear actuator in fig. 2.3). Then the contact line is imaged (after optical reflection and diffusion) with the help of a monochrome camera and the images are saved.

2.2.5.   Characteristic speeds of receding contact line
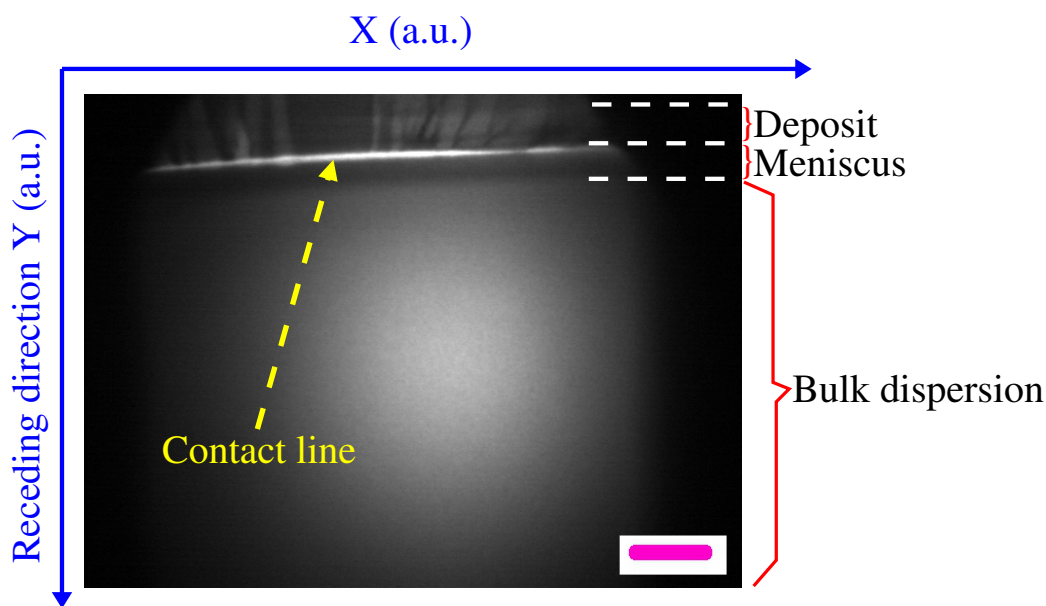
Figure 2.4: An image of the central part of the substrate when the experiment is in progress (front view). The bright region is the contact line (indicated by dashed arrow). Within our experimental conditions, three regions can be identified in the sequential images. The contact line separates the region of deposits and the bulk dispersion region. Gray level below the contact line has different values and it might be meniscus region. Scale bar is 1 mm (one pixel corresponds to 15 μm).

The sequential images are analyzed through homemade routines in Octave. An image of the central part of the substrate is shown in fig. 2.4. The bright region is the contact line and it has started to recede downwards (in the direction of the Y axis). The contact line separates the region of deposits and the bulk dispersion region which is shown in the figure. Below the contact line, gray level has different values and it might indicate the meniscus region. From an initial frame, the contact line (in Y direction) is approximately detected. One pixel corresponds to 15 μm and it varies slightly (± 5 μm/pixel) for different experiments. The measured position of the contact line is included in the routine. By finding the maximum along the horizontal line (along X direction in fig. 2.4), the contact line is reconstructed. From the consecutive frames, the position of the contact line as a function of time for one particular horizontal location (X in fig. 2.4) can be calculated. The speed of the contact line is then obtained for every position and time. If the contact line is pinned, it's speed for that position and time becomes zero. To obtain the statistical information of the data, we used R language. A plot of normalized probability

density function for the contact line speeds is shown in fig. 2.5–left. Cumulative histogram of speeds are built and the characteristic speeds are calculated by fitting the cumulative histogram with a sum of Gaussian distribution functions (fig. 2.5–right). Here we used two functions (shown in red an blue colors). The mean value of each distribution represents the characteristic speed. The standard error of the fitting is the error in obtaining the characteristic speeds. For each initial concentration, the characteristic speeds are calculated and are plotted as a function of applied electric field. The results are discussed in the next chapter. Details for constructing histograms and Gaussian fits are explained in [32].
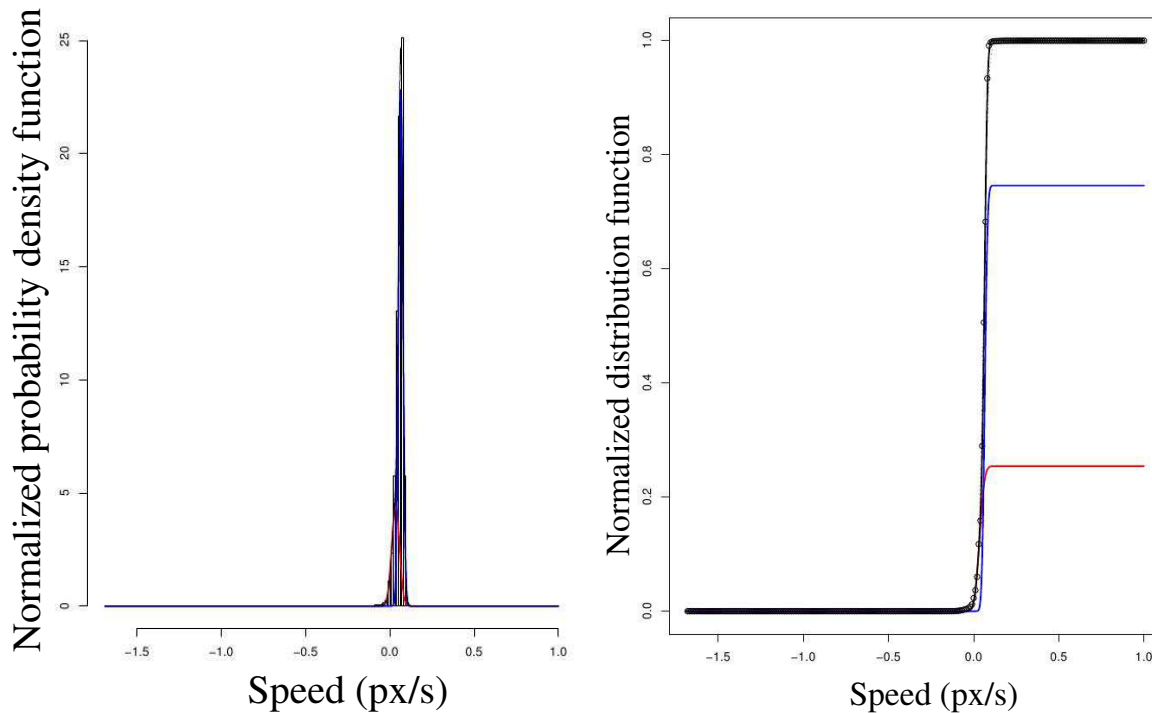
Figure 2.5: (left) Normalized probability density function for the contact line speeds for every position and time. (right) Gaussian fits for the cumulative histogram of speeds (represented in blue and red colors).

2.3.   Deposit morphology and "microscopic" average speed of receding contact line

The colloidal dispersion used for the experiments is the same as the one presented in sub-section 2.2.1.

2.3.1.   Wet cleaning

The substrates used for the experiments are the same as the ones given in sub-section 2.2.2. Compared to the previous experiments (macroscopic measurement), here the substrates are

cleaned with different composition of piranha solution as well as longer cleaning time to have increased hydrophilic character of the substrate. As explained in the sub-section 2.2.2, the substrates are cleaned with acetone and the procedure remains eventually the same. For the soft surface etch, the piranha solution of composition 5:3:1 (H_2O:NH_4OH:H_2O_2) is used and the substrates are cleaned at 66°C for forty minutes. Then they are rinsed with ultra pure water and dried with nitrogen gas blow.

2.3.2. Experiment
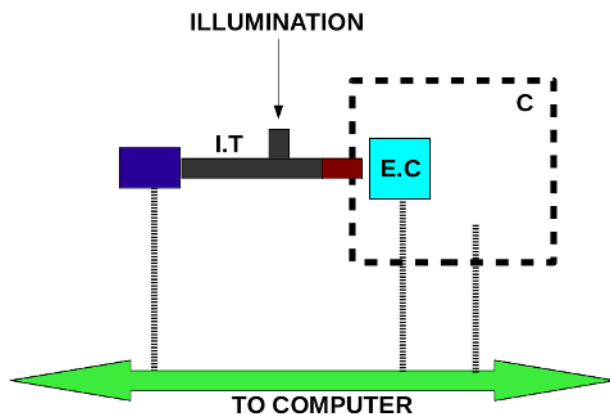
Figure 2.6: Microscopic measurement of receding contact line with DC electric fields. E.C – Experiment cell, C – Chamber, I.T – Imaging tool (Blue – CMOS camera, Grey – Infinity® long working distance microscope, Red – Mitutoyo objective of magnification 10×.)
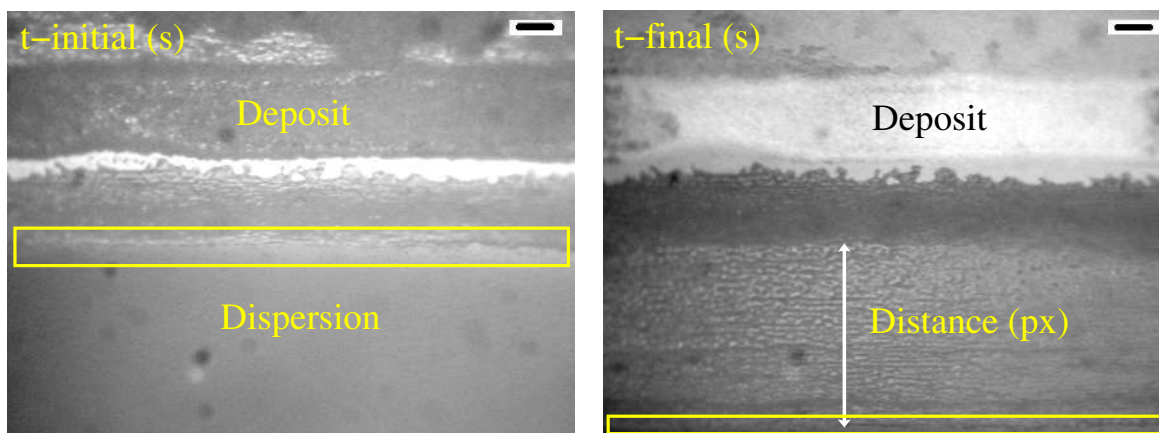
Figure 2.7: (left) Snapshot of the contact line region, say at t=0. Contact line is seen inside the rectangle which separates the dispersion region and the deposit region. (right) Snapshot of the contact line region, say at t=t_{end}. The contact line has receded and the distance can be measured directly from the images. By measuring the time difference, the average velocity can be calculated. Scale bars are 25 μm (one pixel corresponds to 0.31±0.01 μm).

The experiment cell used for the experiments is the same as the one shown in sub-section 2.2.3. The sketch of the experiment setup is shown in the fig. 2.6. The sequential images, temperature and humidity inside the chamber are acquired using a computer. Temperature inside the chamber is maintained at 63°C and the humidity is controlled (20% RH). Procedures for mounting the experiment cell and loading the dispersion are similar to the experiments of the previous section (sub-section 2.2.4). External DC electric fields are of the order of 1 V/mm and they are applied perpendicularly to the conducting substrates. The contact line is tracked microscopically using imaging tool (I.T in fig. 2.6). The imaging tool (I.T) is attached to X–Y translation stages for positioning. With the help of X–micro positioning the contact line is directly identified (and focused) and the sequential images are captured. Snapshots of the contact line region is shown in fig. 2.7. The contact line region can be seen inside the rectangle of fig. 2.7–left. This initial frame is kept as a reference to measure the initial time and position of contact line (from the stored sequential images). After some time, the contact line receded to a new position (fig. 2.7–right). The time for this contact line position is noted. From the final frame, the length of the particular deposit of colloidal particles is measured in pixels (using gimp) and then it is scaled to standard units (micrometers). From the calculated length and the time, the average velocity of the contact line can be measured. Pinning-depinning of the receding contact line is observed in our experiments; however, such instances are not taken into account while calculating the average velocity of the contact line.

2.4.   Colloidal cluster array on non patterned substrates
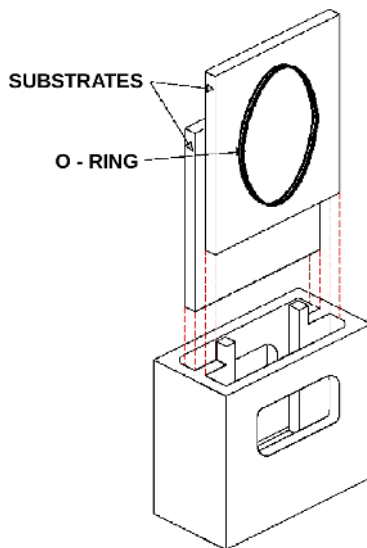
Figure 2.8: Sketch of the experiment cell used to obtain colloidal clusters. Sketch obtained from Dr. M. Giuliani.

The experiments presented in this section are different compared to the experiments explained previously (refer 2.2 and 2.3). Here the experiments are done at ambient conditions (room temperature and humidity) which result in minimal evaporation of the colloidal dispersion. The

contact line region is observed while the alternating electric fields are applied. The colloidal dispersion and the substrates used for the experiments are same as the one given before (subsections 2.2.1 and 2.2.2). Here we use the colloidal dispersion of concentration 0.5% w/w for all the experiments. As received ITO substrates (purchased from Visiontek systems) are dry cleaned with nitrogen gas blow to remove dust.

2.4.1.   Experiment cell

A different experiment cell (fig. 2.8) made of Teflon is used for the experiments. The design itself has interior protrudes which act as spacers between the two substrates. The distance between the substrates is of 1 mm. Ceramic spacers (one side is conducting) are kept between the substrates. Thus the conducting side of the spacers makes contact with the conducting side of the substrate (ITO). Suitable rubber O–rings are used to hold the components tightly.

2.4.2.   Experiment
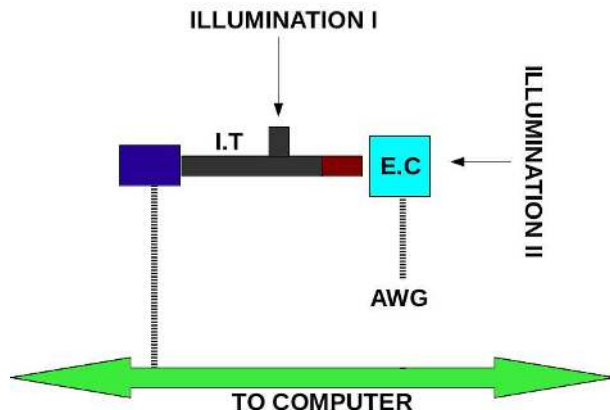
Figure 2.9: Experiment setup used to obtain colloidal clusters with alternating electric fields. E.C – Experiment cell, I.T – Imaging tool (Blue – CMOS camera, Grey – Infinity® long distance working microscope, Red – Mitutoyo objective of magnification 10×), AWG – Arbitrary waveform generator.

The experiment cell is mounted with dry cleaned ITO substrates. Electrical contacts are checked prior to the experiments. The colloidal dispersion is ultrasonicated for fifteen minutes and 120 μl of the dispersion is loaded into the experiment cell. The contact line region is directly identified by the imaging tool. An arbitrary waveform generator is used to apply alternating fields. A schematic of the experiment setup is shown in fig. 2.9. Weak alternating electric fields of square wave form (of the order of 1 Vpp/mm and frequency of the order of 1 Hz) are applied perpendicularly to the substrates. Using the microscope with an objective of magnification 10×, the contact line region is observed. The microscope is attached to a complementary metal oxide semiconductor (CMOS) camera for capturing sequential frames (see fig. 2.9). The central part of the contact line region is observed with a field of view of 0.6 mm; however the cluster formation is common to the entire contact line (far from the boundaries).
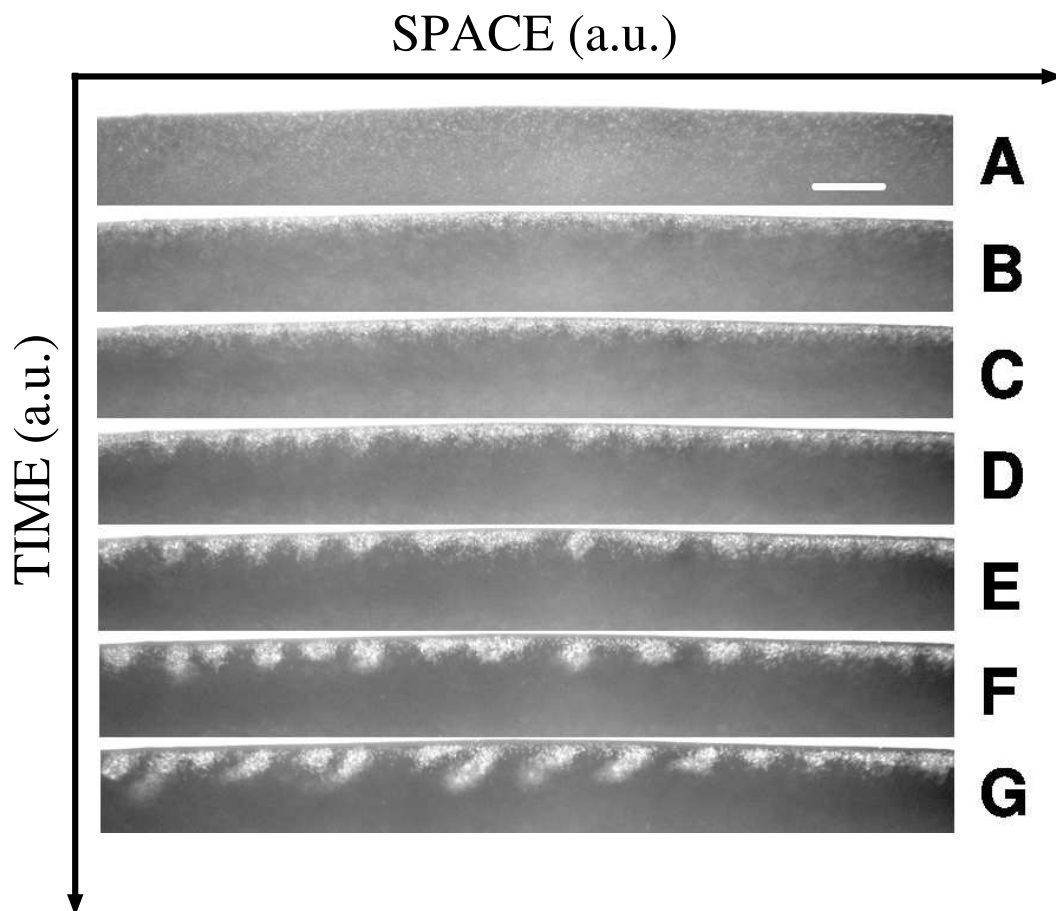
Figure 2.10: Snapshots of the contact line region (front view) while applying an alternating electric field of 1.8 Vpp and 0.8 Hz. The bright regions are particles or clusters. The frames are captured at an interval of one minute. Scale bar is 50 μm (one pixel corresponds to 0.31$\pm$0.01 μm).
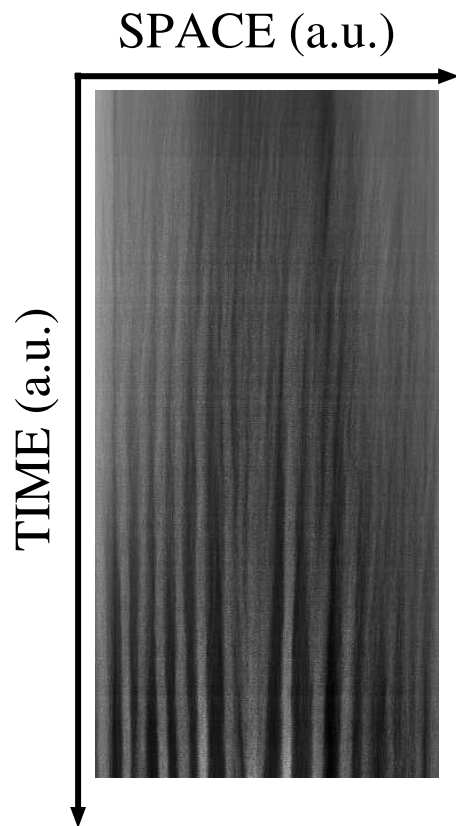
Figure 2.11: Space-time diagram calculated for 4100 sequential frames of an experiment. Applied field: 1.8 Vpp and 0.8 Hz. Bright regions are particles or clusters.

2.4.3. Measurements
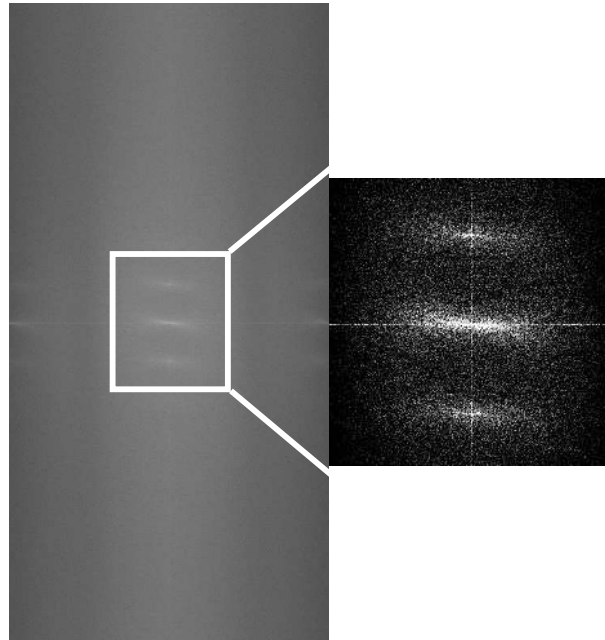
Figure 2.12: Two dimensional fast Fourier transform for 4100 sequential frames of an experiment. Applied field: 1.8 Vpp and 0.8 Hz. Fourier peaks are shown in the magnified portion.

The sequential images are analyzed using homemade routines in Octave. First we measure the time period of clusters. Snapshots of the contact line region are shown in fig. 2.10: A–G are obtained while applying an alternating electric field of 1.8 Vpp and 0.8 Hz. The snapshots (A–G) are discussed in the following chapter. The bright regions are particles or clusters. Snapshots are captured at intervals of one minute. An example of the space-time diagram is shown in the fig. 2.11 which is obtained for 4100 sequential frames. Mean along the Y direction (space) is obtained for each frame and thus the space average and time average are calculated for a given experiment. The frames are captured at a rate of 13 fps (in this case, the applied frequency is 0.8 Hz and for applied high frequencies, the frames are captured at high rates, e.g. 30 fps for 3 Hz). Then two dimensional fast Fourier transform is obtained from the space-time diagram. Corresponding Fourier image for these frames is shown in fig. 2.12. From the Fourier peak values (see magnified portion in fig. 2.12), the total number of sequential frames (4100) and the frame acquisition rate (13 fps), the frequency of the clusters can be calculated. In the experiments, for the applied low frequency, the clusters move as a whole up and down. For a pixel width horizontal line (mean along the Y direction) over these clusters, the intensity variations inside the clusters correspond to the frequency of oscillation of the clusters. The frequency of the clusters are then plotted as a function of applied frequency for different amplitudes. Also, from this sequential frames, the time at which the clusters start to age/dissociate can be found. These values are plotted as a function of applied frequency for different amplitudes. The results are discussed in the next chapter.

The mean spatial distance between the clusters (see fig. 2.10–F) can be calculated through spatial auto-correlation function. To obtain the mean spatial distance, we used the space-time

diagram which is calculated by doing a mean along the Y direction (space). We measure this characteristic length, $\bar{\lambda}$ before the clusters start to dissociate. The auto-correlation plot for an experiment of the applied field 1.8 Vpp and 0.8 Hz is shown in fig. 2.13. From this kind of plots, first local maximum in lag values is obtained for respective experiments and they are converted to standard units (micrometers). Mean characteristic length ($\bar{\lambda}$) is plotted as a function of applied frequency for different amplitudes. The results are discussed in the following chapter.
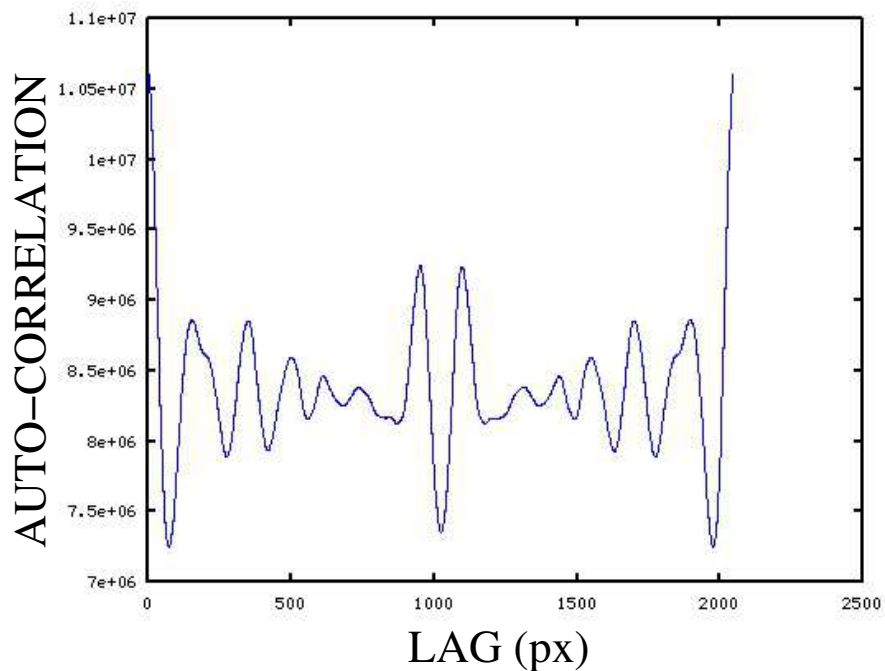
Figure 2.13: Plot of the auto-correlation function for an experiment of the applied field 1.8 Vpp and 0.8 Hz. The lag value corresponding to first local maximum is measured (in this case, it is 153 px), then it is converted into micrometers.

Chapter 3

Results and discussion: Vertical deposition experiments

3.1. Outline

Colloidal particles behave as an effective source to build multiple scale structured materials from colloidal dispersions. In this chapter, the influence of DC and AC electric fields on dilute colloidal dispersion is presented. The studies are mainly related to the contact line region of a colloid (vertical deposition experiments are performed inside a thermal chamber maintained at 63°C as well as in the room temperature). Also, the behavior of the contact line is outlined. Effect due to the field on particles is discussed. Experimental evidence on the formation of a colloidal cluster array at a three phase contact line is highlighted.

3.2. Vertical deposition with DC electric fields

Giuliani *et al.* [19] reported the vertical deposition method using dilute polystyrene colloidal dispersion to obtain colloidal crystals. They mainly study the speed of the receding contact line for varying initial concentrations and concluded that a region near the contact line can be influenced to tune the depositing colloidal particles, and its morphologies. In our case, the experiments are performed to influence the region near the contact line by applying electric fields during the process of deposition.

In vertical deposition of colloids, there are important parameters which need to be controlled to fabricate homogeneous colloidal crystals. Of which, some of the variables are available for tuning while the experiment is in progress.

Concentration: The concentration of the colloidal dispersion inside the experiment cell is neither homogeneous nor constant along the whole experiment. The particles accumulate in a region near the free surface (contact line region) as the continuous phase (in our case, ultra pure water) is evaporated. This region is called as Particle Pool Zone (PPZ) [8, 19]. The formed morphology of particles depends on the local concentration of particles in the PPZ, rather than on the initial concentration; however, an increase in the initial concentration, obviously changes the concentration in PPZ. Influencing PPZ has a great advantage to tailor the morphology of depositing colloidal particles. In order to have a morphology with less number of particles per unit

area, the PPZ should have less number of particles. In experiments of high initial concentration, this is possible when one has the control over the PPZ concentration. This results in multiple kinds of morphology (morphologies with varying number of particles per unit area) in a single experiment of one initial concentration.

Flows: The fluid flows are important to consider, which are of different origin: (a) Marangoni flows due to the evaporation of fluid. In the vertical deposition configuration, evaporation of fluid is maximum near the contact line. The fluid that evaporates near the contact line is replenished by the fluid from bulk and the flows are generated. (b) Capillary flows due to the previously deposited structure which make the system dependent on its previous history. The hydrodynamic interactions between the particles [30] are important to consider. The movement of a given particle induces a flow in the continuous medium, which will have an effect on other particles, called hydrodynamic interactions. In the systems of thermal convective flows, this interactions can be neglected.

The motivation of these experiments is to deepen the understanding of some of these phenomena during the vertical deposition process. Earlier, the role of PPZ to the formed morphology was reported [19] in the absence of the external electric field. Concentration of particles in PPZ can be influenced by applying a weak DC field. This might affect the kind of morphology which will be explained in the following section.

When the fluid phase evaporates, the contact line recedes and the colloidal particles are deposited onto the substrate. Each morphology is associated with different speeds of contact line [19]. Capillary properties of the deposited morphology are related with the speed of contact line. In the following sections, different morphologies obtained during the experiments and its relation with contact line speed are explained. The experiments are performed with applied electric fields (weak DC fields) during the deposition process. The receding contact line is observed macroscopically as well as microscopically and the speeds are measured. The applied electric field has an effect on the colloidal dispersion *via* electrophoresis (estimation for this effect in our experimental conditions is given in the following section), which increases or decreases the particle concentration near the depositing zone.

3.2.1.   Observed morphologies

The concentrations used in our experiments lead to different kind of morphologies. They are divided into six major categories. Morphologies ranging from a sparse submonolayer (at 0.1%) to a multilayer deposit are shown in fig. 3.1. The thickness has been estimated from the step-wise intensity profile as it increases slowly from a monolayer. In the summary of morphologies shown in fig. 3.1, the images are arranged in such a way that the number of particles per unit area increases from left to right (first row of fig. 3.1: A, B and C). In all the cases (A to F), white area is the bare substrate and the dark regions are deposited colloidal particles.

Sparse submonolayer In fig. 3.1, morphology (A) shows that the particles are organized in a columnar-like arrangement. The column corresponds to sparse submonolayer deposit. These kinds of morphologies are observed in experiments of initial concentration 0.1%.

Non Compact (NC) In morphology (B) in fig. 3.1, named as non compact, the columns are extended enough to form a similarly sparse deposit which expands over the surface of the substrate. These typical dried deposits are mostly seen in the experiments of low initial concen-
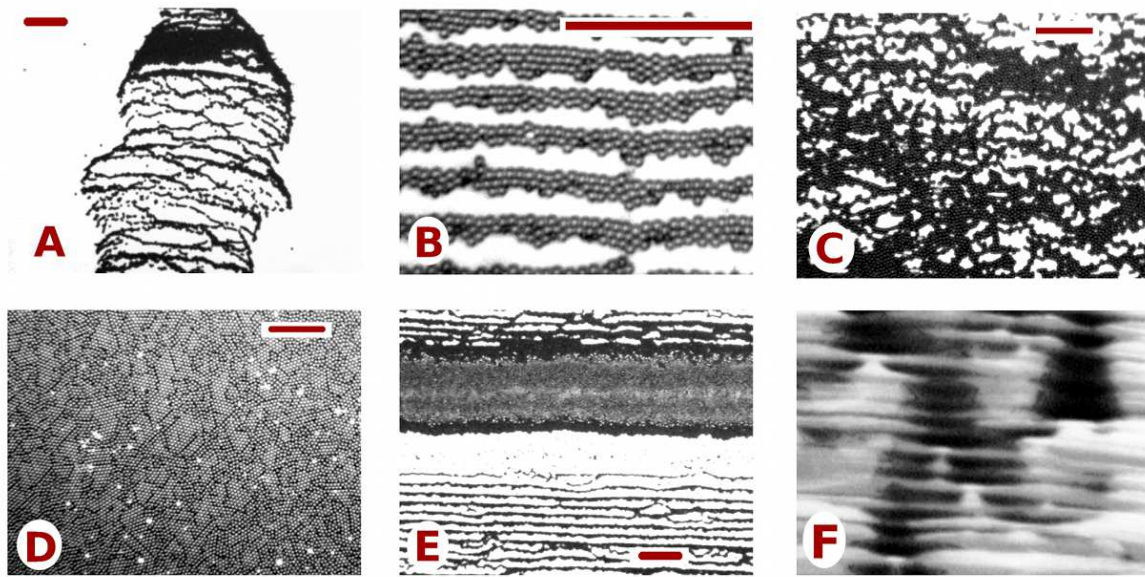
Figure 3.1: Optical micrographies of the several morphologies of the dried deposits of colloidal particles. A - Sparse submonolayer at 0.1%, B - Non compact morphology (NC) at 0.3%, C - Non compact dense morphology (NCD) at 0.5%, D - Compact monolayer (CM) at 0.5%, E - Multilayer (ML) followed by sparse deposit at 0.5%, F - Vertical column multilayer (VCM) at 0.5% (width of image is 6 mm). Scale bars are 25 μm (A - E). Figure reprinted from [101].

tration, from 0.1% to 0.3%.

Non Compact Dense (NCD) Morphology (C) in fig. 3.1 still shows a submonolayer deposit which extended over the substrate. The number of particles per unit area is increased when compared with (A) and (B). These morphologies are mostly seen in the experiments of initial concentration 0.3% and partially to 0.5%. NCD morphologies can be distinguished from NC morphologies by comparing the number of connecting network of particles to a single particle.

Compact Monolayer (CM) In compact monolayer (D) in fig. 3.1, the surface coverage on the substrate by particles reaches its maximum. Domains of ordered colloidal particles are seen which show that the deposit is poly-crystalline in nature. These morphologies are observed in the experiments of initial concentration 0.5%.

Multilayer (ML) and Vertical Column Multilayer (VCM) Structures with more particles per unit area are multilayer deposits which is shown in fig. 3.1 – E. These kinds of morphologies are seen at experiments of high concentrations, 0.5% and 0.7% . In some regions of high concentration experiments, structures with higher particle density are found. These structures arrange like vertical columns as shown in fig. 3.1–F, called Vertical Column Multilayer (VCM).

3.2.2.   Characteristic speed of receding contact line

For a structure or morphology to deposit on the vertical substrate, it is necessary to have the particles available near the depositing region. That is, to have a populated PPZ. Another dependency is on the kind of morphology that has already been deposited: normally a multilayer

which is forming has increasing capillary flows due to its porosity. Hence, a multilayer usually grows faster since the flows that drive particles toward the structure are larger [19]. The speed of the receding contact line depends on the previous history of the deposited morphology.

3.2.2.1. Deposition sketch
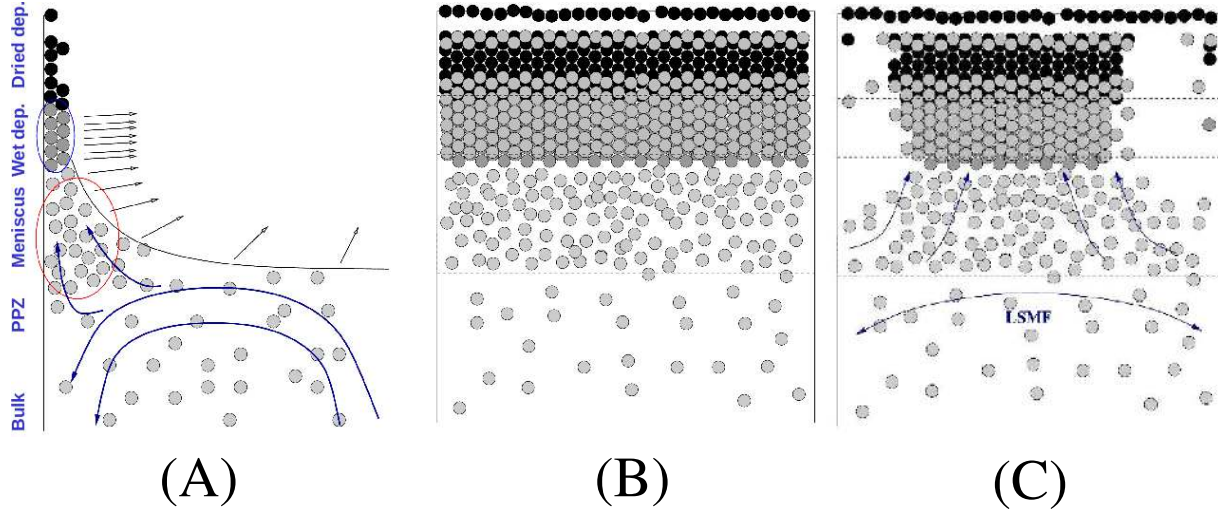
Figure 3.2: Sketch of the deposition of the colloidal particles onto a vertical substrate. (A) Lateral view – Different regions observed during the experiments; (B) and (C) Front view; (B) Formation of two layers; (C) Formation of vertical column multilayer and large scale mean flows (LSMF). Sketch is obtained from Dr. W. González–Viñas and it is modified.

Different observations during the experiments are sketched in fig. 3.2. The contact line recedes as the fluid phase is evaporating. The dried deposits of particles are obtained as the result of evaporation. To replenish the evaporated fluid, fluid from the bulk reaches the contact line region that carries the particles to the PPZ (fig. 3.2–(A)). These particles are then deposited onto the substrate (fig. 3.2–(B)). Electric field can influence the PPZ, as the field acts directly on the particles. The forming morphology depends on the concentration of particles in PPZ. If the number of layers are more in the wet deposit region, porosity from the deposits strengthen the capillary flows and in turn could bring large amount of particles for deposition. The actual amount of particles depends on PPZ in a localized region leaving the surrounding depleted with fewer particles. Consequently, the columns made of multilayers (higher particle density, fig. 3.1–F) are formed. Fig. 3.2–(C) explains the formation of column multilayers. Measuring lateral flows and large scale mean flows (LSMF) turns out to be a challenge and a command over these flows would provide a direct control on the deposition process.

Typical parameters in our experiments are similar as the ones reported in [32], which are

$$\rho \approx \rho_{water} = 1 \text{ g/cm}^3 = 10^3 \text{ Kg/m}^3 \ (\rho \text{ is the density})$$
$$\mu \approx \mu_{water} = 1 \text{ cP} = 10^{-3} \text{ Kg/(m·s)} \ (\mu \text{ is the viscosity})$$
$$\gamma \approx 1 \times 10^{-1} \text{ N/m} \ (\gamma \text{ is the surface tension})$$
$$L \approx 10^{-6} \text{ m} \ (L \text{ is the characteristic length})$$
$$V \approx 10^{-6} \text{ m/s} \ (V \text{ is the characteristic velocity})$$

$$\text{Re} = \frac{\rho V L}{\mu} \approx 10^{-6}$$

$$\text{Ca} = \frac{\mu V}{\gamma} \approx 10^{-8}$$

Density ρ is measured by weighing a known volume of dispersion. Surface tension γ is estimated by the pendant drop method [32]. The colloidal particles behave as inertial ones [102]. They approximately follow the flow. The capillary number (Ca) is of the order of 10^{-8}. Consequently, the capillary forces are stronger than viscous ones [32, 33].

3.2.2.2. Electrokinetic phenomena

The electric field interacts with the particles through several electrokinetic phenomena [103]. Of them, electrophoresis is reported as the strongest since it is directly related to the surface charge of the particle [104, 105]. Hence,

$$\vec{u} = \frac{q\vec{E}}{6\pi\mu r} \tag{3.1}$$

where $\vec{u}$ is the velocity of the particle, q is the effective charge of the surface of the particle (i.e. surface charge of the particle and the charge in the Stern layer) , μ is the viscosity of the fluid, $\vec{E}$ is the external field and r is the radius of the particles. The values for our experimental system are [32]

$$r \approx 0.7 \times 10^{-6} \text{ m}$$
$$Q \approx 4.4 \times 10^{-13} \text{ C}$$
$$\mu \approx 1 \text{ cP} = 10^{-3} \text{ Ns/m}^2$$
$$E \approx 1 \text{ V/mm} = 1 \times 10^3 \text{ V/m}$$

where Q is the surface charge of the particle. To estimate the electrophoretic effect [32], it is important to consider the Stern double layer effect as it screens the part of surface charge of the particle. To calculate the electrophoretic velocity of the particle, Smoluchowski approximation is used, valid for $kr \gg 1$ (k^{-1} is the Debye length). In our case, the particle radius r is 0.7 μm ($r \gg k^{-1}$). The approximation relates the electrophoretic mobility, μ_E with the Zeta potential, ζ [106].

$$\mu_E = \frac{\vec{u}}{\vec{E}} = \frac{q}{6\pi\mu r} \tag{3.2}$$

$$\zeta = \frac{Q}{4\pi\epsilon_m\epsilon_0 r(1 + kr)} \tag{3.3}$$

$$\mu_E = \frac{\epsilon_m\epsilon_0\zeta}{\mu} \quad \text{(Smoluchowski)} \tag{3.4}$$

where ϵ_m is the dielectric constant of the suspending medium, ϵ_0 is the permittivity of vacuum, μ is the dynamic viscosity of the suspending medium and ζ is the zeta potential.

$$\vec{u} = \frac{\vec{E}\epsilon_m\epsilon_0\zeta}{\mu} \quad \sim 10^{-5} \text{ m/s} = 10 \ \mu\text{m/s} \tag{3.5}$$

With the velocity of 10 μm/s, the particles can cover the distance between the two electrodes (electrode spacing is 1 mm) in 100 s [32]. Consequently this mechanism plays a dominant role during the initial part of the experiment and in particular, when the electric field is turned on with the dispersion loaded in the cell. In our experimental conditions, electrophoresis produces an initial redistribution of particles in the direction of the applied electric field. Thus, the local concentration of particles is varied near the electrode region and it depends on the strength of the applied electric field. Concentration of particles increases in the positive electrode and it decreases in the negative one. In short, the characteristic speed of receding contact line can be modified by changing the particle concentration in the PPZ [8, 19].

Other electrokinetic mechanisms like dielectrophoresis, electro-osmosis, streaming potential, sedimentation potential, electrowetting can be relevant in our experimental system. Estimated values for these mechanisms under similar experimental conditions are explained in [32]. The electrophoretic effect is considered as the main consequence of the applied electric field [32]. Moreover, the electrophoretic effect has been proved as an efficient electrokinetic mechanism in transporting colloidal particles [104, 105].

3.2.2.3. Deposit morphology and statistics of the "macroscopic" speed of receding contact line

The experiments corresponding to the applied positive voltages are obtained from [32] (the experiments were performed by Dr. M. Giuliani). The results (experiments of positive voltages) are presented again to explain the observed behavior from the experiments of applied negative voltage.

Fig. 3.3, fig. 3.4 and fig. 3.5 show the characteristic speed of the receding contact line measured macroscopically for initial concentrations 0.1%, 0.3% and 0.5%, respectively for different applied voltages (of positive [32] and negative magnitudes). Despite the small change in the initial concentration, the effect of applied field on the characteristic speeds can be noted (comparing figures 3.3, 3.4 and 3.5). In the same experiment (at a given initial concentration and an applied voltage), two different characteristic speeds for the contact line (circles and squares in figures 3.3, 3.4 and 3.5) are measured. Recalling the morphologies observed in these kinds of experiments, the different characteristic speeds can be understood; however, with our experimental resolution we could measure only two different speeds of contact line. The two characteristic speeds represent the formation of different kinds of morphology in the same experiment. As the PPZ supplies particles for deposition, different speeds of contact line depend on the local conditions in the meniscus.

3.2.2.3.1. Low concentration   At low concentration (0.1%), a decrease in voltage increases the characteristic speed of the contact line (squares in fig. 3.3). In some experimental conditions, an additional speed is measured (circles, fig. 3.3). For the applied positive voltage [32], effects due to the electric field in speed of contact line are difficult to understand. The morphologies observed in these cases (for applied positive and negative voltages) are always similar (NC). This points out that the concentration of particles in PPZ brought by electrophoresis is not enough to form dense or compact morphologies (NCD and CM).

In the negative voltage region, we have depleted PPZ and the expected kind of morphology
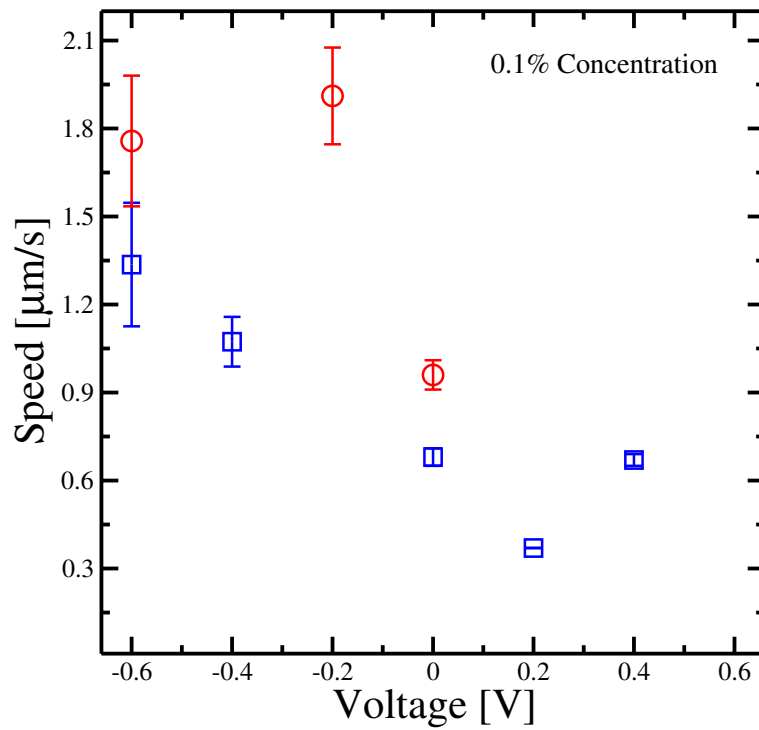
Figure 3.3: Characteristic speeds of the receding contact line for 0.1% initial concentration at different applied voltages. Circle and square in a given condition represent the different characteristic speeds observed in the same experiment.

can be of non compact or sparse deposits. From the substrates, morphologies of low particle density per unit area are obtained and they are given in a columnar arrangement (fig. 3.1–A). This shows that the decrease in concentration of particles in PPZ does not further decrease the particle density in the NC morphology but directs a transition in the morphology which is of columnar and sparse deposits. Under these experimental conditions, the meniscus region is highly depleted and the PPZ has less number of particles. Few particles could be pulled towards these columnar sparse morphologies resulting the neighboring regions without particles. Microscopic measurement or localized observation of the contact line would give more information about the formation of these columnar sparse deposits. The columns found in applied negative voltage region are not observed before in the experiments (without electric field) reported in [19]. One reason could be due to the number of particles in PPZ because in our case, due to the negative voltage, the particles are repelled from the substrate and consequently the PPZ depleted.

Figure 3.4: Characteristic speeds of the receding contact line for 0.3% initial concentration at different applied voltages. Circle and square in a given condition represent the different characteristic speeds observed in the same experiment.

3.2.2.3.2. High concentrations Characteristic speed of receding contact line at high initial concentrations of colloidal dispersion are shown in fig. 3.4 and fig. 3.5. The observed morphologies in these experiments (0.3% and 0.5%) are previously defined: ML and NCD (which tend to grow at faster rates, so high speed of contact line), and CM and NC (which tend to grow at lower rates). In particular, a higher number of compact morphologies like multilayers and monolayers are observed in high concentration experiments. Also, we obtain another kind of morphology, in which the colloidal particles are arranged in a columnar way, where the density of particles per
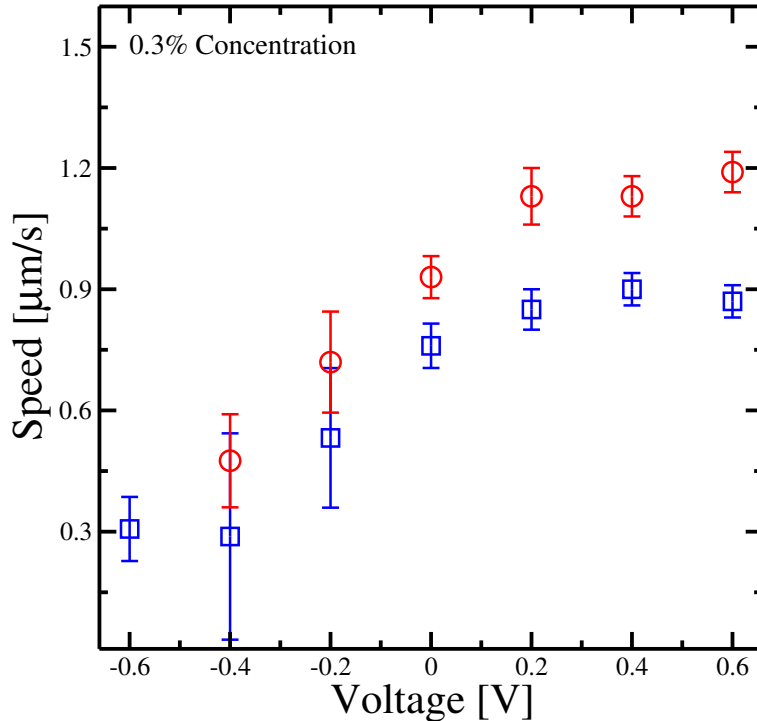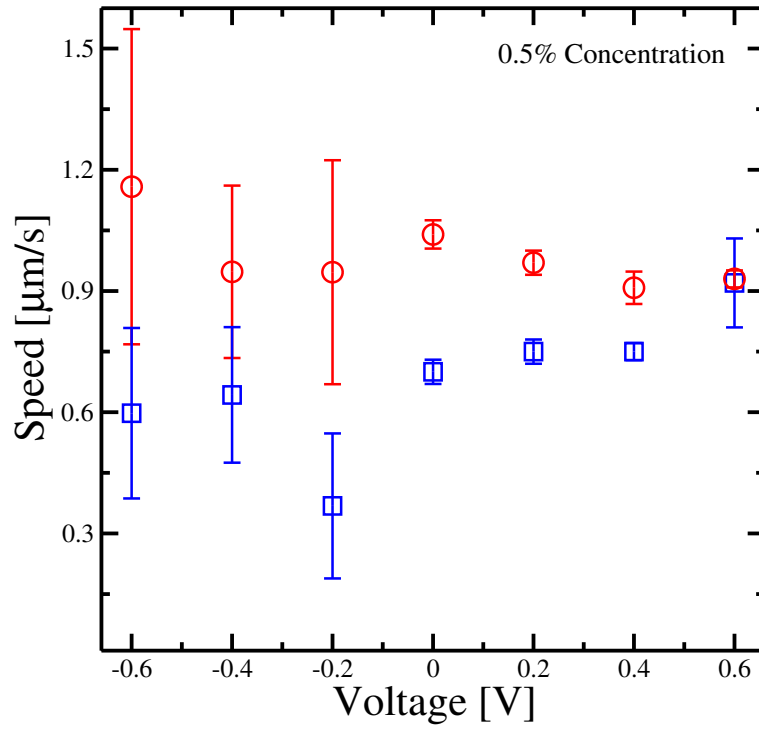
Figure 3.5: Characteristic speeds of the receding contact line for 0.5% initial concentration at different applied voltages. Circle and square in a given condition represent the different characteristic speeds observed in the same experiment.

unit area reaches its maximum (see fig. 3.1–F). Experiments (see fig. 3.5) performed at relatively high voltage (0.4 and 0.6 V) and high concentration (0.5%), result in abundant formation of Vertical Column Multilayer (VCM).

For the initial concentration 0.3% (fig. 3.4), the characteristic speeds of the contact line (both circles and squares) remain unchanged in the applied positive voltage region [32]. But they decrease as the voltage decreases . In the positive voltage region, we see saturated speeds of contact line (fig. 3.4–right side). Compared to the experiments of concentration 0.1% (positive voltage region), large concentration of particles in PPZ is induced by the electrophoretic effect as the particles are negatively charged. This results in more particles which are available for deposition (in the substrate of positive voltage) that not only increase the speed of contact line (relative to the negative voltage region of 0.3%), but also increase the area covered by multilayers. Multilayers are associated with large speed of receding contact line [19, 32]. Thus, large concentration results in thicker deposits where the additional particles are deposited. In the negative voltage region (fig. 3.4–left side), the PPZ is depleted due to the electrophoretic effect. Consequently, it affects the deposits of colloidal particles and the speed of receding contact line. The kind of deposited morphology remains similar, NC (positive voltage region of 0.1%, fig. 3.3). These kinds of deposits are associated with low speeds of contact line [19].

A different behavior is observed at high initial concentration (0.5%) experiments, where the two characteristic speeds of contact line overlap at 0.6 V (see fig. 3.5). They diverge towards the zero field. In this positive voltage region, the high characteristic speed (circles) decreases slightly (for increasing applied voltage), and the lower one (squares) increases until they overlap at the applied voltage of 0.6 V. The obtained morphologies are complex with alternating columnar like structures (fig 3.1–F). The simultaneous formation of morphologies with different growth rate could affect the characteristic speeds leading to the observed overlap.

If we move on the negative voltage region, the characteristic speeds (both circles and squares) remain constant within the error (fig. 3.5). The higher characteristic speeds (circles in fig. 3.5, negative voltage region) are similar to the speeds (squares and circles in fig. 3.4) observed in positive voltage region of the 0.3% experiments. The concentration of particles in PPZ for negative voltage region of 0.5% decreases due to the electric field, thus both experimental conditions could be comparable (experiments from positive voltage region of 0.3% concentration, fig. 3.4 with the negative voltage region of 0.5% concentration, fig. 3.5).

While performing the preliminary experiments to measure the receding contact line macroscopically, we noted an inconsistency in some experiments (not reported) related with the loading of dispersion. To minimize the effects from loading procedure, the experiment cell is placed in the same position during the dispersion loading for all the experiments. After loading, the cell is moved into the thermal chamber in the same way without tilting or disturbing.

3.2.2.4. Deposit morphology and "microscopic" average speed of receding contact line

In the previous section, macroscopic statistical measurement of the speed of the receding contact line is presented. Morphological formation of multilayers and vertical column multilayers are complex to understand from the macroscopic measurement. Micron length scale observation of contact line and its dynamics could help in understanding the deposition process in a better
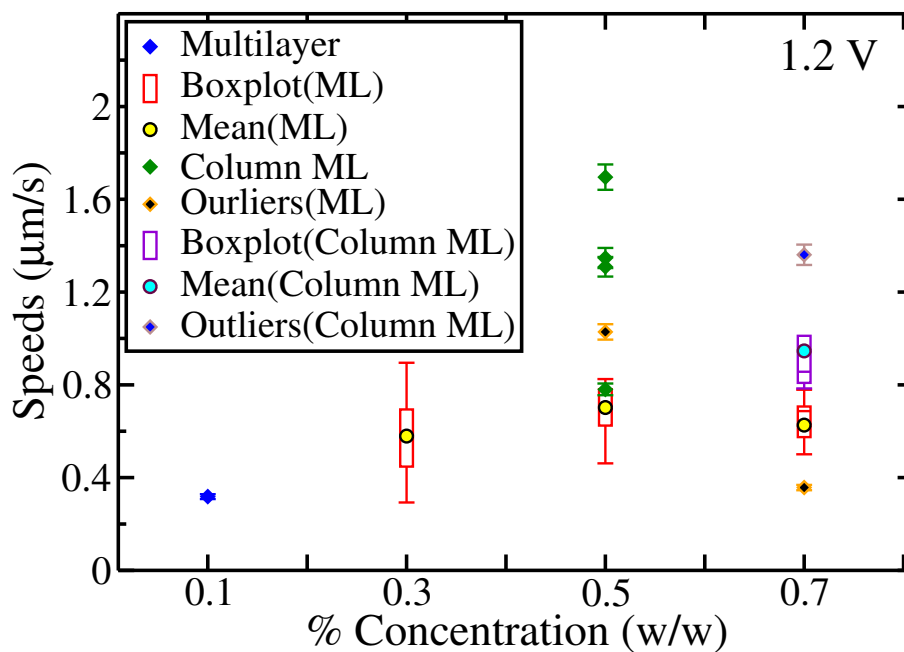
Figure 3.6: Microscopic measurement of receding contact line at an applied field of 1.2 V as a function of initial concentration.

way. The microscopic measurement of receding contact line for these kinds of morphologies is highlighted and qualitative information is presented in the following.

Compared to the experiments of previous section and [19], here the experiments are performed at different experimental conditions. Firstly, we change the substrate cleaning procedure to have increased hydrophilic character (see section 2.3.1). Secondly the humidity inside the thermal chamber is controlled (20% RH). Consequently, at constant temperature (63°C), the evaporation rate of the fluid is slower and hence the receding contact line can be followed, microscopically, easier. Importantly, the measurement procedure (see section 2.3.2) for receding contact line differs from the measurement procedure of previous section and [19].

As said before, morphologies like multilayers and column multilayers (fig. 3.8–right) are abundant at high initial concentration and high applied field. Microscopic measurement of receding contact line at 1.2 V as a function of initial concentration is shown in fig. 3.6. The area of observation follows the receding contact line and the observation is far from the boundaries (experiment cell walls). Box-plots are constructed to give collective representation of individual speed value.

In fig. 3.6, though the initial concentration is relatively low (0.1%), a multilayer morphology is observed. The multilayer morphology at this concentration could be due to the high applied field 1.2 V, which completely modifies the properties of PPZ. The morphology might be of this kind as shown in fig. 3.7 which may lead to the observed low speed of contact line (fig. 3.6).

Increasing the initial concentration, enriches the PPZ with particles. In turn, multilayer morphologies are formed and the mean speed of contact line increases (yellow filled circles in fig. 3.6). At high concentration (0.7%) the mean value decreases. A possible reason could be due to the substrate at the back, where the PPZ is depleted. The receding of contact line at back substrate is of different speed while the contact line in front substrate recedes at high speed. This

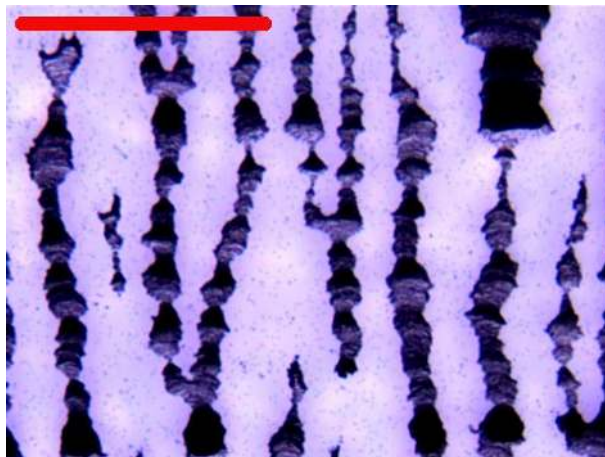Figure 3.7: Optical micrograph of sparse stripes obtained at 1.2 V and initial concentration of 0.1%. Scale bar is 500 μm.
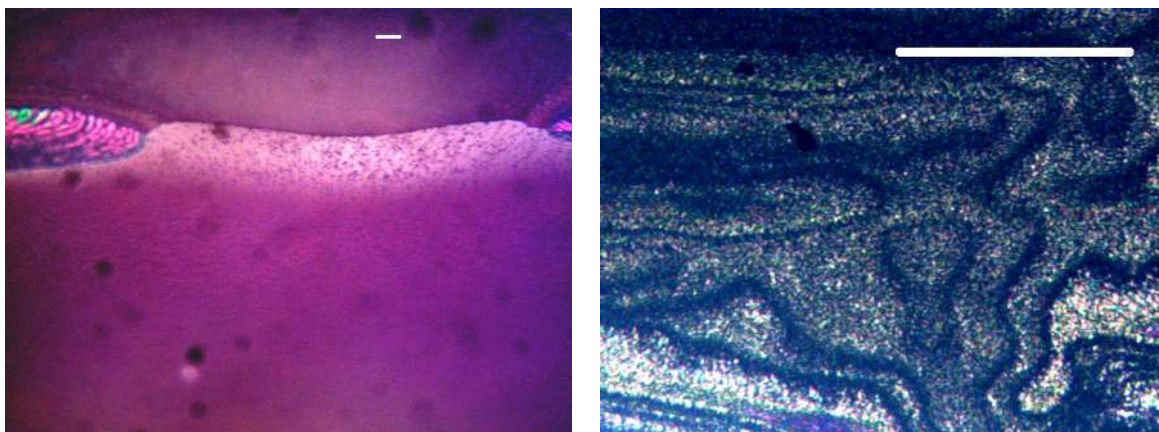

Figure 3.8: (left) Snapshot of the contact line receding downwards while forming a column multilayer at 1.2 V and initial concentration of 0.7%. Scale bar is 25 μm. (right) Optical micrograph of column multilayer obtained at 1.2 V and initial concentration of 0.7%. Scale bar is 500 μm.

might produce a unbalance situation with which the pinning-depinning of contact line occurs, which has to be studied extensively. Column multilayers are forming frequently at high initial concentrations. Snapshot of the contact line region during the application of the field is shown in fig. 3.8–left. The contact line (bright region) recedes downwards while forming a column multilayer at an applied field of 1.2 V and initial concentration of 0.7%. At 0.5% concentration (see fig. 3.6), obtained column multilayers have different speeds. This can be due to the different condition in PPZ. However, in both concentrations (0.5% and 0.7%) the obtained speeds for column multilayers are higher than those of the multilayers. With a positive applied voltage and high concentration, there are more particles in the PPZ and localized lateral flows [21] could be stronger towards the contact line that in turn bring more particles to deposit. Thus, the column multilayers are formed with high speeds of contact line.

The qualitative explanation gives the information about the role of initial concentration and high applied field (together with the change in experimental conditions like substrate character, relative humidity and mode of observing the receding contact line). More experiments have to be performed to evaluate the influence of electric fields on the deposition process. As the measurement of contact line is in microscopic length scale, each forming morphology of colloidal particles is influenced by the previously deposited colloidal particles. While presenting the collective representation for the speed of contact line, those previously deposited particles has to be considered. Also, in this microscopic scale, we could observe the interactions between the particles due to the applied field. Experiments on colloidal dispersion with evaporation cause convection flows which are difficult to take into account. To simplify this problem, similar experiments can be performed at room temperature with electric fields. As a first step, the contact line region is observed at microscopic length scale while the alternating electric fields are applied.

3.3.   Colloidal cluster array on non patterned substrates

Summarizing the experimental conditions, here, the experiments are done at room conditions and applying weak AC electric fields. The meniscus of a colloid with a free surface is focused. The experimental conditions are selected in such a way that there is minimal evaporation of the solvent (ultra pure water). This prevents the receding of the contact line during the measurement time.

The aim of these experiments is to get insights on the mechanisms involved in colloidal cluster formation and their evolution. In these experiments, we study mainly three relevant aspects.

* The response of clusters to the applied field.

* The evolution of the system by measuring the time required for cluster formation and aging of clusters.

* The horizontal spatial distribution of clusters.

3.3.1.   Mechanisms

Comparing with the electrohydrodynamic instabilities reported [107, 108], the observed phenomena in these experiments are due to electrokinetic and electrowetting [51, 54] mechanisms.

Electrophoresis (section 3.2.2.2) is an efficient mechanism in transporting the particles [104, 105] and when it acts on the dispersion, it forms a concentration gradient. Thus the effect results in a high concentration of particles near the contact line region, which is greater than the initial concentration (0.5%, in this section). This increased concentration of particles near the contact line is observed in the experiments. Particle tracking methods could be employed to identify the particles and consequently the concentration near the contact line can be obtained.

The accumulated particles near the contact line (due to electrophoresis) act as an dielectric layer between solid (substrate) and the dispersion. Electrowetting occurs, an effect that varies the mean contact angle of dispersion due to the applied electric field. Estimated values for this effect are obtained from similar experimental conditions [32] and they are given below.

The change in contact angle due to the electrowetting can be estimated by the equilibrium condition for a parallel-capacitor [51].

$$\gamma_{LV}\left(cos\theta - cos\theta_0\right) = \frac{1}{2}\frac{d}{\epsilon_0\epsilon_r}\sigma_L^2 \tag{3.6}$$

where γ_{LV} is the free energy between the liquid/vapor interfaces without electric field, and ϵ_0 and ϵ_r are the permittivity of vacuum and the dielectric constant of the dielectric layer of thickness d, respectively. By using Gauss law, $\sigma_L = \epsilon_0\epsilon_r\frac{V}{d}$. Electrowetting force is $\gamma_{EW} = \frac{1}{2}\frac{d}{\epsilon_0\epsilon_r}\sigma_L^2$. Equation 3.6 can be rewritten as a function of the voltage difference between electrodes and hence,

$$\left(cos\theta - cos\theta_0\right) = \frac{\epsilon V^2}{2\gamma_{12}d} \tag{3.7}$$

where θ and θ_0 are the equilibrium contact angles with and without electric field, respectively; $\epsilon = \epsilon_0\epsilon_r$; γ_{12} is the surface tension between the fluids (in our case they are dispersion medium and air); and d is the thickness of the dielectric layer (accumulated colloidal particles). This approximation presents an order of magnitude of the influence of electric field over the system. We consider ϵ to be between the permittivities of polystyrene and water, i.e. 25 to 100 times of ϵ_0. Hence the change in the equilibrium contact angle due to the applied field is

$$\left(cos\theta - cos\theta_0\right) = \frac{\epsilon V^2}{2\gamma_{12}d} \approx \frac{[10, 10^3] \times 10^{-12}\frac{N}{V^2} \times 1V^2}{10^{-7}N} = \left[10^{-4}, 10^{-2}\right] \tag{3.8}$$

Reported equilibrium contact angle in the absence of the electric field for similar kinds of colloidal dispersion is in the interval from 30° to 50° [32]. On applying the electric field, from former estimation we can assume the maximum change in the contact angle is about 1% (a change of 0.5° if we consider θ_0=45°) [32]. For the alternating electric field, the mean contact angle increases as well as decreases. This small variation in contact angle induces local flows that form clusters. This is explained in the following section. Contributions from both effects (electrophoresis and AC electrowetting) set a forcing threshold to obtain clusters. Under these conditions, the interparticle interactions may play an important role in transport properties [109–111]. We focus on a region of the experimental parameter space where clusters form; however other forcing conditions may also form clusters, but the clusters are smaller in dimensions. We obtained them in our preliminary experiments (not reported). Further studies have to be performed to define this threshold condition of cluster formation and the experimental parameter space as they will help in constructing a phase diagram which may specify the region of cluster formation.

3.3.2. Cluster formation
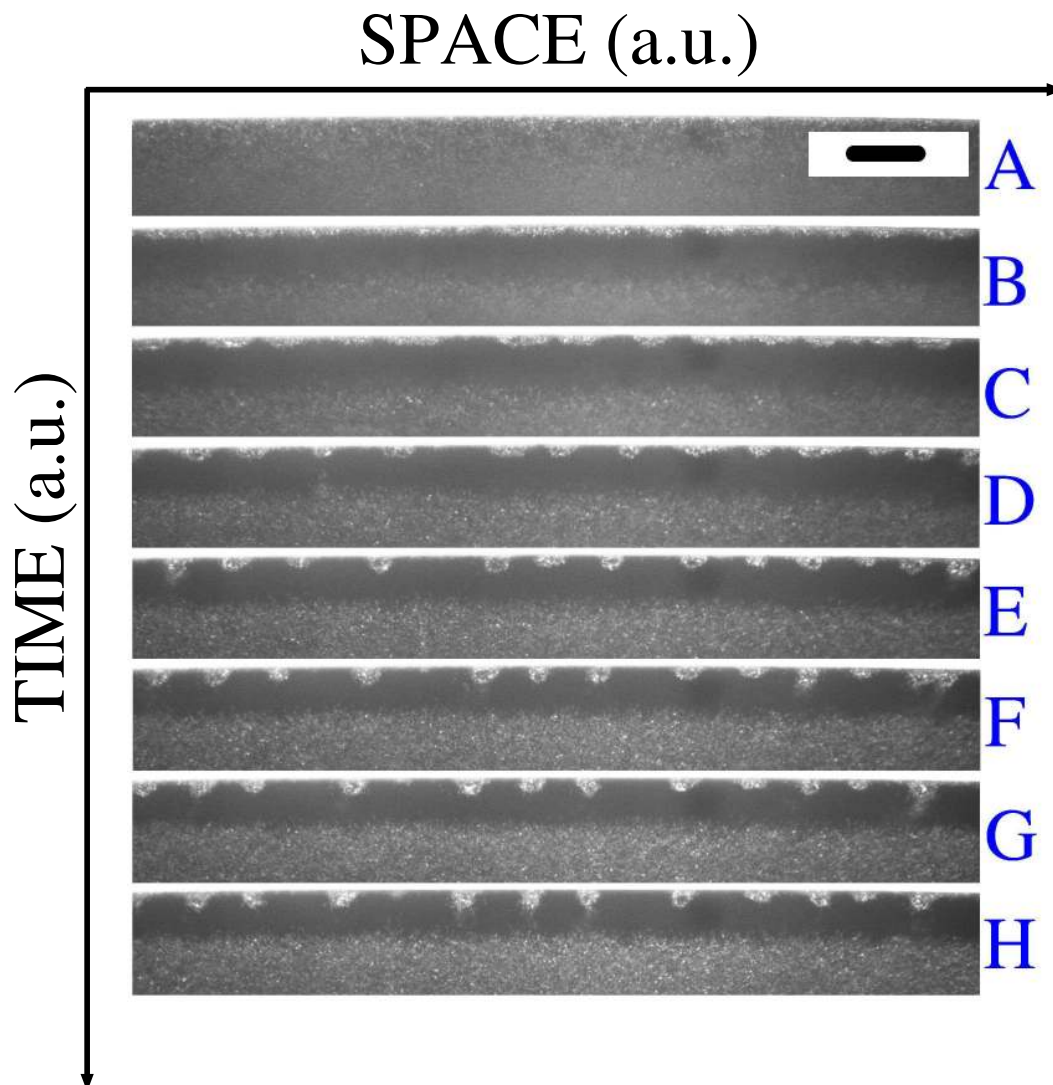
Figure 3.9: Snapshots of the contact line region (front view) at 2.2 Vpp and 3 Hz. The bright regions are particles or clusters. The frames are captured at an interval of two minutes and the scale bar is 50 μm.

Once the colloidal dispersion is loaded into the experiment cell, the electric field is applied (see fig. 2.10–A and fig. 3.9–A). Electrophoresis supplies particles to the meniscus region. They come closer to the contact line and start to accumulate (see fig. 2.10–B,C and fig. 3.9–B,C). AC electrowetting [51] generates a flow [52, 53] near the contact line (due to the increase and decrease in the contact angle). The flow becomes unstable and lead to a transverse modulation. This might be responsible for the cluster formation. Under these conditions, cluster formation initiates (see fig. 2.10–D and fig. 3.9–D) and later clusters grow (see fig. 2.10–E,F and fig. 3.9–E, F, G), until they stabilize their size. Finally, the clusters will start to age/dissociate (see fig. 2.10–G). In fig. 3.9–H, the clusters deform their shape and the aging may start earlier (see fig. 3.9–F and G, a cluster in the right extreme of the frame). The observed effects and the mechanism of cluster

formation are sketched in fig. 3.14.
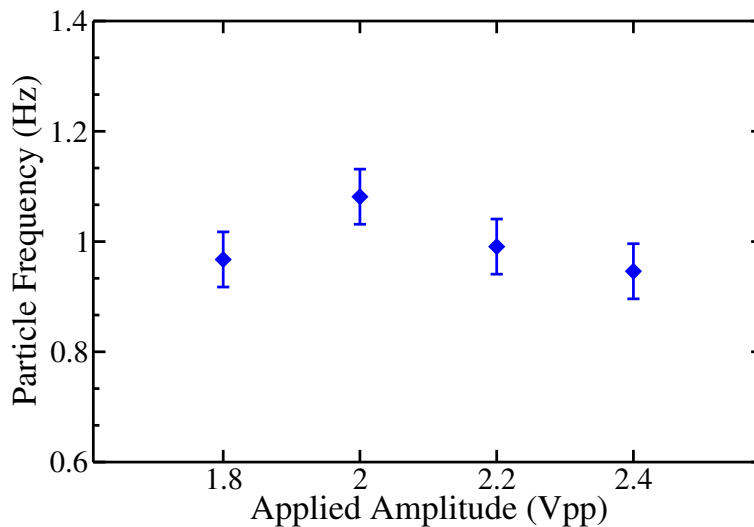
3.3.2.1.   Behavior of particles

Figure 3.10: Measured frequency of particles as a function of increasing applied amplitude at constant applied frequency of 1 Hz.

To obtain an initial picture about the system, response of particles to the applied field is measured. This response is measured with two different cases of applied conditions. One is by keeping the frequency constant (1 Hz) and varying the amplitude (fig. 3.10) and the other is by keeping the amplitude constant (1.8 Vpp) and varying the frequency (fig. 3.11). For the range of applied amplitudes (see fig. 3.10), from 1.8 Vpp to 2.4 Vpp, at a constant frequency of 1 Hz, the measured frequencies of the particles coincide with the applied one (1.00±0.1 Hz). Hence, in our experimental conditions, the particles follow adiabatically the applied electric field. This can also be seen in fig. 3.11 for applied low frequencies (from 0.4 Hz to 1.6 Hz). At applied higher frequencies (from 2 Hz to 4 Hz), the measured values for particles seem to be different. Possibly, at higher values, fast variation of the contact angle makes the particles unable to follow the force.

3.3.2.2.   Behavior of clusters

In the case of clusters (fig. 3.12), for applied low frequencies from 0.6 Hz to 1.8 Hz (see fig. 2.10), we measure the frequency response of clusters. The clusters follow the forcing condition. The measured frequency of clusters is close to the applied frequency. Similarly as in the case of the response of particles (fig. 3.10 and fig. 3.11–0.4 Hz to 1.6 Hz), the clusters follow the force at applied low frequencies (fig. 3.12 from 0.6 Hz to 1.8 Hz). The clusters move as a whole, up and down in these applied low frequencies. Thus, the clusters can follow the variations in the contact angle, and it is observed in the experiments.

But for higher applied frequencies (2 Hz and 3 Hz in fig. 3.12), the response is different. The measured frequencies of the clusters are of higher values (inside the maroon ellipses in fig. 3.12) for applied high frequencies. For these frequencies (2 Hz and 3 Hz), the quick variations in the
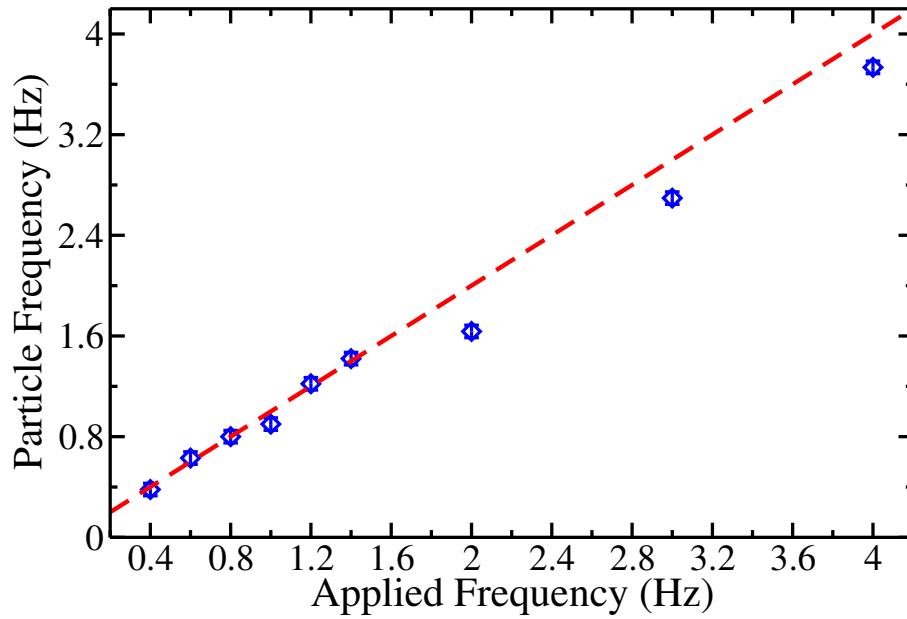
Figure 3.11: Measured frequency of particles as a function of increasing applied frequency at constant applied amplitude of 1.8 Vpp. The dashed line is an indicative to the applied frequencies.
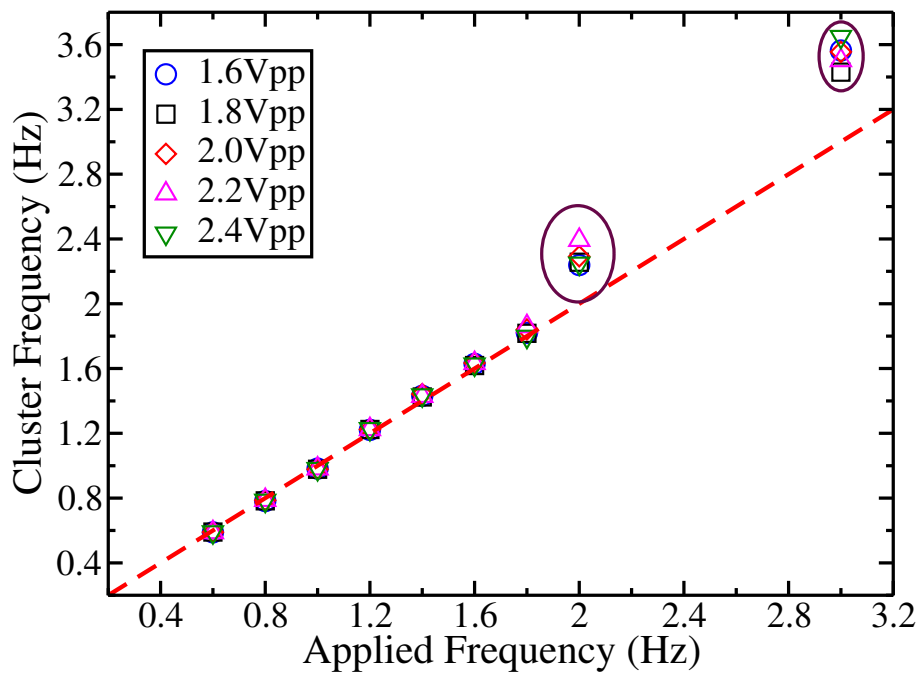

Figure 3.12: Frequency response of the clusters to the applied field. The dashed line is an indicative to the applied frequencies. The measured frequencies of the clusters are of higher values (inside the maroon ellipses) for applied frequencies 2 Hz and 3 Hz.

contact angle make these clusters to be unable to follow. A similar behavior is obtained for the particles also (see fig. 3.11–2 Hz to 4 Hz). Due to the inertia of clusters, they do not move. However, the particles rearrange inside the clusters. This rearrangement varies the intensity of the light (central region of individual cluster, D to H in fig. 3.9). The intensity is varying at higher frequencies which are slightly greater than the applied one. In this conditions, the clusters are not moving as a whole up and down.

3.3.2.3. Evolution of clusters
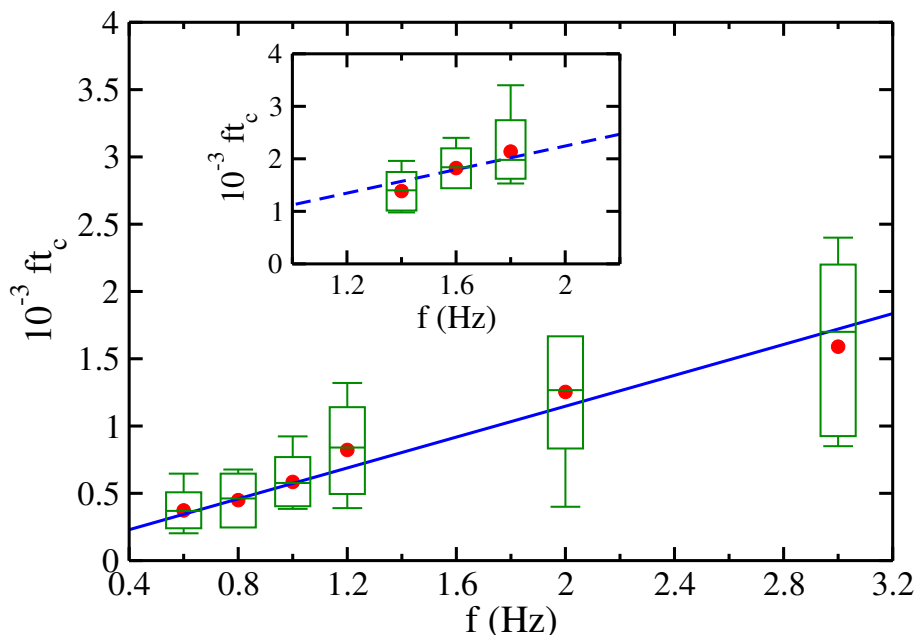
Figure 3.13: Non dimensional threshold time (ft$_c$) as a function of applied frequencies. Box-plots include data from different strengths of the applied field. For each frequency, the mean non dimensional threshold time is represented by a filled red circle. The lines are fits to a proportional law (solid corresponds to t$_c$ = 574 s and dashed to t$_c$ = 1122 s). Inset corresponds to experiments performed with more hydrophilic substrates.

To correlate the formation of clusters with the applied field, the temporal length scale at which they form is measured. The measurement helps to characterize the long temporal scale behavior of the system. The threshold time (t$_c$), at which the clusters form completely, is defined as the time beyond which the clusters start to dissociate. The non dimensional threshold time (ft$_c$) as a function of applied frequencies (f) is shown in figure 3.13. ft$_c$ increases proportionally to the increasing applied frequencies. This proportional increase (fig. 3.13) indicates that this global evolution of the system (time required for the clusters to dissociate) is weakly dependent on the forcing condition.

3.3.2.4. Surface property of the substrates

The cluster evolution may depend on the surface properties of the substrate. As the applied field varies the contact angle through AC electrowetting and hence the mean contact angle of the

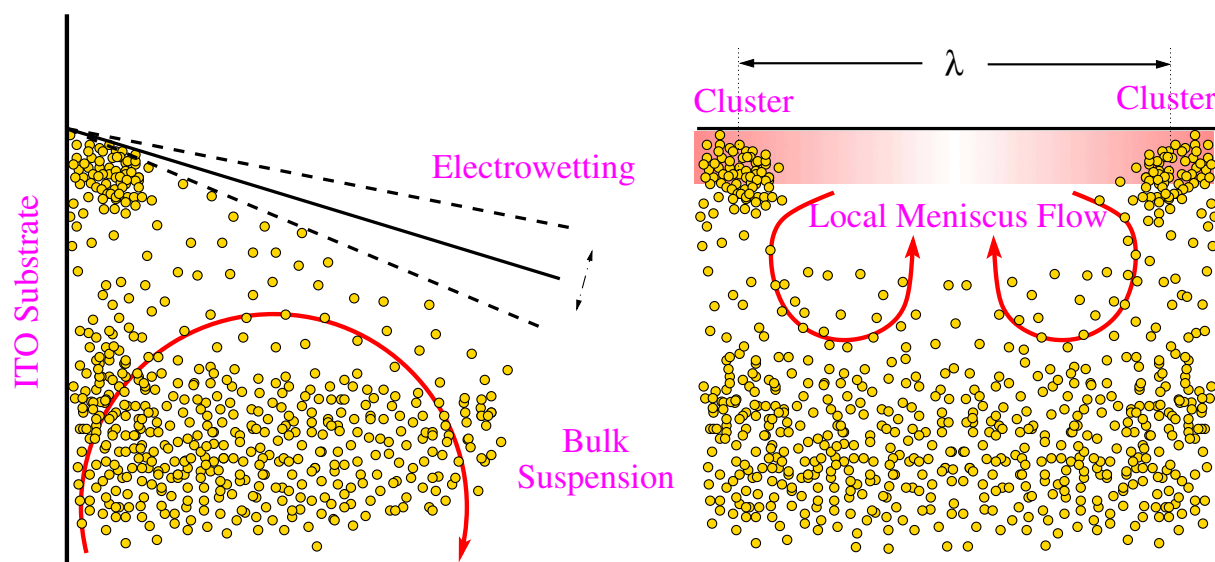Figure 3.14: Microscopic sketch of the region near the contact line. Left: Lateral view. Effect due to electrowetting has been enhanced for better view. Right: Front view. Local flows are indicated by red arrows and the corresponding transverse modulation in the contact angle is shown by the color (shade) gradient near the contact line.

substrate can be of high importance. To show this, preliminary experiments are performed using the substrates of more hydrophilic character. We also measure the non dimensional time and it is shown in fig. 3.13 (inset). Due to the character of the substrate (more hydrophilic), mean contact angle is low and consequently AC electrowetting effects are relatively minimal compared to other experiments. This increases the time to get the required amount of particles near the contact line region. Another possibility to have populated contact line region with particles is to increase the initial concentration. In our preliminary experiments, high initial concentration (0.7%) is used. But defining the clusters is difficult since it forms a thick band of particles. When high concentration is used, a decrease of the forcing condition would reduce the effects of electrophoresis and consequently, the clusters could be defined.

3.3.2.5. Characteristic length

The clusters are spatially distributed and they are separated by a characteristic length (see fig. 2.10–F and fig. 3.9–G). AC electrowetting might induce an instability on the flows. The instability gives rise to transverse local flows and to a modulation of the varying contact angle (fig. 3.14–right). This local flows are advection-like closed flows. The recurrence time is termed as the time taken by a volume element to complete a cycle. The characteristic length of this closed flows corresponds to the mean spatial distance between the clusters ($\bar{\lambda}$). Also, the characteristic length (fig. 3.15) is measured at threshold time t_c.

From the plot (fig. 3.15), it is clear that the characteristic length varies as a function of applied frequency. In a given amplitude, for e.g. 2.4 Vpp in fig. 3.15, the mean characteristic length increases to a maximum and then decreases as the applied frequency is increased. In each amplitude, for one particular frequency, for e.g. at 1.0 Hz (for 2.4 Vpp), a relative maximum
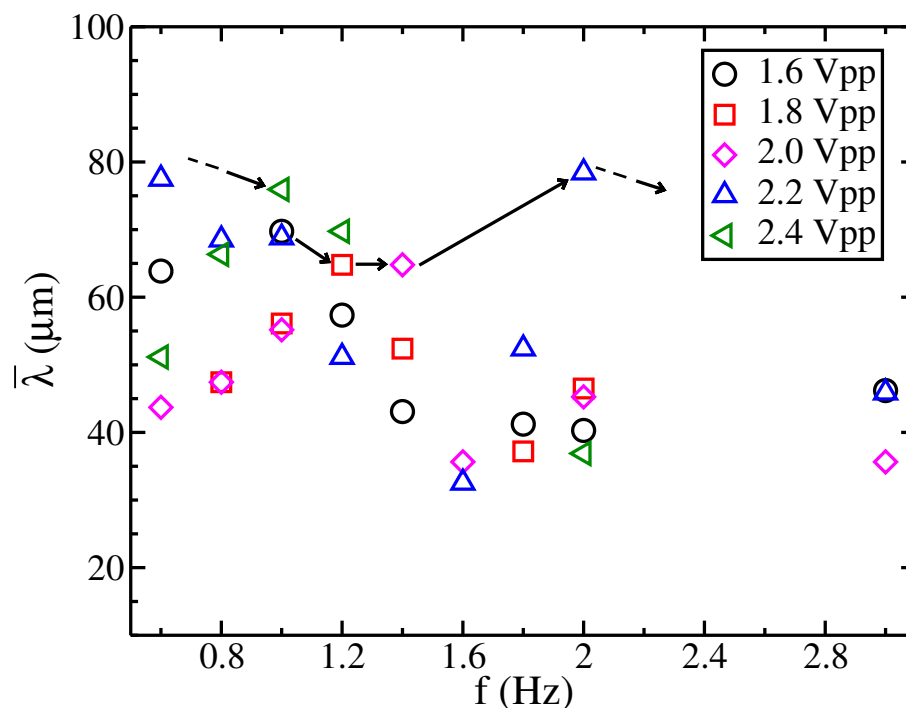
Figure 3.15: Mean characteristic length ($\bar{\lambda}$) at the threshold time (t_c) as a function of applied frequencies. The arrows outline the sequence of the maxima occurring while increasing the strength of the field. The dashed line arrows correspond to the 2.2 Vpp to 2.4 Vpp transition.

in characteristic length is observed. This frequency (e.g. 1.0 Hz for 2.4 Vpp) depends on the recurrence time, and thus on the strength of the local flows near the contact line region. To attain this relative maximum condition for increasing applied frequencies, one has to increase the applied amplitude as shown in the fig. 3.16.

The recurrence time is limited to have a regular flow and consequently, for high applied amplitude (e.g. 2.4 Vpp) the relative maximum in characteristic length is obtained at low applied frequency, which corresponds to a multiple of the expected recurrence time (see dashed line arrows in figure 3.15).
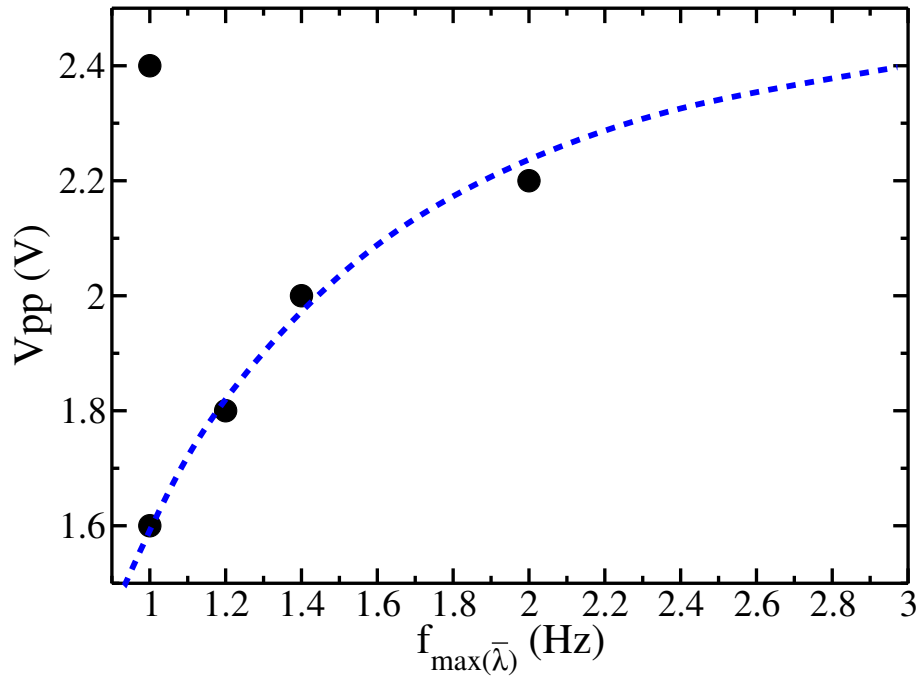
Figure 3.16: Correlation between the applied amplitude and the formation of clusters for a relative maximum in characteristic length $\bar{\lambda}$. Dashed line is a guide to the eye. For applied amplitude of 2.4 Vpp, the relative maximum in characteristic length is obtained at low applied frequency (1 Hz). This corresponds to a multiple of the expected recurrence time (see dashed line arrows in figure 3.15).

Chapter 4

Materials and methods for spin-coating experiments

4.1. Outline

Spin-coating experiments are performed with external electric and magnetic fields, respectively. The spin-coater is modified accordingly to apply external fields. This chapter also explains the experimental techniques and methods that characterize the spin-coating experiments.

4.2. Experiments with magnetic field

4.2.1. Spin-coater
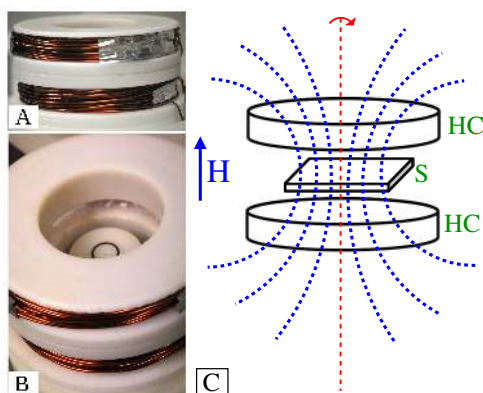
Figure 4.1: A and B–Photographs of the experimental components: (A) A pair of Helmholtz coils and (B) Same mounted on the spin-coater. C–Sketch of the experimental setup and the magnetic field lines (HC: Helmholtz coil; S: Substrate). The substrate spins in the region of uniform magnetic field.

All the experiments are performed with a commercial spin-coater (Laurell technologies, WS-650SZ-6NPP/LITE/OND). Rotation rates can be varied from 2000 to 7000 rpm. Sketch of the experimental setup is shown in fig. 4.1–C. Photographs of the complete setup are shown in

fig. 4.1–A and B. Magnetic fields ranging from 0 to 0.066 T are applied by a pair of Helmholtz coils (fig. 4.1–A). The coils are placed in such a way that the substrate spins in the region of uniform axial magnetic field (fig. 4.1–B and C). The applied magnetic fields are varied by adjusting the current given to these coils with an external power supply.

4.2.2. Substrates

Glass substrates of size $38 \times 25 \times 1$ mm^3 are used for all the experiments. The substrates are cleaned with acetone in an ultrasonic bath for fifteen minutes followed by a soft basic piranha etch (ultra-pure water/ammonia/hydrogen peroxide in the ratio of 5:3:1) at 67°C for forty minutes. The substrates are rinsed with ultra-pure water after each cleaning/etch stage. The wet cleaned substrates are then dried by nitrogen gas blow. Freshly cleaned and dried substrates are used for each experiment.

4.2.3. Colloidal dispersion PS–MAG

The aqueous superparamagnetic colloidal dispersion (the superparamagnetic particles are polystyrene coated magnetite; density $= 1.2085$ g/cm^3) is obtained from Polysciences, Inc. at a concentration of 2.1% (v/v). The particles are polydisperse with diameters ranging from 1 to 2 μm. As provided dispersion is then ultrasonicated for fifteen minutes before starting the experiments.

Characterization of superparamagnetic particles PS–MAG

Magnetic characterization of superparamagnetic colloidal particles (PS–MAG) is obtained from the group of Dr. C. Gómez-Polo. The particles are characterized with SQUID magnetometer (Lot-Oriel n. MPMS-XL). In fig. 4.2, the magnetization curve is shown, with a small coercive field strength ($H_c = 23$ Oe; see fig. 4.2–inset). The mass magnetization at a moderate field (1.2 kOe) is about 40 emu/g. This indicates that the particles are superparamagnetic.

4.2.4. Colloidal dispersion SiO$_2$–MAG

The superparamagnetic particles are silica coated magnetite of diameter 1.51 ± 0.05 μm (density $= 1.6$–1.8 g/cm^3). They are obtained in dried form from microParticles GmbH, Germany. The particles are thermally treated to remove the moisture absorbed by them. They are weighed before and after the thermal treatment. Then, the particles are homogeneously dispersed in ultra-pure water to obtain a concentration of 1.44% (v/v). The dispersion is ultrasonicated for fifteen minutes before starting the experiments.

Characterization of superparamagnetic particles SiO$_2$–MAG

Magnetic characterization of superparamagnetic colloidal particles (Si–MAG) is obtained from the group of Dr. C. Gómez-Polo. The particles are characterized with SQUID magnetometer (Lot-Oriel n. MPMS-XL). The magnetization curve is shown in fig. 4.3, with a small coercive field strength ($H_c < 20$ Oe). The mass magnetization at a moderate field (1.2 kOe) is about 9.8 emu/g.
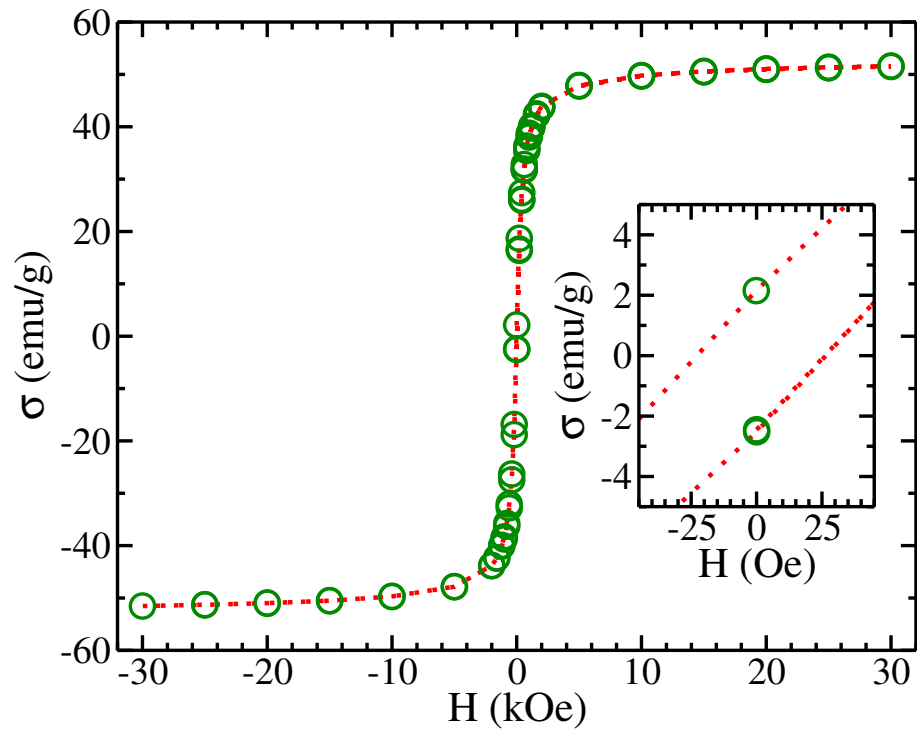
Figure 4.2: Magnetization curve for the superparamagnetic particles (PS–MAG) at 300 K. Inset shows a magnified portion of the graph to obtain the coercive field strength. The plot is obtained from the group of Dr. C. Gómez-Polo.
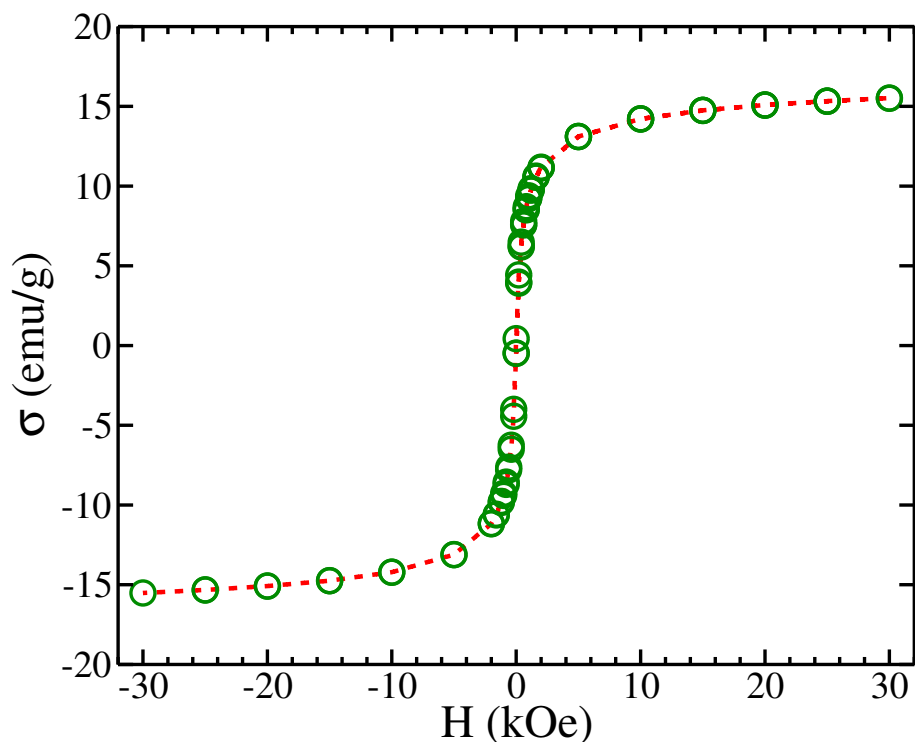
Figure 4.3: Magnetization curve for the superparamagnetic colloidal particles (SiO$_2$–MAG). Dotted line interpolates data points from the measurement. The plot is obtained from the group of Dr. C. Gómez-Polo.
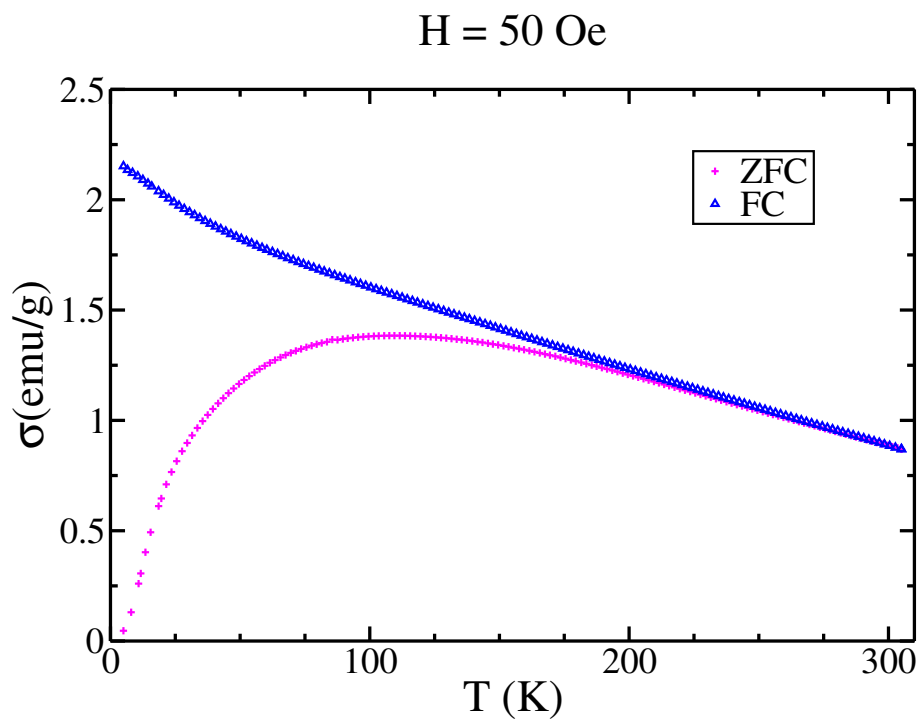
Figure 4.4: Induced FC-ZFC curves at 50 Oe. Blocking temperature is around 108 K. The plot is obtained from the group of Dr. C. Gómez-Polo.

Field cooled–Zero field cooled plot measured at a magnetic field of 50 Oe is shown in fig. 4.4. Blocking temperature is around 108 K. This indicates that the particles are superparamagnetic.

4.2.5.   Experiment

The spin-coater is operated at a required rotation rate and the magnetic field is applied. Then, 120 μl of the superparamagnetic colloidal dispersion is pipetted onto the spinning substrate. Once the spun dispersion is dried (within fractions of a second), magnetic field is turned off and the spinning is stopped. Micrographs are taken on the spin-coated substrates at 2 mm increasing intervals from the center of spinning.

Measurements

Figure 4.5: (left) Micrograph of the dried substrate (for PS–MAG dispersion) at 4 mm from the center of rotation in the absence 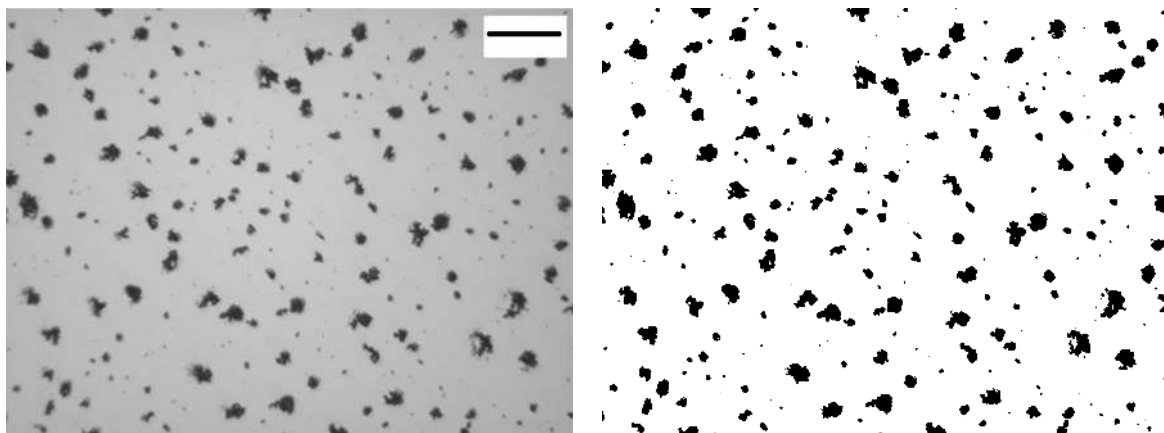of the applied magnetic field. The spinning rate is 2000 rpm and the scale bar is 50 μm. (right) Binary image after doing a threshold to the micrograph in left.

The micrographs are thresholded and segmented using gimp. A binary image is shown in fig. 4.5–right and the respective micrograph is given in the left side of fig. 4.5. The binary images from all the experiments are then analyzed using homemade routines in Octave. In our case, we use dilute dispersions. As a consequence, the obtained morphologies are submonolayers of superparamagnetic particles (clusters). In our analysis, we are not considering the submonolayers that overlap with the boundary of a given image. From the binary image, we measure the area occupied by the superparamagnetic particles relative to total area of the region. This is called occupation factor ε^2, or surface coverage. It is equivalent to the dimensionless thickness of a multilayer deposit. We calculate the occupation factor for each image and the spatially averaged values are used for further analysis. Other kind of measurements such as area occupied by the clusters of superparamagnetic particles and number density of clusters (number of clusters of superparamagnetic particles relative to the total area of the region) can be performed from the binary image shown in fig. 4.5–right. To characterize the geometry and the orientation of the clusters of superparamagnetic particles, the eccentricity of a cluster is measured by means of the second order central moment. Finally, we analyze the number of nearest neighbors of each cluster. We find the centroid positions for each cluster of superparamagnetic particles and

the corresponding Voronoi diagram [112] is calculated. From this, the mean number of nearest neighbors is obtained.

4.3.   Experiments with electric field

The experiments were performed at the Department of Physics and Physical Oceanography, Memorial University of Newfoundland, Canada with Dr. A. Yethiraj.

4.3.1.   Spin-coater
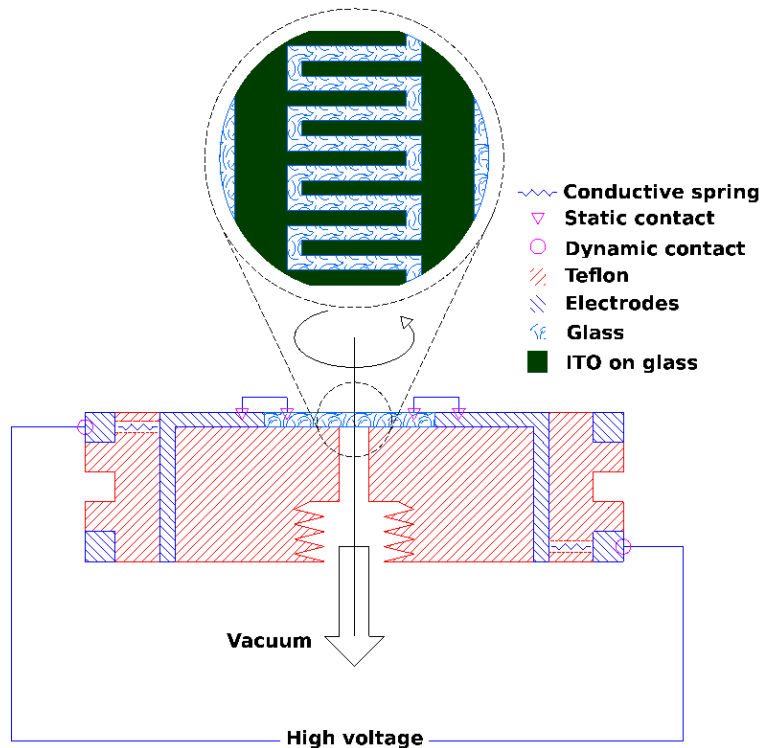
Figure 4.6: Schematic drawing of the modified spin-coating chuck to apply the electric fields. The bottom half of the sketch shows the side view of the chuck. The top half of the diagram presents the top view of the patterned Indium Tin Oxide (ITO) substrate, which has two sets of mutually interdigitating electrodes shown in dark green color. Electrical contact is made between the two exterior rings on the chuck and the two interdigitating electrodes on the patterned ITO substrate such that one of the electrodes is connected to high voltage and the other one is grounded.

All the experiments are performed in a commercial spin-coater (Laurell technologies, WS-400-6NPP). Rotation rates can be varied from 2000 to 7000 rpm. To apply an electric field whose orientation in the $x - y$ plane rotates with the sample (static in the rotating frame), a custom chuck is constructed (fig. 4.7). Fig. 4.6 shows schematically a cropped side view of the modified spin-coating chuck used in the experiments. The essential elements in this chuck are two wire brushes, as shown in the figure by open red circles, that serve as dynamic electric contacts. These brushes (one of them can been seen in fig. 4.7) are connected to the active and ground terminals,

Figure 4.7: Photograph of the modified spin-coating chuck.

respectively, of a high voltage amplifier and they make continuous electrical contact with two rotating electrodes on the modified chuck (shown in diagonal blue hatch, fig. 4.6). The amplifier is fed by a sinusoidal signal from a function generator. The dynamical contacts on the chuck are realized through two exterior rings. This chuck has two conducting electrodes (top plates) on either side of the spinning center that holds the patterned Indium Tin Oxide (ITO) substrate. Electrical contacts between the two exterior rings and two top plates of the chuck are shown in diagonal blue hatch (fig. 4.6). These top plates can been seen in fig. 4.7 and make static electrical contact (red inverted triangles in fig. 4.6) with the two interdigitated ITO electrodes. Each top plate is connected to one end of a patterned ITO coated glass substrate (in the next sub-section, procedure for substrate patterning is provided). Thus, the conducting patterned ITO substrate makes direct electrical contact with the dispersion. One end of the patterned ITO is thus connected to an alternating high voltage amplifier while the other end is grounded.

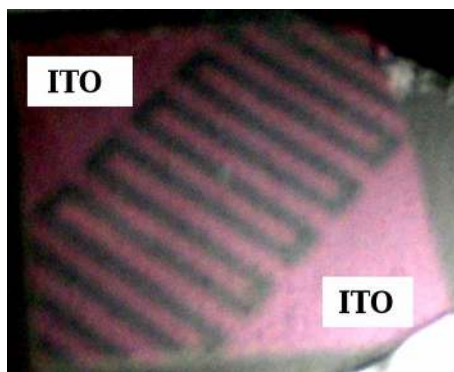### 4.3.2. Substrates and patterning procedure

Figure 4.8: Photograph of the patterned ITO substrate of size 20×20 mm^2. Electrode spacing is 1.05 mm.

Commercially available microscope glass slides are used as base substrates. ITO coated mi-

croscope cover slips of size 20×20 mm^2 and of sheet resistance 30–60 Ω/sq. are glued (UV curing glue, Norland Optical Adhesive 61) over those base substrates. A layer of Shipley S-1813 photoresist is spin-coated onto the ITO glued substrates at 4000 rpm for thirty seconds. Then the ITO substrate is soft baked at 100°C for one minute. The ITO substrate with photoresist is then covered with a metal mask where the desired pattern is engraved. They are exposed to an ultraviolet light for seven seconds. The unmasked region becomes acidic due to the UV exposure. To develop, the exposed substrate is immersed in a 0.5% (w/v) NaOH solution for fifteen seconds and then rinsed with distilled water. Hence, the unmasked region is bare ITO, and it is etched chemically by immersing in HCl (11.65 M) for thirty seconds and then rinsed with distilled water. The etched substrate is cleaned with acetone to remove the unexposed photoresist. Photograph of the patterned ITO substrate is shown in fig 4.8. Spacing between the interdigitating electrodes is 1.05 mm. Wires are glued (UV curing glue, Norland Optical Sealant 91) to the two ends of the interdigitated ITO pattern. Electrical contact between the ITO and the wire lead is made using the silver paste. Other end of the wire lead is connected to the modified spin-coating chuck.
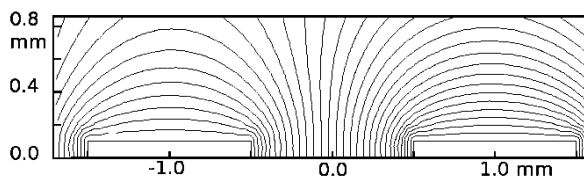
4.3.3. Simulated electric potential

Figure 4.9: Equipotential lines in the interdigitated electrode geometry. The non uniformity in the electric field can be visualized via the spatially varying density of equipotential lines. The map was done by A. P. Bartlett from the group of Dr. A. Yethiraj.

A map of the simulated electric potential done by A. P. Bartlett from the group of Dr. A. Yethiraj (shown in fig. 4.9). Spatial non-uniformity in the equipotential lines in a schematic simulated electrostatic profile for the field geometry near two digits in the interdigitated electrode geometry is presented. The simulation is carried out for a potential difference of 1000 V between the electrodes. The potential difference between adjacent equipotential lines is 32.25 V. Both the strength and the non uniformity of the electric field is higher around the electrode edges (where the equipotential lines are closely spaced). It is uniform above the surface of electrode as well as in the space (center) between the two electrodes.

4.3.4. Colloidal dispersion

Spherical silica particles of diameter 458 ± 2 nm are obtained in dried form from Angstrom-Sphere, that is commercially available in Fiber Optic Center inc. The particles are dried to remove the moisture. They are weighed to calculate the amount of solvent to be added to obtain a concentration of 20% v/v or $\sim$ 40% w/w. Methyl Propyl Ketone (MPK) is used as a solvent. Preliminary spin-coating experiments were performed by suspending the particles in Methyl Ethyl Ketone (MEK). Evaporating time for both dispersions as a function of spinning rate is measured. They are shown in fig. 4.10. Dispersion with MPK as solvent is used for experiments with electric
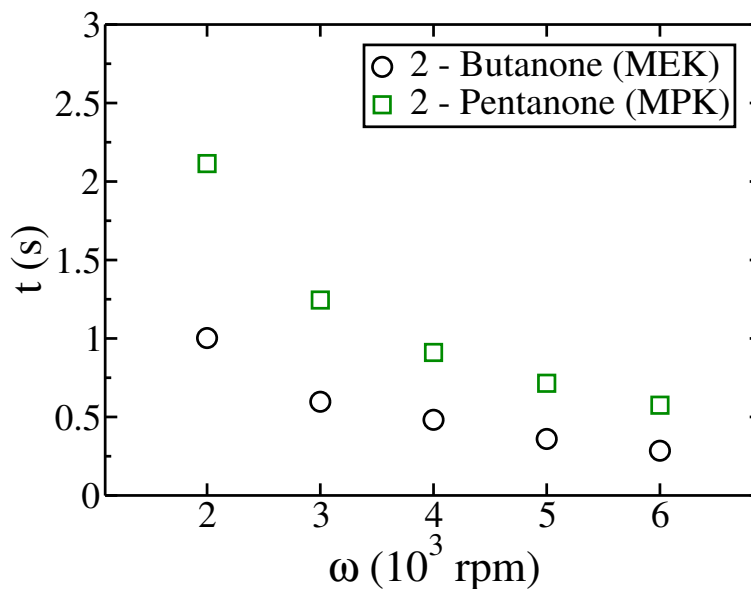
Figure 4.10: Drying time for dispersions with different kinds of solvent. The particles are spherical silica.

fields because, it dries at slower rate compared to MEK. Longer drying time of the dispersion makes the interactions due to the electric field to last for more time. Consequently, it may provide enhanced results.

4.3.5.   Experiment

Before starting the experiments, the field is turned on and adjusted to desired values. Contacts are checked to avoid electrical malfunction. Once the field is set, the substrate is spun at 2000 rpm. When the substrate reaches a constant angular velocity, 40 μl of the colloidal dispersion is pipetted onto it. After the spun dispersion is completely dried, the spinning is stopped and the field is turned off.

Characterization

The spin-coated substrates are characterized by Scanning Electron Microscopy (SEM) at different magnifications. A sample image is shown in fig. 4.11. A small portion is magnified for better view. For particle detection analysis, images with same magnification are always used. Homemade routines [113] are obtained from the group of Dr. A. Yethiraj. The routines are used to obtain the particle centers. Particle tracking analysis are optimized for large number of particle features in the SEM image. From the information of particles, orientation of the microscopic domains of colloidal particles in the SEM image is calculated. The routine returns the angle value at which most of the domains are oriented. That is referred as the dominant orientation of the domains (θ). Details concerning the particle detection methods, packing fraction, and domain orientation calculations are explained in [113].
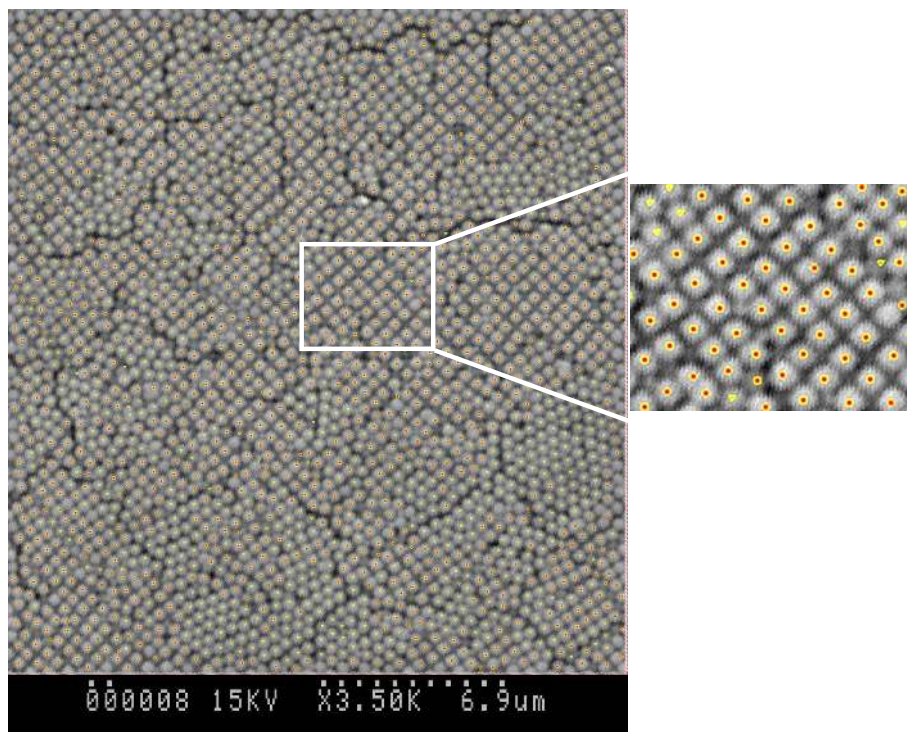
Figure 4.11: Particle detection analysis for a SEM image obtained in the experiment (absence of the electric field). Magnified portion shows the identified particle centers. Routines are obtained from the group of Dr. A. Yethiraj [113].

Chapter 5

Results and discussion: Spin-coating experiments

5.1.   Outline

In this chapter, effects of external fields on the spin-coating of colloids are presented. Magnetic field is applied during the spin-coating of dilute superparamagnetic colloids. Relevant studies on the obtained morphologies are discussed in the following section. A spin-coating model which takes into account the particulate nature of the spin-coated deposits is proposed . Experiments are correlated using this model. In the last section, we show that an application of a nonuniform electric field during the spin-coating process (using nonmagnetic colloids) breaks the axial symmetry and also gains local control over the orientation of the microscopic crystallites.

5.2.   Spin-coating of superparamagnetic colloids in magnetic field

Spin-coating of simple fluids is well known and spin-coating of polymers is commercially established. There are models [69, 70] based on the lubrication approximation which predict fairly well the experimental results [71]. Studies on the spin-coating of colloids (both numerical simulations and experiments) [114] focused on the effect of angular velocity, initial concentration, properties of the solvent etc., to the final thickness of the coating. Lately, spin-coating experiments with highly volatile colloidal dispersion [90] obtained non-planar coatings. Symmetry transitions which result from shear melting and shear crystallization mechanisms are reported [91, 115]. However, fundamental interactions in the colloidal systems while spin-coating are important to study as they are related directly to the final film thickness. Final morphology of particles mainly depend on the initial concentration of the dispersion, spinning rate and solvent properties. Sharp transition in the final morphology by varying the spinning rate is easy to evaluate. But, obtaining the desired morphology(ies) is difficult if it is done only by changing the spinning rate.

From many ways, tuning the properties of dispersion while spinning may offer structures of interest that could find potential application. To start with, spin-coating experiments with dilute superparamagnetic colloids in the presence of magnetic field are performed. Previous spin-coating experiments reported by Giuliani *et al.* [90] and Arcos *et al.* [89] were done using colloidal dispersions (non magnetic particles) of moderate or high initial concentration (10% to

20 % v/v), which made difficult the characterization of the morphology formation. In the case of dilute dispersions of superparamagnetic particles, we obtain sparse morphologies that consist of clusters of particles. The clustering processes might be closely related to the final deposit and its order. Application of external magnetic field while spin-coating affects the fluid by changing its viscosity (see subsequent sections). The external field could influence the aggregation dynamics of superparamagnetic particles through magnetic dipole interactions. Exploring the formation of submonolayers and clusters of particles might help us in understanding the formation of compact structures like monolayers and multilayers (also, the transition from submonolayer to compact structures).

5.2.1. Morphologies

In our experimental conditions, the obtained deposits of colloidal particles are submonolayer, mainly formed by clusters of superparamagnetic particles. In some regions over the substrate, islands or groups of particles are seen. The density of particles per unit area decreases if we move away from the center of rotation on the dried substrate and / or the rotation rate is increased and / or the applied magnetic field is decreased.

Figure 5.1: Micrographs of the dried substrate (for PS–MAG dispersion) at 4 mm from the center of rotation. The applied fields are 0 T (left) and 0.033 T (right). In both cases, the spinning rates are 2000 rpm and the scale bars are 0.1 mm.

Representative micrographs of the dried substrate for the PS–MAG dispersion are shown in fig. 5.1 and fig. 5.2 (the difference is the magnification). The experiments are performed at 2000 rpm and the applied field is of 0 T (fig. 5.1–left) and 0.033 T (fig. 5.1–right). Islands or groups of particles are seen mostly in the experiments of zero field condition (high magnification micrograph, fig. 5.2–left). In the case of applying magnetic field while spinning, formation of clusters of bigger size (fig. 5.1–right and high magnification micrograph, fig. 5.2–right) could be due to the presence of polydisperse superparamagnetic particles in the dispersion.

5.2.1.1. Area and number density

Micrographs are obtained at increasing regular intervals from the center of rotation. For each micrograph, the average area of the clusters $\langle A \rangle$ (the area of projection on the dried substrate) is
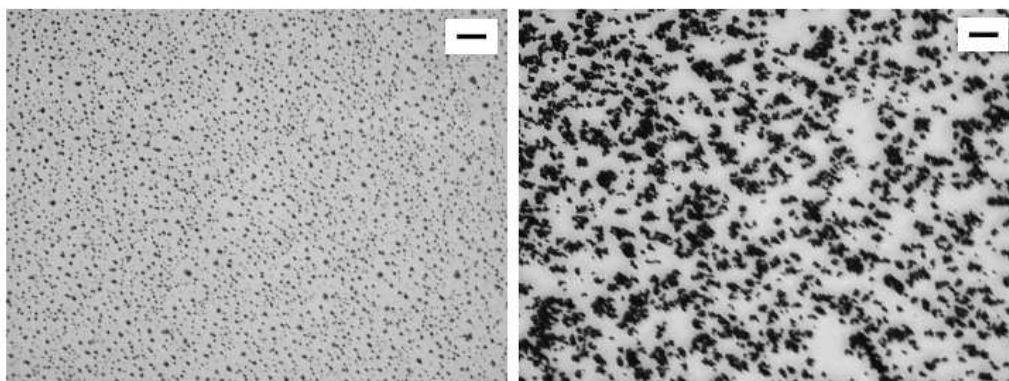
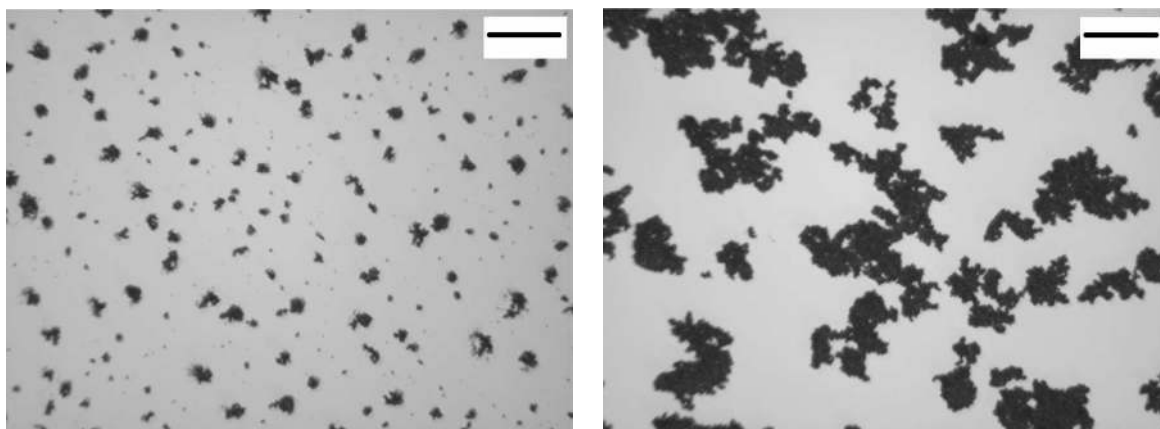Figure 5.2: High magnification micrographs of the dried substrate (for PS–MAG dispersion) at 4 mm from the center of rotation. The applied fields are 0 T (left) and 0.033 T (right). In both cases, the spinning rate is 2000 rpm and the scale bars are 50 μm.
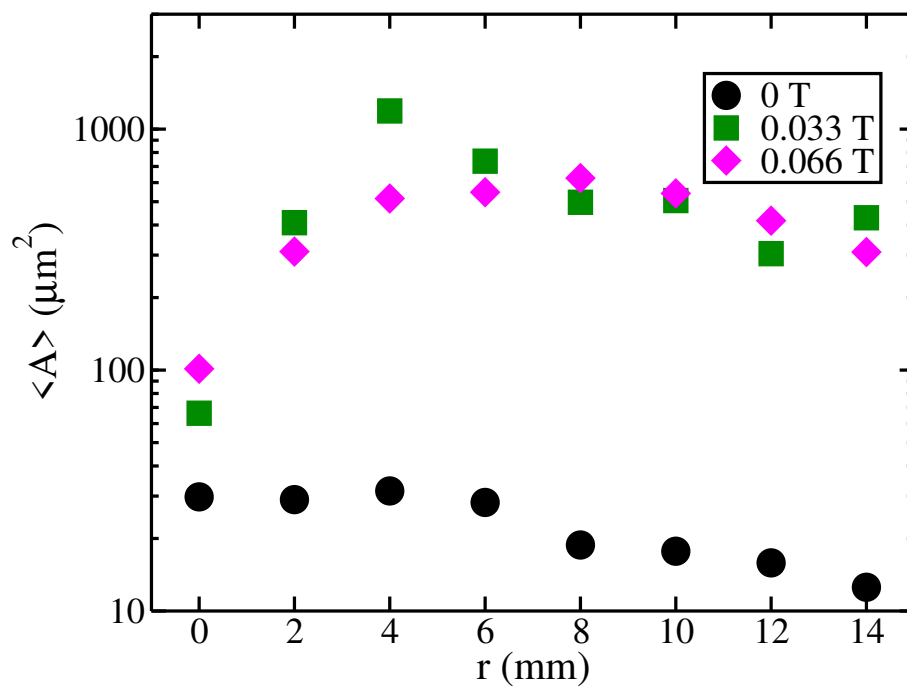

Figure 5.3: Average area of clusters as a function of radial distance from the center of rotation at 2000 rpm (colloidal dispersion PS–MAG).
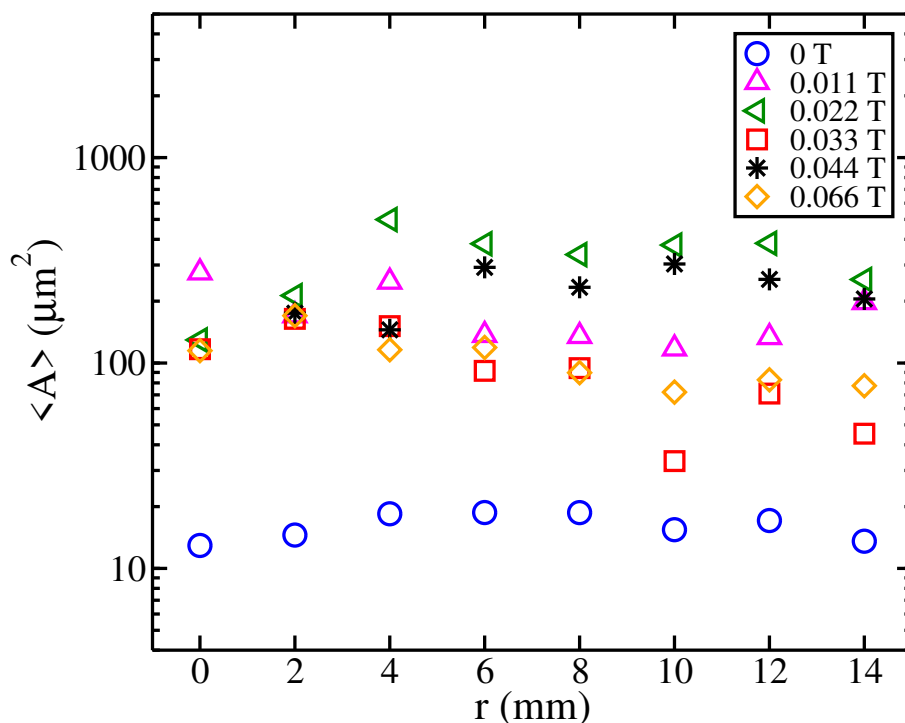
Figure 5.4: Average area of clusters as a function of radial distance from the center of rotation at 6000 rpm (colloidal dispersion PS–MAG).

measured (fig. 5.3 and fig. 5.4). In fig. 5.3 (2000 rpm), the average area of clusters for the applied field condition is higher (squares and diamonds) when compared to the case of zero magnetic field (circles). A similar behavior is observed with the experiments of higher rotation rates (see fig. 5.4) where the average area of clusters is higher when the magnetic field is applied. The applied magnetic field induces the magnetic dipole interactions between the superparamagnetic particles, which form submonolayer deposits (see fig. 5.1–right and fig. 5.2–right). These deposits provide an increase in surface coverage of the substrate and consequently, the average area increases. The results are explained in the following sub-section.

For the same micrographs, the density of clusters (number density) is measured for increasing r (fig. 5.5 and fig. 5.6). The number density decreases for the applied field condition. To explain this behavior, we have to recall the increase in area for the applied magnetic field condition. The increase in area does not represent an increase in the number of clusters of superparamagnetic particles. It shows the formation of submonolayer deposits (see fig. 5.1–right and fig. 5.2–right), hence the number of clusters per unit area decreases. The results are explained in the following sub-section.

5.2.1.2.   Mean area and mean number density

We took the data corresponding to, say, fig. 5.3 and fig. 5.5 and we calculate the spatial average. For all the properties that measured in the experiment (e.g. average area, number density of clusters), the mean and the standard deviation are calculated and plotted.

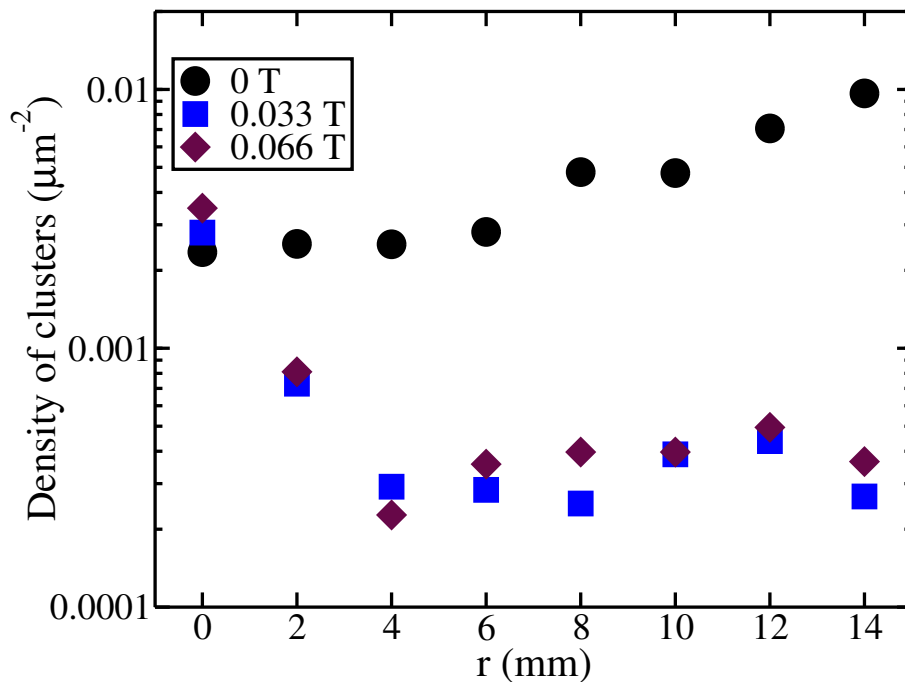The mean values are plotted for increasing applied magnetic field (e.g. for mean area, see

Figure 5.5: Number density of clusters as a function of radial distance from the center of rotation at 2000 rpm (colloidal dispersion PS–MAG).
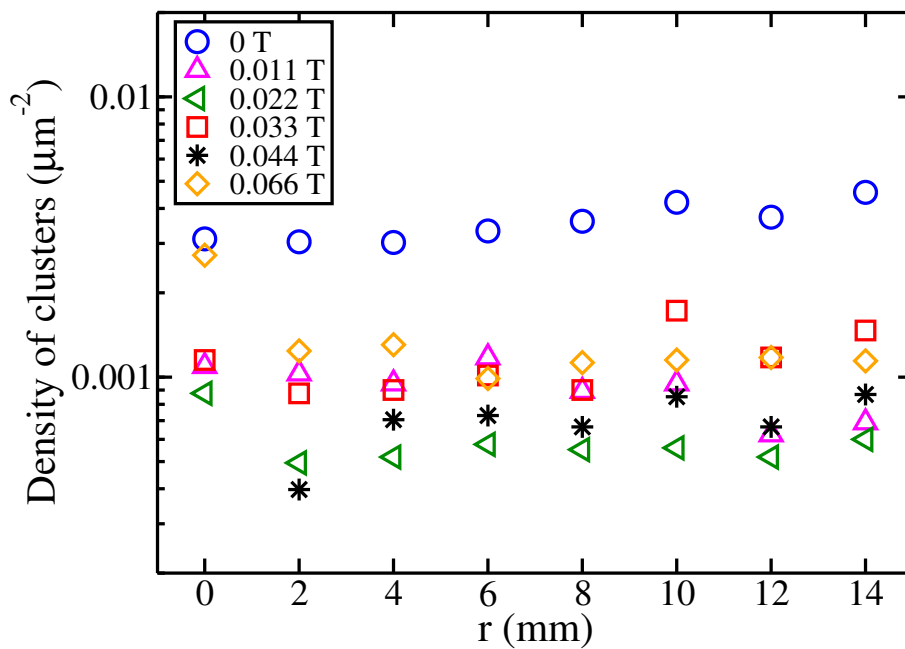

Figure 5.6: Number density of clusters as a function of radial distance from the center of rotation at 6000 rpm (colloidal dispersion PS–MAG).

fig. 5.7). In these plots, the bars represent the standard deviation that corresponds to different r values from the center of rotation. The bars are larger for the applied field condition when is compared to the zero field (taken into account the log scale). This occurs due to a large dependence of $\langle A \rangle$ on r. Altogether, the mean area increases as the applied field is increased. On the contrary, the mean number density of clusters (fig. 5.8) decreases as the applied field increases.
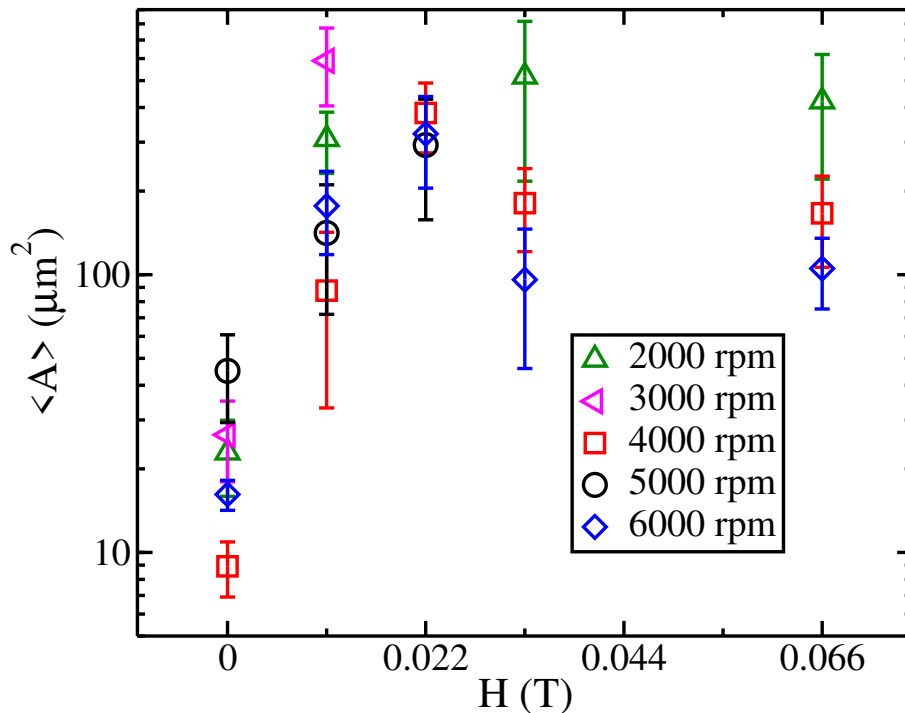
Figure 5.7: Mean area of clusters as a function of increasing external magnetic field (colloidal dispersion PS–MAG).

When the magnetic field is applied while spin-coating, a morphological transition from sparse to submonolayer deposits (consist of clusters of superparamagnetic particles) is commonly observed in the experiments (see fig. 5.1 and fig. 5.2). In a sparse morphology (see fig. 5.1–left and fig. 5.2–left), the number of particles per unit area is very small. The particles are grouped together to form small clusters. In the case of submonolayer deposits, the superparamagnetic particles present more surface coverage over the substrate (see fig. 5.1–right and fig. 5.2–right) and the number of particles per unit area increases.

The applied magnetic field (during spin-coating) influences the transition mainly through the following phenomena. Firstly, it changes the dynamic viscosity of the superparamagnetic colloidal dispersion spinning on the substrate [92]. This has an influence on the rheology of the dispersion. Secondly, the field acts on the particles and it controls the clustering behavior through inter-particle magnetic dipole interactions. The increasing applied field enhances the interaction between the particles, which drives to link the neighboring clusters together to form submonolayer deposits. As the submonolayer deposits provide an increase in surface coverage of the substrate, the mean area increases (see fig. 5.7). Consequently, the number of clusters decreases for the field condition compared to the zero field and a low mean number density is obtained (see fig. 5.8).
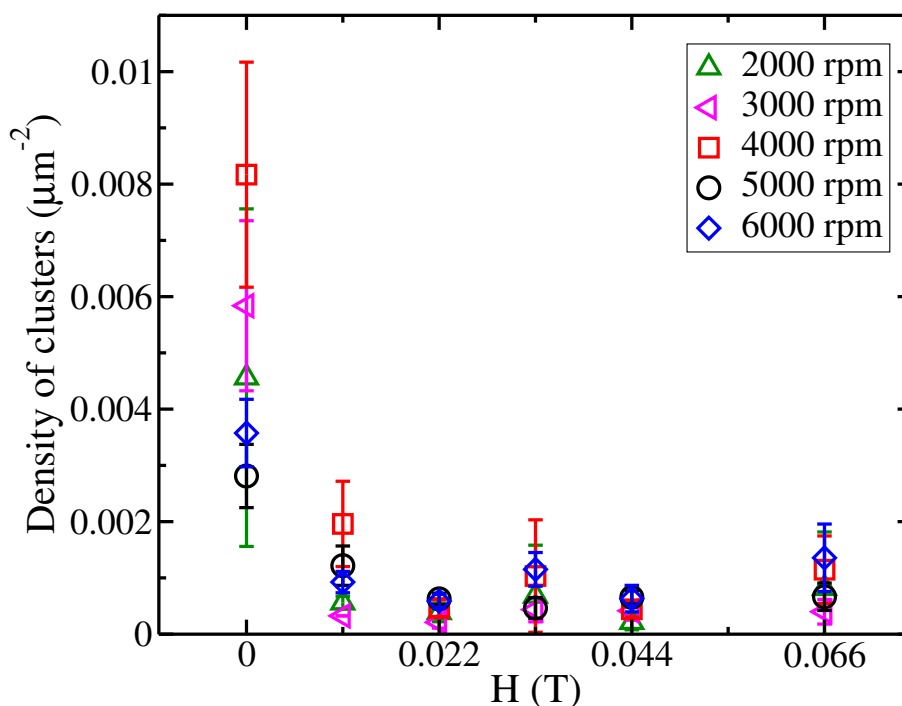
Figure 5.8: Mean number density of clusters as a function of increasing external magnetic field (colloidal dispersion PS–MAG).

In the absence of the field, the colloidal dispersion behaves like non-magnetic. Even though the particles are superparamagnetic, they have very small remanent magnetization. The final morphology of the coating may depend on the rotation rate, initial concentration and solvent properties (in our case, ultra pure water). Polydispersity in the superparamagnetic particles (PS–MAG) has relevant effect (diameter of the particles ranging from 1 to 2 μm). Particle segregation is possible with the polydisperse superparamagnetic particles while spin-coating the dispersion (in the absence of the magnetic field). Hence, the resultant sparse morphology may have clusters of superparamagnetic particles.

5.2.1.3.   Occupation factor

Local occupation factor ε^2 can be defined as the area occupied by the clusters relative to the total area of the region (area of observation). The occupation factor is equivalent to the thickness of a multilayer morphology obtained from spin-coating [116]. For a given experimental condition, the occupation factor depends on the radial displacement from the center of spinning r (non-planarization [90]). Globally, on increasing the applied field, the increase in mean occupation factor (see fig. 5.9) could be understood by means of an increase in the effective viscosity ([92] and references therein), which makes the evaporation of the solvent more relevant during the coating. At higher fields, the occupation factor seems to saturate.

Figure 5.9: Mean occupation factor of clusters as a function of increasing external magnetic field. The mean and standard deviation are obtained by doing a spatial mean to the average occupation factor. The average occupation factor is obtained as a function of increasing radial distance r from the center of rotation (colloidal dispersion PS–MAG).
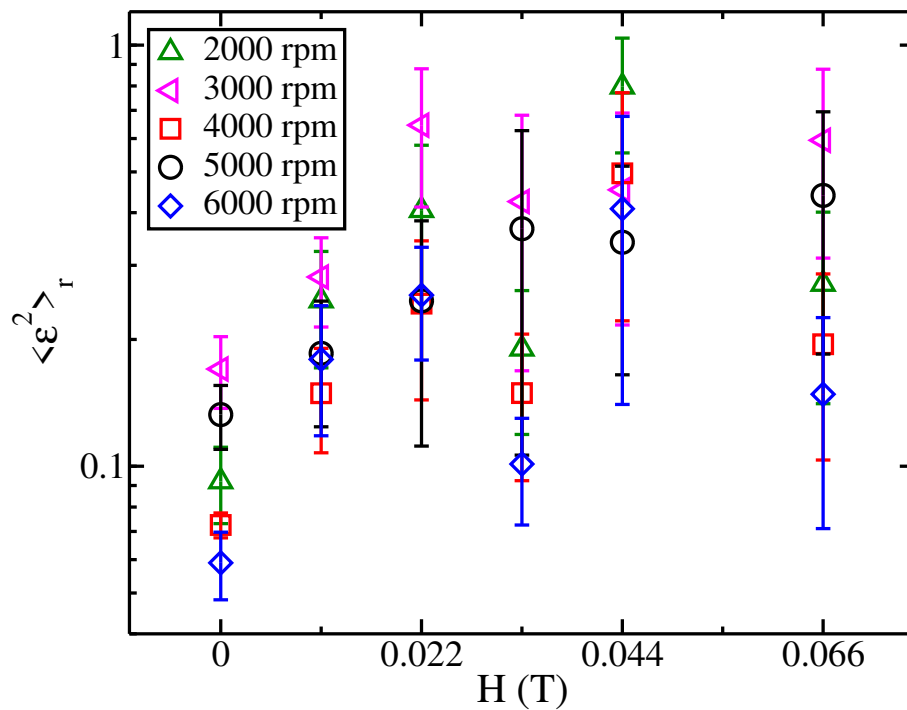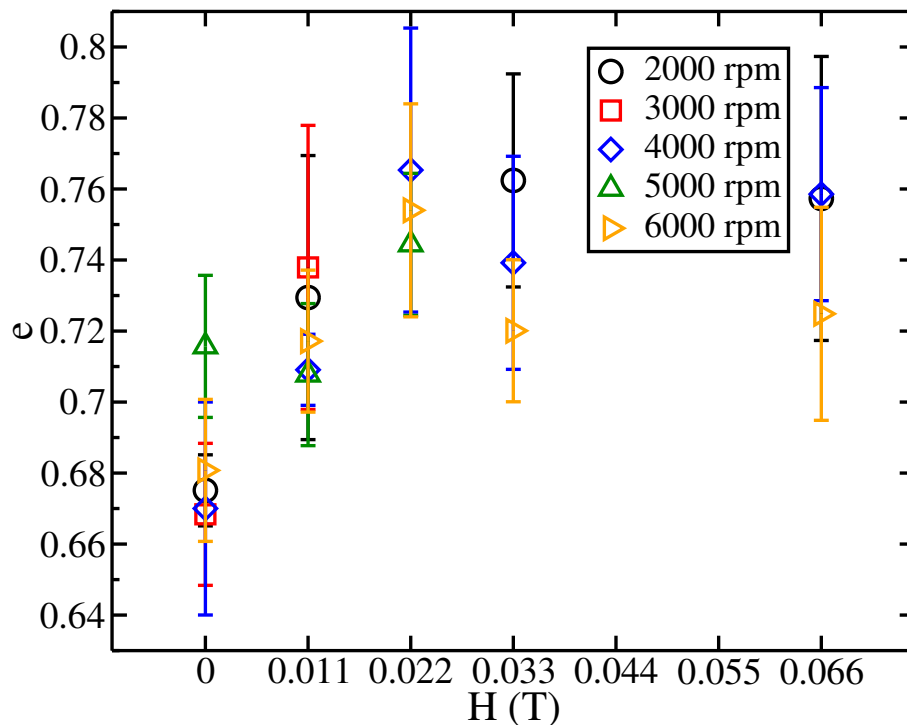
Figure 5.10: Mean eccentricity of clusters as a function of increasing external magnetic field (colloidal dispersion PS–MAG).

5.2.1.4.   Eccentricity of clusters

Spin-coating experiments with non-magnetic colloids of high initial concentration give rise to different axial symmetries, four fold and six-fold (arises from the nature of the microscopic packing of colloidal particles [89]). In this case, the symmetries depend on the properties of colloidal dispersion (size of the particle, volatility of the solvent) and rotation rate [89, 90]. For superparamagnetic colloids, either the applied magnetic field or the rotation may create preferred direction or orientation of particles and / or clusters. In that way, orientational order in the coating can be influenced. To study this phenomenon in the experiments of dilute dispersion of superparamagnetic particles, geometry and the orientation of the clusters are characterized by measuring the eccentricity of a cluster. The mean eccentricity of the clusters increases (up to 10%) with increasing applied field (fig. 5.10). Eccentricity is a positive defined number and mean eccentricity is not zero, even at $H = 0$. We found that, within our experimental resolution, the clusters are not oriented (data not shown). There is no privileged direction in our experimental conditions (see fig. 5.1 and fig. 5.2).

5.2.1.5.   Number of nearest neighbors

We analyze the mean number of nearest neighbors of each cluster (fig. 5.11). In the absence of the magnetic field, the mean nearest neighbor value is close to six (with low dispersion in data). This shows that the number density of clusters is high (see fig. 5.8, fig. 5.1–left and fig. 5.2–left). When the magnetic field is applied, their values decrease, with an increasing error bar. This
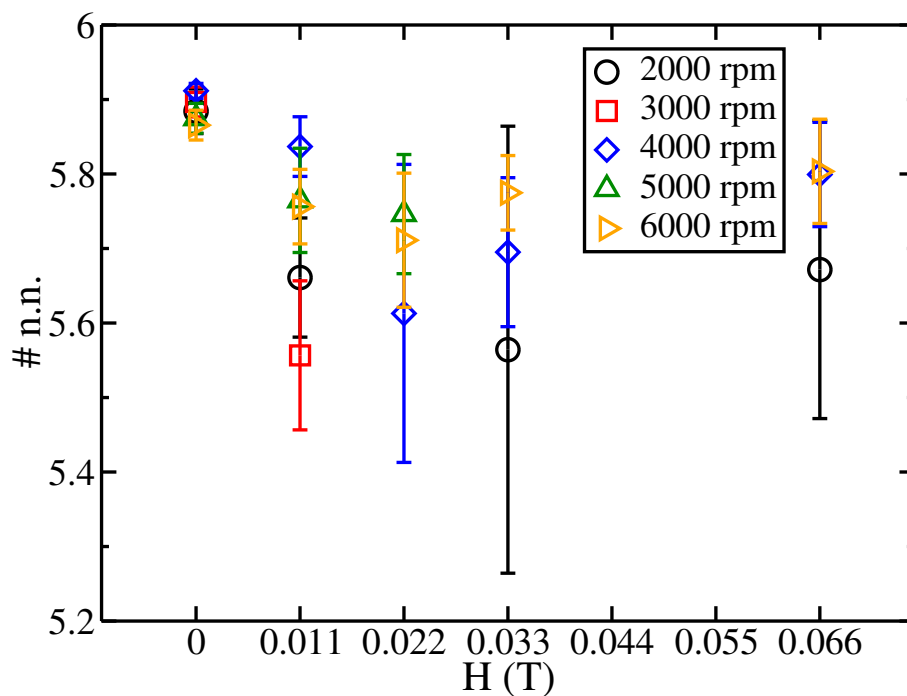
Figure 5.11: Mean number of nearest neighbors of clusters as a function of increasing external magnetic field (colloidal dispersion PS–MAG).

error bar indicates the deposit is submonolayer of superparamagnetic particles. In a hexagonal lattice, the most common defect is penta-hepta, which would not lead to a decrease in mean value of nearest neighbors. Thus, the result obtained is of another nature, which could point out the organization of clusters.

Hence, within the experiment resolution, the clusters are neither oriented nor ordered.

The fluid dynamics of the spin-coating process (fluid on a rotating disk problem) has been studied extensively from the perspective of thinning Newtonian liquid droplets [69–71, 79]. It is possible to broaden these continuum models (e.g. Emslie's one [69] or Meyerhofer's one [70] or Cregan's one [79]) to colloidal dispersions by taking into account the particulate nature of the spin-coated deposits. In the following section, we present a model for the colloidal spin-coating.

5.2.2. Model for colloidal spin-coating

We propose a model for colloidal spin-coating by considering the evaporation of the solvent. The model is used to study the final film thickness of the dried deposits. Colloidal dispersion of monodisperse superparamagnetic particles (SiO_2–MAG) is used in the spin-coating experiments. Sets of micrographs, in the absence of magnetic field (fig. 5.12–A, C, E) and in the presence of magnetic field, H=0.066 T (fig. 5.12–B, D, F) are shown. The spinning rate is 3000 rpm for A and B; 5000 rpm for C and D; 7000 rpm for E and F. For a given micrograph, we calculate the area occupied by the clusters of superparamagnetic particles relative to total area of the region. As it has been mentioned already, this value is called "occupation factor" ε^2, or surface coverage, and it is equivalent to the dimensionless thickness of a multilayer deposit. We calculate the occupation

factor for each image and the spatially averaged values are used for further analysis.

Emslie *et al.* [69] modeled spin-coating system without taking into account the evaporation of the solvent. The model accounts for (a) the viscous forces caused by the fluid properties and (b) the centrifugal forces of spinning. When a polymer solution is spun, it leaves a thin layer deposit indicating that the solvent has been evaporated. To account for the evaporation of solvent, Meyerhofer [70] included a correction based on the assumption that the spin-coating process consists of two different stages: (a) a flow dominated phase followed by (b) an evaporation (of the solvent) dominated phase. Later on, Cregan *et al.* [79] considered that the solvent evaporation is simultaneous with the flow dominated phase. The solvent starts to evaporate once the dispersion is pipetted on to the spinning substrate. In the following, we summarize their arguments.

The deposited layer thickness ($h_\infty^{(s)}$) is given by equation 5.1, where $h_0^{(s)}$ and $h_0^{(l)}$ are the initial solute and the solvent thickness, respectively ($h_0^{(s)} + h_0^{(l)}$ is the initial film thickness). $\alpha = \frac{2\omega^2}{3\nu}$ where ω is the spinning rate and ν is the kinematic viscosity of the solvent. E corresponds to the evaporation rate of the solvent.

$$h_\infty^{(s)} = \frac{h_0^{(s)}}{h_0^{(l)}} \left(\frac{E}{\alpha}\right)^{\frac{1}{3}} \tag{5.1}$$

It is assumed that the initial dispersion is homogeneous. Then, the thicknesses can be translated into volumes and hence $\frac{h_0^{(s)}}{h_0^{(l)}} = \frac{C}{1-C}$, where C is the initial concentration in v/v. Equation 5.1 thus becomes,

$$h_\infty^{(s)} = \frac{C}{1-C} \left(\frac{3}{2}\nu E\right)^{\frac{1}{3}} \omega^{-\frac{2}{3}} \tag{5.2}$$

Cregan's model [79] assumes that E does not depend on ω. Consequently,

$$h_\infty^{(s)} = A\omega^{-\frac{2}{3}} \tag{5.3}$$

where A is a constant over the experiment. Other models [32, 70] assume $E \propto \omega^{\frac{1}{2}}$ or $E \propto \omega$.

We consider a reference experiment reported by Giuliani *et al.* [90]. They used non magnetic SiO_2 particles dispersed in Methyl Ethyl Ketone (MEK). The concentration was 20% v/v and experiments concerning this dispersion are referred as SiO_2–NM. Spatial averaged final deposit thickness (h^*) for the non magnetic SiO_2 particles (measured using Atomic Force Microscopy) is obtained from fig. 4a of the reported [90] reference experiment (reprinted here in fig. 5.13)[1]. In fig. 5.13, deposit thickness is plotted as a function of radial distances for different ω (these data correspond to circles in fig. 5.15 and they are plotted for several ω).

We define compact equivalent height (h_∞) as the thickness of a homogeneous layer whose volume is the same of the particles deposited. This parameter accounts the particulate character in spin-coated deposits. A sketch to explain this parameter is shown in fig. 5.14.

By assuming the equation 5.3, compact equivalent height for reference experiment (SiO_2–NM) can be represented as

---

[1]The spatial average is obtained for the increasing radial distances from the center of rotation; however, it is possible to obtain the average over the whole substrate in three dimensions. This kind of approach might provide additional information concerning the thickness distribution of the spin-coated film over the entire substrate.
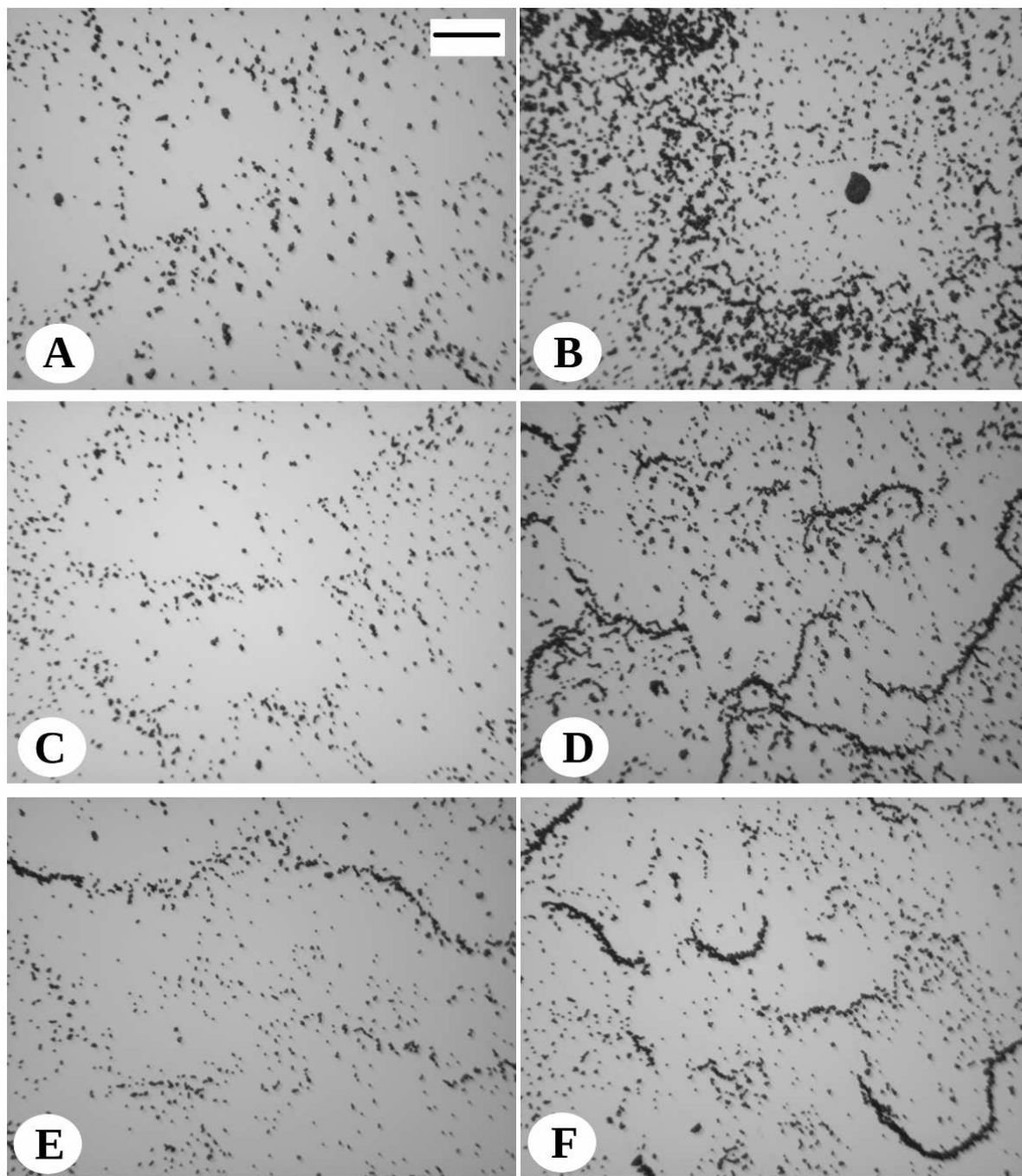
Figure 5.12: Micrographs of spin-coated substrate (with SiO_2–MAG dispersion of concentration 1.44% v/v) at 8 mm from the center of spinning. For A, C and E, the magnetic field $H = 0$ and for B, D and F, the applied magnetic field $H = 0.066$ T. Spinning rate is 3000 rpm for A and B; 5000 rpm for C and D; 7000 rpm for E and F. When the magnetic field is applied, the superparamagnetic particles accumulate together to form clusters (B, D and F). Scale bar for all the images is 50 μm.
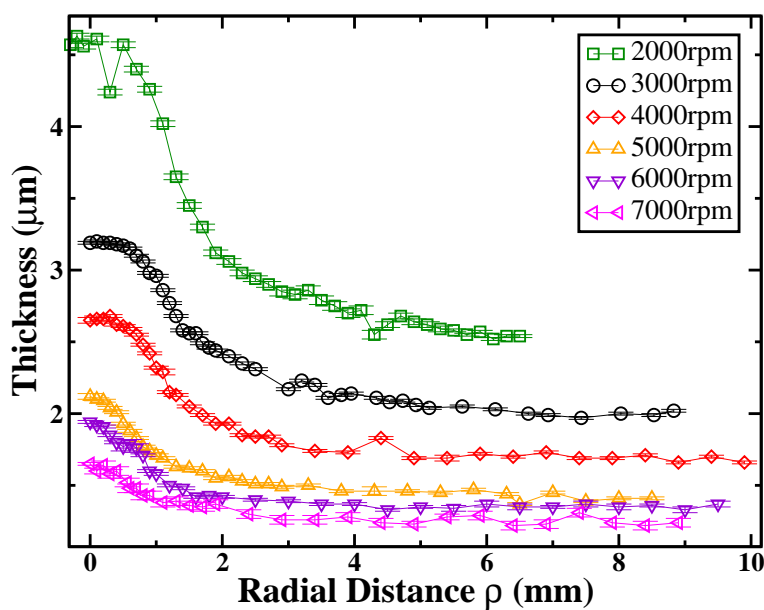
Figure 5.13: AFM thickness profiles at different rotation rates for non-magnetic particles (SiO$_2$) with Methyl Ethyl Ketone as solvent. Initial concentration was 20% v/v. Modified figure reprinted from [90].
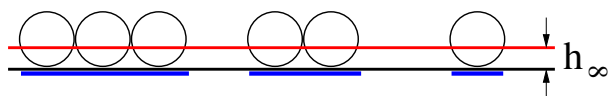
Figure 5.14: A sketch of the thickness parameter, compact equivalent height (h_∞), whose volume is the same of the particles deposited. Sketch is obtained from Dr. W. González–Viñas and it is modified.

$$h_\infty^{(s,ref)} = A_{ref}\omega^{-\frac{2}{3}} \tag{5.4}$$

where, $A_{ref} = \frac{C_{ref}}{1-C_{ref}}\left(\frac{3}{2}\nu_{ref}E_{ref}\right)^{\frac{1}{3}}$. Parameters related to A_{ref} can be obtained from the SiO$_2$–NM reference experiments [90] which include: C_{ref}, or the initial concentration of dispersion (20% v/v); ν_{ref}, or the viscosity of the solvent MEK used to prepare the dispersion (0.5217 cSt); and E_{ref}, or the dimensional evaporation rate of the solvent MEK. However, evaporation rates are usually referred to the one of n-Butyl Acetate. So, $E^* = 3$, which means 3 times the evaporation rate greater than n-Butyl Acetate.

Multilayers (e.g. from SiO$_2$–NM experiments) can be represented in terms of compact equivalent height which is proportional to the number of layers (n).

$$h_\infty^{(s,ref)} \propto n \tag{5.5}$$

By considering the most common different kinds of crystal structure in spin-coated films, the compact equivalent height can be given as

Case (i) fcc$_{100}$

$h_\infty^{(s,ref)} = \frac{2\pi}{6}R\cdot n = \frac{2\pi}{6}R\left(\sqrt{2}\frac{h^*}{2R} + 1 - \sqrt{2}\right) = \frac{\pi}{3\sqrt{2}}h^* + \left(1 - \sqrt{2}\right)\frac{2\pi}{6}R$, where R is the radius of the particle and h^* is the dimensional spatially averaged deposit thickness (measured, e.g. using Atomic Force Microscopy) and can be obtained from plots like fig. 4a of [90].

Case (ii) hcp

$$h_\infty^{(s,ref)} = \frac{2\pi}{3\sqrt{3}}R\cdot n = \frac{2\pi}{3\sqrt{3}}R\left(\sqrt{\frac{3}{2}}\frac{h^*}{2R} + 1 - \sqrt{\frac{3}{2}}\right) = \frac{\pi}{3\sqrt{2}}h^* + \left(1 - \sqrt{\frac{3}{2}}\right)\frac{2\pi R}{3\sqrt{3}}$$

Hence, in both structures, for $n \gg 1$,

$$h_\infty^{(s,ref)} \approx \frac{\pi}{3\sqrt{2}}h^* \tag{5.6}$$

In the experiments of SiO$_2$–MAG (without the applied magnetic field), the morphologies of superparamagnetic particles are submonolayers and hence the compact equivalent height is proportional to the occupation factor (ε^2).

$$h_\infty^{(s,mag)} \propto \varepsilon^2 \tag{5.7}$$

We assume the packing for these submonolayers is hexagonal. Hence,

$$h_\infty^{(s,mag)} = \frac{2\pi}{3\sqrt{3}}R\varepsilon^2 \tag{5.8}$$

where R is the radius of the particle.

Comparing multilayer (SiO$_2$–NM) and submonolayer (SiO$_2$–MAG) experiments,

$$\frac{h_\infty^{(s,ref)}}{h_\infty^{(s,mag)}} = \frac{1}{2}\sqrt{\frac{3}{2}}\frac{h^*}{R\varepsilon^2} \tag{5.9}$$

Figure 5.15: Comparison of the film thickness profile for different colloids in the absence of the magnetic field. Squares: SiO_2–MAG (superparamagnetic particles are silica coated magnetite of diameter 1.51 μm dispersed in ultra pure water); Diamond: PS–MAG (superparamagnetic particles are polystyrene coated magnetite of diameter 1 to 2 μm dispersed in ultra pure water); Circles: SiO_2–NM (silica nonmagnetic particles of diameter 458 nm were dispersed in MEK and information is extracted from fig. 4a of the reference experiment reported in [90], by doing a spatial average). Data from the experiments collapse to a single curve. Experimental data are compared with the model (dashed line) proposed by Cregan *et al.* [79]. The mean occupation factor values for PS–MAG are given in section 5.2.1.3 (page 79) and in fig. 5.9.

Scaled height profile for submonolayer (SiO$_2$–MAG) experiments can be constructed using equation 5.9. This will allow to compare both kinds of experiment.

$$h_{scaled} = 2\sqrt{\frac{2}{3}}R\varepsilon^2 \frac{h_\infty^{(s,ref)}}{h_\infty^{(s,mag)}} \tag{5.10}$$

By assuming Cregan's equation, SiO$_2$–MAG experiments can be presented as

$$h_\infty^{(s,mag)} = A_{mag}\omega^{-\frac{2}{3}} \tag{5.11}$$

where $A_{mag} = \frac{C_{mag}}{1-C_{mag}}\left(\frac{3}{2}\nu E\right)^{\frac{1}{3}}$. For A_{mag}, where C_{mag} is the initial concentration of superparamagnetic colloidal dispersion (1.44% v/v), ν represents the viscosity of the solvent (ultra pure water) and E is the evaporation rate of the ultra pure water, these values can be obtained from the experiments of SiO$_2$–MAG.

By using the equations 5.4 and 5.11, SiO$_2$–MAG experiments can be compared directly with the SiO$_2$–NM reference experiments.

$$h_{scaled} = 2\sqrt{\frac{2}{3}}R\varepsilon^2 \frac{A_{ref}}{A_{mag}} \tag{5.12}$$

h_{scaled} values are calculated for SiO$_2$–MAG experiments using the equation 5.12. This scaled thickness (squares in fig. 5.15) is compared with the spatial averaged final deposit thickness (h^*) of SiO$_2$–NM experiments (circles in fig. 5.15). Although the particles and the solvents are of different characteristics, data collapse to a single curve – a universal behavior of colloids under spin-coating.

Mean occupation factor values ε^2, for PS–MAG (polystyrene coated magnetite particles, see page 79 and fig. 5.9) are scaled to obtain the film thickness, h_{scaled}. Polydispersity of PS superparamagnetic particles has an influence on R (in equation 5.12). Mean film thickness for these PS–MAG experiments is compared qualitatively (diamonds in fig. 5.15). Most of the mean values (at 2000, 4000 and 6000 rpm) show a decreasing tendency, similar to other kind of dispersions (non-magnetic and SiO$_2$–MAG). The standard deviation in h_{scaled} values for PS–MAG dispersion comes from the polydispersity of the superparamagnetic particles.

5.2.3. Comparison with other models

The experimental data are compared with the model reported by Cregan *et al.* [79]. They propose a theoretical calculation on the final dimensional layer thickness of the spin-coated films. A power-law fit respective to this model is plotted (fig. 5.15–dashed line and fig. 5.16–dotted line). The experimental data are in good agreement with this fit. Power-law fit to the non-magnetic particles, reference experiment, (solid line in fig. 5.16) shows a strong dependency on the spinning rate, $\sim \omega^{-0.74\pm0.03}$. The exponent value is close to the one presented in the model of V. Cregan *et al.* [79], $\left(-\frac{2}{3}\right)$, which considers that the solvent evaporation as simultaneous. This indicates, irrespective of the nature and the kinds of dispersion, that the final film thickness mostly depends on the spinning rate.

Relevant power-law fits are constructed using models from [32, 70]. They are shown in fig. 5.16. The experimental data deviate slightly from the two models presented in [70] and [32], as shown by the triangles and open circles, respectively, in fig. 5.16. As said before, the assumption by
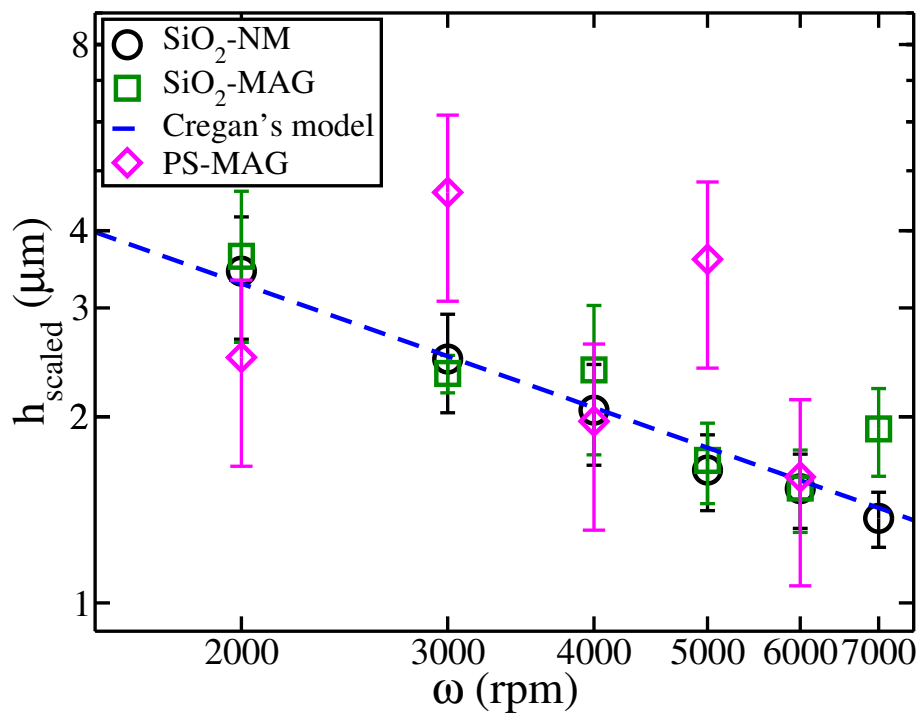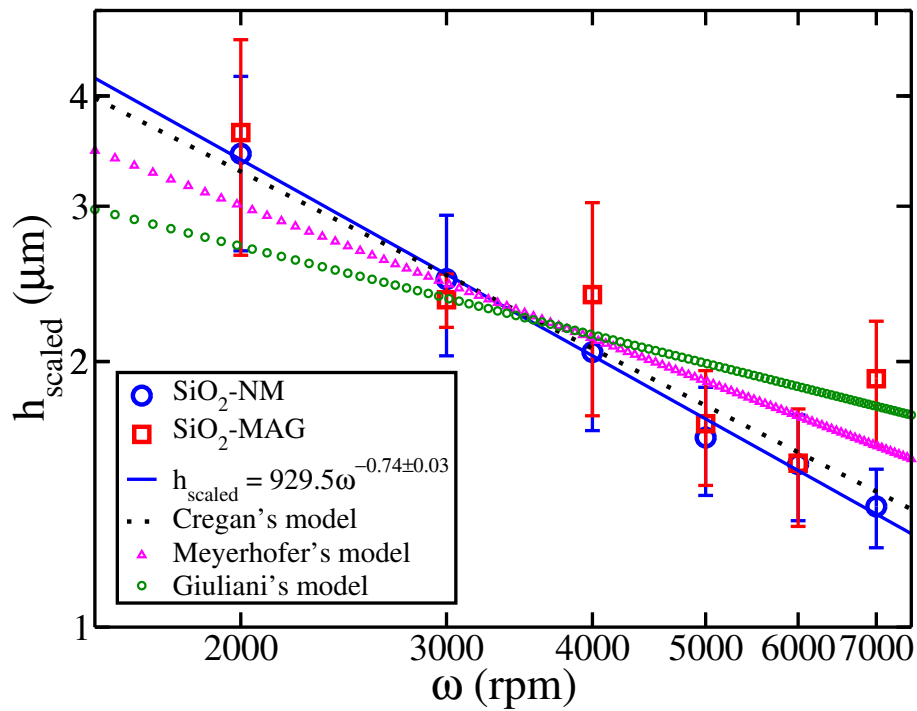
Figure 5.16: Comparison of the film thickness profiles for different dispersions in the absence of the magnetic field. Squares: SiO$_2$–MAG; Circles: SiO$_2$–NM. The experimental data for both dispersions collapse to a single curve. Solid line is the best power-law fit to the non-magnetic particles (SiO$_2$–NM reference experiment). The experimental data are compared with the models [32, 70, 79]. Dotted line corresponds to model proposed by Cregan *et al.*. Triangles represent the model from Meyerhofer and the open circles are obtained from [32].

Meyerhofer is that the spin-coating process contains two different stages, a flow dominated one followed by an evaporation of the solvent. But in our case, we assume [79] that once the dispersion is pipetted on the spinning substrate, the shear makes the solvent evaporation simultaneous. Another relevant model proposed by Giuliani *et al.* [32] features similar problem, but they focus on the drying fronts approaching to the center of spinning. All these models [32, 70, 79] are compatible with our experimental results.

5.2.4.   Relative viscosity
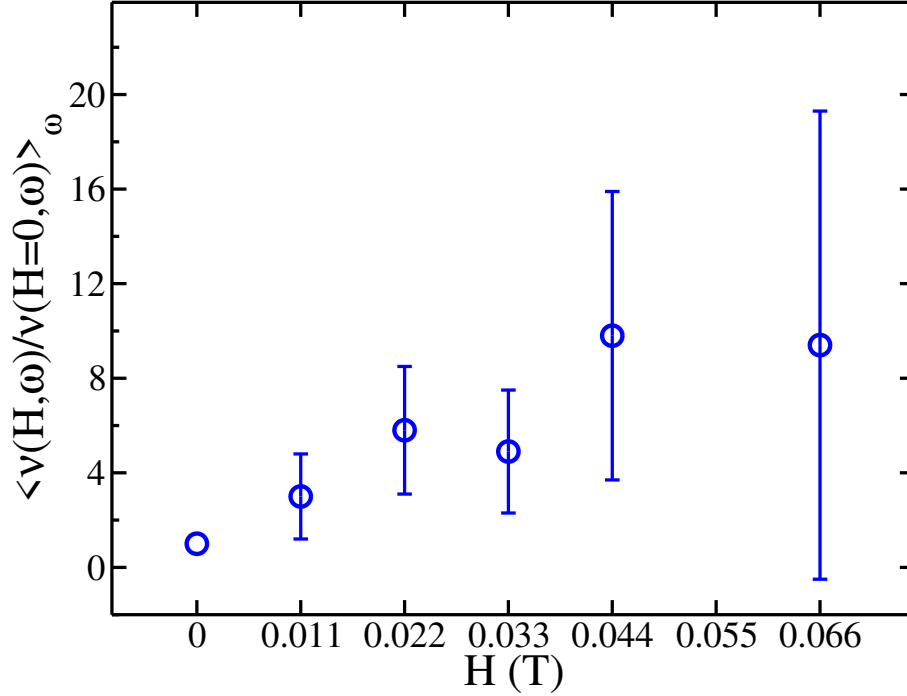
Figure 5.17: Relative change in the viscosity for all spinning rates as a function of the applied magnetic fields.

In the absence of the magnetic field ($H = 0$), equation 5.11 is obtained by assuming the Cregan's model [79] which is shown before in the equations 5.1, 5.2 and 5.3. Equation 5.11 can be generalized in such a way that E may depend on ω, and when the magnetic field H is applied while spin-coating, it becomes

$$h_\infty^{(s,mag)}(H,\omega) = \frac{C_{mag}}{1 - C_{mag}} \left[\frac{3\nu(H,\omega)E(\omega)}{2\omega^2} \right]^{\frac{1}{3}} \tag{5.13}$$

and consequently,

$$\frac{h_\infty^{(s,mag)}(H,\omega)}{h_\infty^{(s,mag)}(0,\omega)} = \left[\frac{\nu(H,\omega)}{\nu(0,\omega)} \right]^{\frac{1}{3}} \tag{5.14}$$

In the experiments of SiO$_2$–MAG (with and without the presence of the magnetic field), the morphologies of superparamagnetic particles are submonolayers and hence the compact equivalent

height is proportional to the occupation factor ε^2. By using the equation 5.8 in equation 5.14

$$\frac{\nu(H,\omega)}{\nu(0,\omega)} = \left[\frac{\varepsilon^2(H,\omega)}{\varepsilon^2(0,\omega)}\right]^3 \tag{5.15}$$

The equation 5.15 is independent on the models used among [32, 70, 79].

Using the above equation, the relative change in viscosity due to the applied magnetic field can be calculated. Information about ε^2 is obtained directly from the experiments. For a given magnetic field, we plot (fig. 5.17) the mean and standard deviation (in the appearance of error bars) for relative change in viscosity for all ω. The mean relative viscosity increases as the magnetic field is increased. Magnetic fields may increase the mean relative viscosity through the magnetic dipole interactions between the superparamagnetic particles. At high magnetic fields, more number of particles can accumulate in elongated clusters. Morphological transition from sparse (absence of the magnetic field) to submonolayer deposits (presence of the magnetic field) of superparamagnetic particles can be seen in fig. 5.12–A to B, C to D and E to F. We do not observe any preferred direction for these clusters, and orienting them in a desired direction is challenging. Standard deviation in each value (fig. 5.17) shows the qualitative dependence on the spinning rate ω. Nonetheless, one can relate the increase of standard deviation to an increase in non-Newtonian character [66, 91, 117] as the applied fields are increased.

Further work has to be carried out to study this phenomena in depth. To start with, increasing the initial concentration of superparamagnetic dispersion may provide insights concerning this phenomena. Also it could direct in observing privileged directions for the clusters of superparamagnetic particles when the external magnetic field is applied.

5.3. Spin-coating of colloids in electric field

Giuliani *et al.* [90] reported mechanisms and dynamics of structure formation while spin-coating a colloidal dispersion of volatile solvent (high concentration, silica particles, 20% v/v). They studied how the thinning dynamics is relevant to final deposit of particles. These spin-coated crystals (final deposits), with micron-scale building blocks show structural colors (iridescence) when illuminated with white light. Depending on the nature of microscopic packing of colloidal particles [89], white light reflections are varied. 4-fold symmetry and 6-fold symmetry are observed in colloidal spin-coating [87–90]. The symmetric radial arms arise from axial symmetry imposed by the spinning [89, 90, 118, 119]. These crystals are intrinsically polycrystalline with different microscopic crystallites being orientationally correlated with one another (short range positional order and long range orientational order). Hence they are termed "orientationally correlated polycrystals" (OCP) [89]. Monodomain, defect-free, large area colloidal crystals are of great interest in fabricating inexpensive photonic band gap materials [120–124].

The polycrystalline nature of these spin-coated colloidal films is thus a major obstacle to use them as viable photonic materials. To obtain crystallites in a preferred direction, it is necessary to overcome the axial symmetry from spin-coating. To break the symmetry, nonuniform external alternating electric fields are applied (while spinning). The field could affect the outward flow of fluid during the process and might break the axial symmetry. Nonmagnetic silica particles are used to prepare the colloidal dispersion of concentration 20% v/v. The spinning rate for all the

experiments is 2000 rpm.

5.3.1. Dielectrophoresis
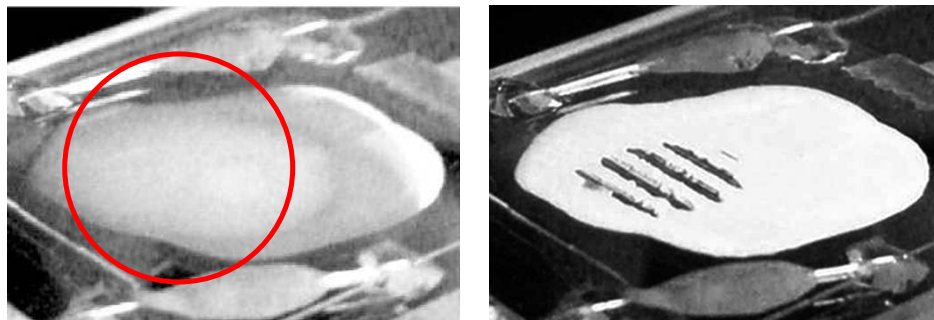
Figure 5.18: Demonstration of dielectrophoretic localization of colloidal dispersion in the absence of spinning. (left) In the absence of electric field: the white colloidal dispersion can be seen inside the red circle. (right) With electric field of 0.47 kV/mm and 40 kHz: here the colloidal dispersion has been redistributed towards the electrode regions.

When the field is turned on, colloidal dispersion experiences a non-uniform force and the dominant mechanism for this field-induced migration of fluid is dielectrophoresis (DEP). Three dielectric media are present in our experimental system: (i) colloidal particles (in our case, $\epsilon_{\mathrm{p}} \sim 4$) (ii) solvent ($\epsilon_{\mathrm{s}} = 15.5$) and (iii) air ($\epsilon_{\mathrm{air}} = 1$). Two Clausius-Mosotti factors can be written for $K_{\mathrm{solvent\text{-}air}} = 0.8$ and $K_{\mathrm{particle\text{-}solvent}} = -0.3$. In our experiments, it is expected that solvent DEP (solvent–air) will be the predominant mechanism, while particle DEP can additionally be relevant. Also, at these applied frequencies, electro-osmotic effects can play a role; however, frequency dependence has to be explored.

Figure 5.19: (left) Spin-coated sample at zero field shows 4-arm reflection patterns that is characteristic of axisymmetric spin-coating. (right) Spin-coated sample in the presence of applied electric field, 0.95 kV/mm and 3 kHz. Magenta and blue arrows show the interdigitated ITO electrodes connected to the amplifier (magenta arrows point to the grounded electrode G). Here, the final sediment shows no remnant of axial symmetry.
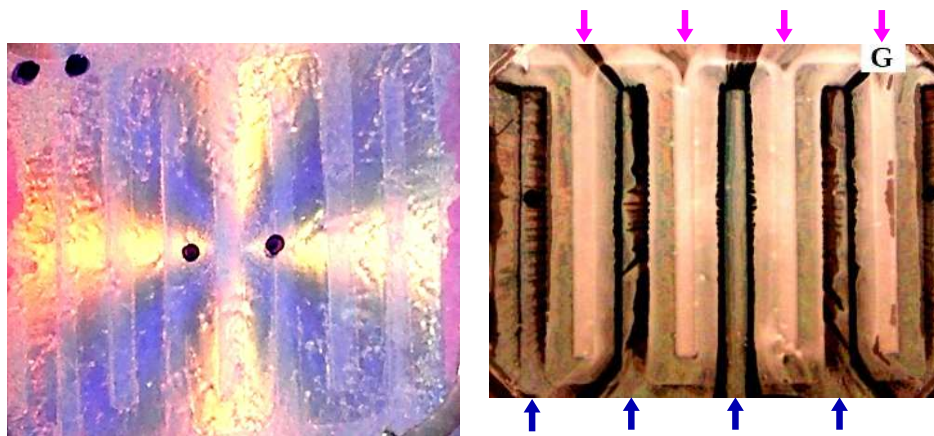
5.3.1.1.   Dielectrophoretic localization – absence of spinning

Dielectrophoretic localization of colloidal dispersion without spinning is shown in fig. 5.18–left (absence of electric field) and fig. 5.18–right (presence of electric field). Dispersion inside the drawn red circle in fig. 5.18–left is redistributed towards the electrode region when a field of 0.47 kV/mm and 40 kHz is applied. The solvent gets evaporated and the drying continues to leave a thick white deposit (fig. 5.18–right).

5.3.1.2.   Dielectrophoretic localization – presence of spinning

In the presence of spinning and absence of electric field, orientationally correlated polycrystals [89] are obtained (fig. 5.19–left). The symmetric arms can be understood from [89, 90]. When the external field is applied, two changes in the spin-coated deposits (fig. 5.19–right) are observed by eye: reflection arms due to axial symmetry (seen in zero field, fig. 5.19–left) are not present. Also, the deposits of colloidal particles are localized to certain regions of the pattern.
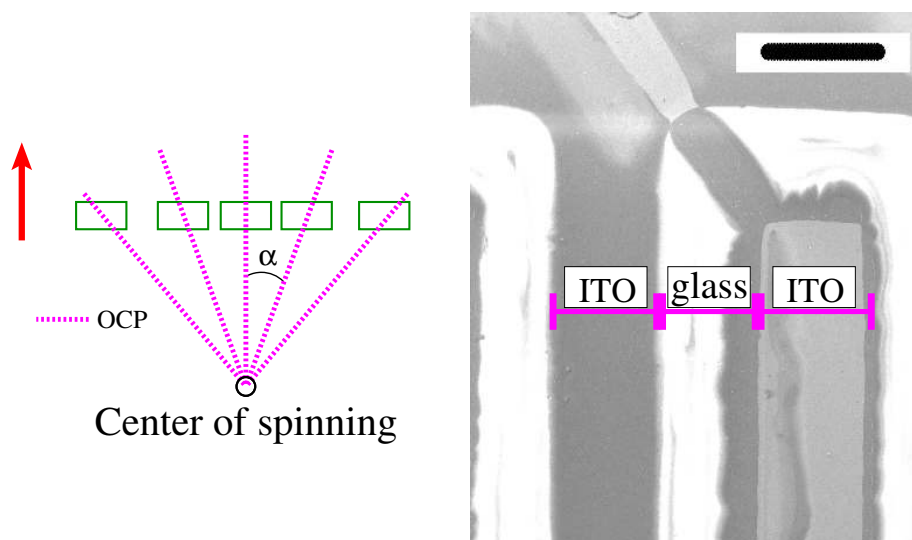
Figure 5.20: (left) Sketch for the positions of the analyzed zones by SEM (rectangles) over the spin-coated sample. α is the "pattern angle", defined by the angle between the direction of the pattern (red arrow) and the radial position of the image (analyzed zone) relative to the center of spinning (refer text for explanation). Magenta dotted lines illustrate the directions at which the orientationally correlated polycrystals would be oriented in the absence of electric field. (right) Low magnification SEM overview of relevant regions in the spin-coated samples (glass and ITO). Scale bar is 1 mm.

5.3.2.   Microscopic analysis

Although the deposits of colloidal particles seem to be along the pattern (macroscopic observation), effects due to the electric field can be seen through the microscopic arrangement of these colloidal particles. To study the microscopic distribution and orientation of these particles, scanning electron micrographs (SEM) are obtained at different positions over the sample relative

to the center of rotation. The angle between this radial vector and direction of pattern in the ITO substrate is termed as "pattern angle" α (fig. 5.20–left). Dotted lines in fig. 5.20–left show the directions at which OCP [89] would be oriented in the absence of electric field. The zones analyzed by SEM over the spin-coated sample are also sketched (fig. 5.20–left) as rectangles. In the spin-coated sample, these green rectangles can fall into one of the two regions (fig. 5.20–right); either over the ITO electrode region, that is connected to the voltage amplifier, or over the glass which is a non-conducting region between the two ITO electrodes.
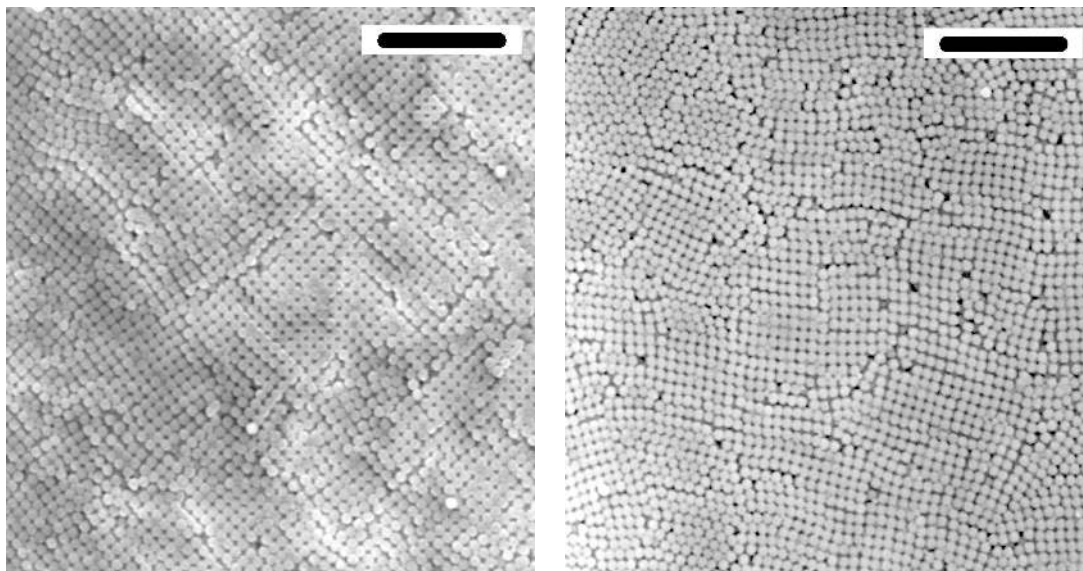
Figure 5.21: SEM micrographs. (left) In the absence of electric field and $\alpha = 45°$. (right) In the presence of electric field 0.95 kV/mm, 3 kHz obtained for glass region and $\alpha = 49°$. Scale bars are 5 μm.

5.3.2.1. Domain orientation

The orientation of the microscopic domains for each SEM micrograph can be calculated. A direction at which the maximum number of microscopic domains are oriented is termed as dominant orientation of the domains (θ). The orientations are compared with the pattern angle (α) as shown in fig. 5.22. In the absence of electric field, the orientation of domains is expected to follow α ($\theta = \alpha$) [89] and it is observed in SEM (fig. 5.21–left). Circles in fig. 5.22 show this behavior and they lie on the dashed line that corresponds to $\theta = \alpha$.

On applying the electric field, axial symmetry has been broken. Hydrodynamic shear forces and electrostatic forces compete in trying to orient the domains (fig. 5.21–right). In principle, with the applied field, perfect orientation along the field would result in $\theta = 0$, independent of α. The domain orientation induced by the applied field is shown in fig. 5.22–squares. It is much more effective in the glass regions of the substrate (blue squares) than in the ITO electrode region (red squares) because the electric field gradient is higher in the former than in the latter (section 4.3.3).
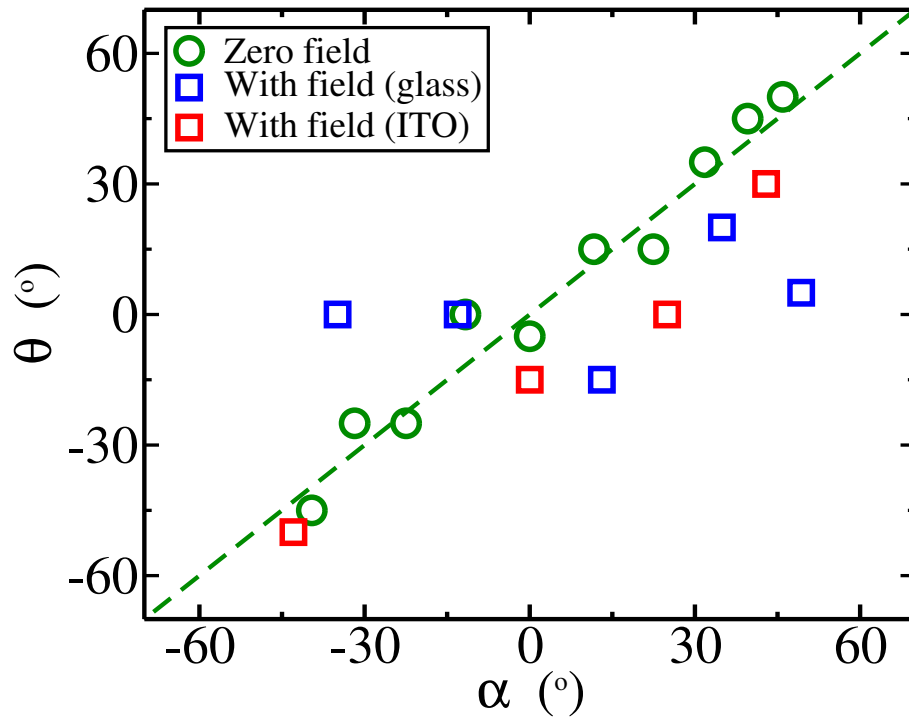
Figure 5.22: Dominant domain orientation angle θ as a function of pattern angle α. Green circles–absence of electric field. Squares–applied electric field (0.95 kV/mm at 3 kHz). The condition for orientationally correlated polycrystals ($\theta = \alpha$) is shown by the dashed line. Domain orientation along the direction of the ITO pattern corresponds to $\theta = 0$. Red and blue squares represent the ITO and the glass region on the substrate, respectively.

5.3.2.2. Efficacy of the applied field

Figure 5.23: Slopes of the linear fits, m_g, for the dominant orientation of domains (glass region data, see e.g. 5.22) against the applied field strength, showing a systematic decrease from close to unity (OCP) to close to zero (direction of the ITO pattern). Applied frequency is 3 kHz.

For a given experiment, a linear fit is plotted for the dominant orientations, θ obtained from the glass regions. The slopes of these fits, $m_g = d\theta/d\alpha$, are plotted (fig. 5.23) against the applied field strength (E), which give quantitative information on the efficacy of the electric field in orienting the domains. Unidirectional orientation of the colloidal crystalline domains along the direction of the ITO pattern corresponds to $\theta = 0$. Thus, when the field completely determines the domain orientation, $\theta = 0$, independent of α and $m_g = 0$.

For glass region, the slope m_g decreases from a value of 1. This value is expected for an OCP. Decreasing m_g represents the domains are orienting and a value close to zero validates the field-induced orientational order of domains. For ITO electrode region, fig. 5.24, the effects due to the field are minimal. The calculated slope is close to unity, which represents the microscopic domains are orientationally correlated. Also, an asymmetry is observed in the colloidal deposit between the ground and oscillating voltage electrode regions (fig. 5.19–right and fig. 5.20–right). This could possibly be related to opposing solvent-in-air and particles-in-solvent dielectrophoretic flows and/or to some capacitive effects in the system. Further experiments are in progress to study this phenomena.
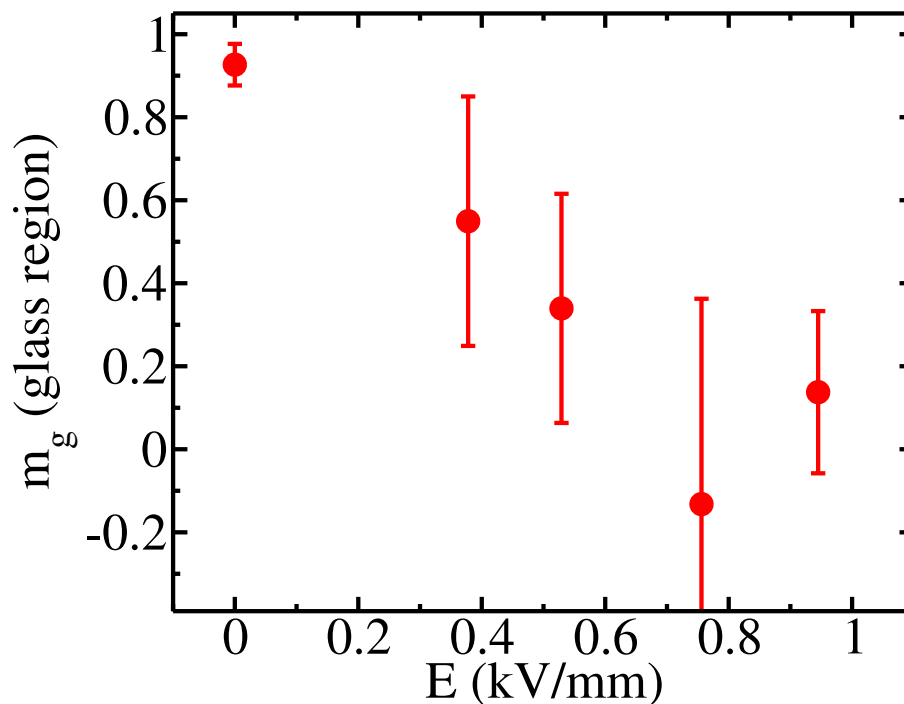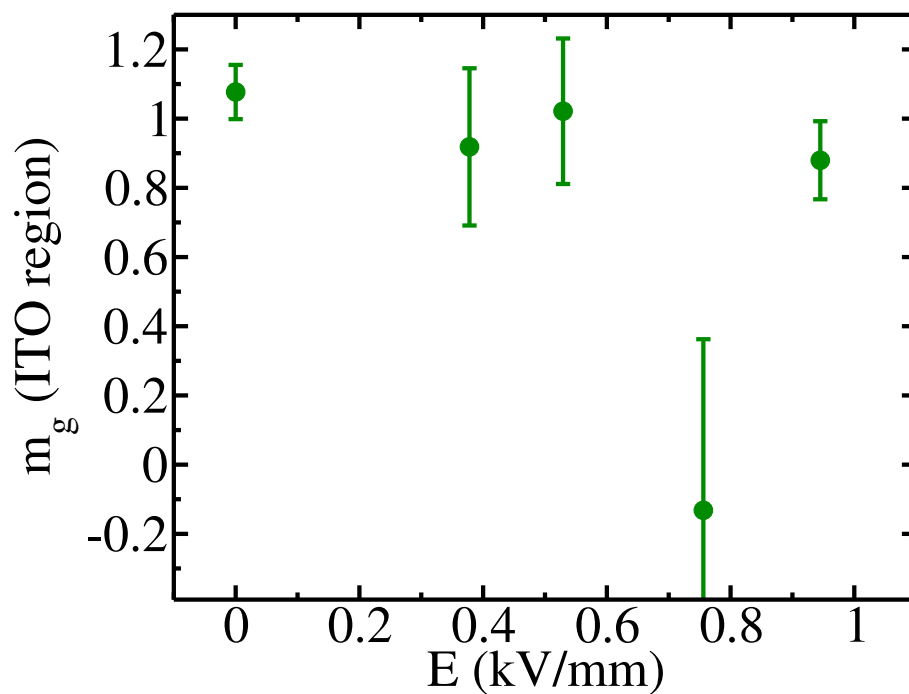
Figure 5.24: Slopes of the linear fits, m_g, for the dominant orientation of domains (ITO electrode region data, see e.g. 5.22) against the applied field strength, showing that the field effects are reduced. The slope m_g remains close to unity indicating OCP. Applied frequency is 3 kHz.

Conclusions and Outlook

Conclusions

The most important parameter in the evaporation induced self-assembly of colloidal particles is the rate at which the continuous phase is removed from the colloidal dispersion. The choice can be of a quasi-static phase transition, that may result in particle arrays with long range order and few defects. This process is too long and to target a desired structure remains complex. Hence, it is less preferred. In contrast, far–from–equilibrium phase transitions provide in-situ variables of the experiment that can be either controlled or tuned while the phase transition is in process; however, the involved kinetic mechanisms are more complex to understand and to characterize. *This Thesis focuses on the non equilibrium phase transition in the colloidal system and on how the in-situ variables during the transition are influenced by external fields.*

In this experimental work, we study the influence of the external fields on the colloidal dispersion of dissimilar properties in a different perspective. The external fields are applied when the colloidal dispersion undergoes an evaporative phase transition (from liquid dispersion to solid deposits). Consequently, the colloidal particles are deposited onto the substrate. We investigate the effects of the applied field by studying the obtained morphology of colloidal deposits and correlating it with the external field and the experimental conditions. The experiments are performed in such a way that the fluid phase can be withdrawn in two different time scales.

(i) <u>In a longer time scale</u> (the fluid is removed slowly, relative to (ii) given below), experiments are performed using dilute colloids (concentration of the order of 0.1% w/w) in the vertical deposition technique. **Applied weak DC field (as weak as 1 V/mm) influences the particle pool zone and consequently affects the kind of morphology of colloidal deposits as well as the speed of the receding contact line**. Our experimental setup provides a control over the amount of particles given in a localized region and thus **the field induced manipulation of self-assembly is possible**; however, the present setup has some limitations in quantifying the flows and its association with the external field. The attention can be drawn by employing an observation at higher resolution. In a similar perspective, **external alternating weak electric fields (as weak as 1 V/mm; frequency of the order of 1 Hz) generate local flows in the meniscus region of a static contact line. The flows form periodic colloidal clusters along the horizontal contact line**. Our experimental setup provides important clues in the understanding of the three phase contact line in the colloidal system. Likewise, **our method demonstrates a direct approach to obtain the structured patterns of colloids over non patterned substrates**.

(ii) <u>In a shorter time scale</u> (the fluid is removed quickly, relative to (i) given above), experiments are performed using colloids of different nature and concentration in the spin-coating technique. **In the case of concentrate colloids of silica particles (concentration 40% w/w), application of a non uniform alternating high electric field stationary in the rotating frame (electric field strength of the order of 0.1 kV/mm; frequency of the order of 1 kHz) during the spin-coating provides the deposits of colloidal particles in a predefined direction and the axial symmetry from the spin-coating breaks**. However, this method lacks in fabricating monodomain, defect-free colloidal crystals. **In the case of dilute colloids of superparamagnetic particles (concentration 2.427% w/w), application of an axial magnetic field during the spin-coating provides clusters of superparamagnetic particles**. In our experiments, the application of magnetic field to the dilute superparamagnetic colloids does not lead to any privileged direction for these clusters (clusters are neither oriented nor ordered). Hence, **the main effect of the applied magnetic field is the change of the rheology of the dispersion while spin-coating**. Thus, **spin-coating can be employed as a probe to measure the microrheology**. **It is possible to extend the continuum models** (e.g. Cregan's one [79]) **to colloidal dispersions by considering their particulate nature**. Moreover, in the absence of magnetic field, a general relation is drawn that compares the final film thickness of the different kinds of colloid (non magnetic and superparamagnetic, respectively).

Outlook

Vertical deposition is a promising technique to obtain domains of ordered colloidal particles. The microscopic effect of the hydrodynamical flows that occur in the bulk dispersion due to the evaporation of the continuous phase is not yet clear. Besides, these flows are crucial for the improvement of the structure formation and hence, highly periodic morphology. One can control the amount of particles for deposition (near the contact line) by directing these flows. The characterization of the flows during the deposition can be performed by in-situ particle tracking methods. Furthermore, vertical deposition technique can be used to pattern the substrates in a simplistic mean by exploiting the capillary flows due to the porosity of the previously deposited structures. When the contact line recedes over the periodic clusters, capillary flows towards the clusters might strengthen, and elongated columns of particles can be deposited on the substrate. Subsequently, the whole substrate is patterned with the colloidal columns in a straightforward manner. A collaborative work is being carried out with R. Aslam, of our group.

Spin-coating method is highly recommended for the large scale fabrication of polymer thin films. Nevertheless, research groups demonstrated viable approaches to extend this method for colloidal dispersions. Axial symmetry from the spin-coating limits the broad application of this method and the symmetry breaking mechanisms are still under exploration. Application of external fields while spin-coating can be inventive to this problem but, it is not yet optimized for the colloidal systems of vast properties. To initiate these studies, experiments that contribute in constructing a phase diagram for the *colloidal system under shear* might be useful. One needs to take into account the initial concentration, the particle diameter, the properties of the fluid like evaporation rate, viscosity, density etc., and the substrate properties.

Bibliography

[1] I. Langmuir. *The constitution and fundamental properties of solids and liquids. I. Solids.* J. Am. Chem. Soc. **38**, (1916), p. 2221.

[2] I. Langmuir. *The constitution and fundamental properties of solids and liquids. II. Liquids.* J. Am. Chem. Soc. **39**, (1917), p. 1848.

[3] K. B. Blodgett. *Films built by depositing successive monomolecular layers on a solid surface.* J. Am. Chem. Soc. **57**, (1935), p. 1007.

[4] M. C. Petty. *Possible applications for Langmuir–Blodgett films.* Thin Solid Films **210/211**, (1992), p. 417.

[5] G. G. Roberts, P. S. Vincett, W. Barlow. *Technological applications of Langmuir–Blodgett films.* Phys. Technol. **12**, (1981), p. 69.

[6] B. Tieke. *Langmuir–Blodgett films for electronic applications.* Adv. Mater. **2**, (1990), p. 222.

[7] M. Bardosova, M. E. Pemble, I. M. Povey, R. H. Tredgold. *The Langmuir–Blodgett approach to making colloidal photonic crystals from silica spheres.* Adv. Mater. **22**, (2010), p. 3104.

[8] R. G. Shimmin, A. J. DiMauro, P. V. Braun. *Slow vertical deposition of colloidal crystals: A Langmuir–Blodgett process?* Langmuir **22**, (2006), p. 6507.

[9] M. Bardosova, F. C. Dillon, M. E. Pemble, I. M. Povey, R. H. Tredgold. *Langmuir–Blodgett assembly of colloidal photonic crystals using silica particles prepared without the use of surfactant molecules.* J. Colloid. Interf. Sci. **333**, (2009), p. 816.

[10] A. Gil, F. Guitián. *Formation of 2D colloidal crystals by the Langmuir–Blodgett technique monitored in situ by Brewster angle microscopy.* J. Colloid. Interf. Sci. **307**, (2007), p. 304.

[11] P. Massé, S. Ravaine. *The Langmuir–Blodgett technique: A powerful tool to elaborate multilayer colloidal crystals.* Colloid. Surface. A **270–271**, (2005), p. 148.

[12] S. Reculusa, S. Ravaine. *Colloidal photonic crystals obtained by the Langmuir–Blodgett technique.* Appl. Surf. Sci. **246**, (2005), p. 409.

[13] S. G. Romanov, M. Bardosova, M. Pemble, C. M. S. Torres. *(2+1)-Dimensional photonic crystals from Langmuir–Blodgett colloidal multilayers.* Appl. Phys. Lett. **89**, (2006), p. 043105.

[14] J. Diao, J. Hutchison, G. Luo, M. Reeves. *Theoretical analysis of vertical colloidal deposition.* J. Chem. Phy. **122**, (2005), p. 184710.

[15] A. S. Dimitrov, K. Nagayama. *Continuous convective assembling of fine particles into two-dimensional arrays on solid surfaces.* Langmuir **12**, (1996), p. 1303.

[16] P. Jiang, J. F. Bertone, K. S. Hwang, V. L. Colvin. *Single-crystal colloidal multilayers of controlled thickness.* Chem. Mater. **11**, (1999), p. 2132.

[17] J. Li, S. Luan, W. Huang, Y. Han. *Colloidal crystal heterostructures by a two-step vertical deposition method.* Colloid. Surface. A **295**, (2007), p. 107.

[18] Z. Zhou, X. S. Zhao. *Opal and inverse opal fabricated with a flow-controlled vertical deposition method.* Langmuir **21**, (2005), p. 4717.

[19] M. Giuliani, W. González-Viñas. *Contact-line speed and morphology in vertical deposition of diluted colloids.* Phys. Rev. E **79**, (2009), p. 032401.

[20] J. Zhang, X. Luo, X. Yan, G. Zhu. *Fabrication of high-quality colloidal crystal films by vertical deposition method integrated with a piezoelectric actuator.* Thin Solid Films **518**, (2010), p. 5204.

[21] C. Fustin, G. Gasser, H. Spiess, U. Jonas. *Parameters influencing the templated growth of colloidal crystals on chemically patterned surfaces.* Langmuir **20**, (2004), p. 9114.

[22] P. Pieranski, L. Strzelecki, B. Pansu. *Thin colloidal crystals.* Phys. Rev. Lett. **50**, (1983), p. 900.

[23] C. A. Murray, D. H. Van Winkle. *Experimental observation of two-stage melting in a classical two-dimensional screened coulomb system.* Phys. Rev. Lett. **58**, (1987), p. 1200.

[24] P. A. Kralchevsky, K. Nagayama. *Capillary forces between colloidal particles.* Langmuir **10**, (1994), p. 23.

[25] P. Kralchevsky, V. Paunov, I. Ivanov, K. Nagayama. *Capillary meniscus interaction between colloidal particles attached to a liquid–fluid interface.* J. Colloid Interf. Sci. **151**, (1992), p. 79.

[26] N. D. Denkov, O. D. Velev, P. A. Kralchevsky, I. B. Ivanov, H. Yoshimura, K. Nagayama. *Mechanism of formation of two-dimensional crystals from latex particles on substrates.* Langmuir **8**, (1992), p. 3183.

[27] C. Dushkin, H. Yoshimura, K. Nagayama. *Nucleation and growth of two-dimensional colloidal crystals.* Chem. Phys. Lett. **204**, (1993), p. 455.

[28] A. S. Dimitrov, C. D. Dushkin, H. Yoshimura, K. Nagayama. *Observations of latex particle two-dimensional-crystal nucleation in wetting films on mercury, glass, and mica.* Langmuir **10**, (1994), p. 432.

[29] P. A. Kralchevsky, N. D. Denkov, V. N. Paunov, O. D. Velav, I. B. Ivanov, H. Yoshimura, K. Nagayama. *Formation of two-dimensional colloidal crystals in liquid films under the action of capillary forces.* J. Phys.: Condens. Matter **6**, (1994), p. A395.

[30] P. Kralchevsky, N. Denkov. *Capillary forces and structuring in layers of colloid particles.* Curr. Opin. Colloid Interface Sci. **6**, (2001), p. 383.

[31] A. Yethiraj. *Tunable colloids: Control of colloidal phase transitions with tunable interactions.* Soft Matter **3**, (2007), p. 1099.

[32] M. Giuliani. *Colloidal crystal formation through interfacial mechanisms.* Ph.D thesis, University of Navarra (2010) .

[33] R. Lenormand, E. Touboul, C. Zarcone. *Numerical models and experiments on immiscible displacements in porous media.* J. Fluid Mech **189**, (1988), p. 165.

[34] H. Morgan, N. G. Green. *AC electrokinetics: Colloids and nanoparticles.* Research Studies Press Ltd., England (2003).

[35] J. Bockris, A. Reddy. *Modern electrochemistry.* Plenum press, New York (1973).

[36] R. J. Hunter. *Foundations of colloid science.* Oxford Univ. Press, New York (1989).

[37] D. J. Shaw. *Introduction to colloid and surface chemistry.* 3rd ed., Butterworths, London (1980).

[38] P. C. Hiemenz, R. Rajagopalan. *Principles of colloid and surface chemistry.* 3rd ed., Marcel Dekker, New York (1997).

[39] J. H. Masliyah, S. Bhattacharjee. *Electrokinetic and colloid transport phenomena.* John Wiley and Sons, Inc., New Jersey (2006).

[40] Smoluchowski. *Contribution to the theory of electro-osmosis and related phenomena.* Bull. Int. Acad. Sci. Cracovie **1**, (1903), p. 184.

[41] H. A. Pohl. *Dielectrophoresis.* Cambridge Univ. Press, UK (1978).

[42] T. Müller, A. Gerardino, T. Schnelle, S. Shirley, F. Bordoni, G. DeGasperis, R. Leoni, G. Fuhr. *Trapping of micrometre and sub-micrometre particles by high-frequency electric fields and hydrodynamic forces.* J. Phys. D-Appl. Phys. **29**, (1996), p. 340.

[43] M. Trau, D. Saville, I. Aksay. *Assembly of colloidal crystals at electrode interfaces.* Langmuir **13**, (1997), p. 6375.

[44] S.-R. Yeh, M. Seul, B. I. Shraiman. *Assembly of ordered colloidal aggregates by electric-field-induced fluid flow.* Nature **386**, (1997), p. 57.

[45] A. Ramos, H. Morgan, N. Green, A. Castellanos. *AC electrokinetics: A review of forces in microelectrode structures.* J. Phys. D-Appl. Phys. **31**, (1998), p. 2338.

[46] N. Green, A. Ramos, A. Gonzalez, H. Morgan, A. Castellanos. *Fluid flow induced by non-uniform AC electric fields in electrolytic solutions on micro-electrodes. Part I: Experimental measurements.* Phys. Rev. E **61**, (2000), p. 4011.

[47] N. Green, A. Ramos, H. Morgan. *AC electrokinetics: A survey of sub-micrometre particle dynamics.* J. Phys. D-Appl. Phys. **33**, (2000), p. 632.

[48] H. Verheijen, M. Prins. *Reversible electrowetting and trapping of charge: Model and experiments.* Langmuir **15**, (1999), p. 6616.

[49] L. Minnema, H. Barneveld, P. Rinkel. *An investigation into the mechanism of water treeing in polyethylene high-voltage cables.* IEEE T. Electr. Insul. **15**, (1980), p. 461.

[50] G. Beni, S. Hackwood. *Electrowetting displays.* Appl. Phys. Lett. **38**, (1981), p. 207.

[51] K. H. Kang. *How electrostatic fields change contact angle in electrowetting.* Langmuir **18**, (2002), p. 10318.

[52] H. Lee, S. Yun, S. H. Ko, K. H. Kang. *An Electrohydrodynamic flow in AC electrowetting.* Biomicrofluidics **3**, (2009), p. 044113.

[53] S. H. Ko, H. Lee, K. H. Kang. *Hydrodynamic flows in electrowetting.* Langmuir **24**, (2008), p. 1094.

[54] F. Mugele, A. Klingner, J. Buehrle, D. Steinhauser, S. Herminghaus. *Electrowetting: A convenient way to switchable wettability patterns.* J. Phys.: Condens. Matter **17**, (2005), p. S559.

[55] F. Mugele. *Fundamental challenges in electrowetting: From equilibrium shapes to contact angle saturation and drop dynamics.* Soft Matter **5**, (2009), p. 3377.

[56] J.-C. Baret, M. M. J. Decre, F. Mugele. *Self-excited drop oscillations in electrowetting.* Langmuir **23**, (2007), p. 5173.

[57] J. Gray, R. Bonnecaze. *Rheology and dynamics of sheared arrays of colloidal particles.* J. Rheol. **42**, (1998), p. 1121.

[58] Y. L. Wu, D. Derks, A. van Blaaderen, A. Imhof. *Melting and crystallization of colloidal hard-sphere suspensions under shear.* Proc. Natl. Acad. Sci. U. S. A. **106**, (2009), p. 10564.

[59] J. Vermant, M. Solomon. *Flow-induced structure in colloidal suspensions.* J. Phys.-Condes. Matter **17**, (2005), p. R187.

[60] B. Ackerson. *Shear-induced order and shear processing of model hard-sphere suspensions.* J. Rheol. **34**, (1990), p. 553.

[61] B. Ackerson, N. Clark. *Shear-induced partial translational ordering of a colloidal solid.* Phys. Rev. A **30**, (1984), p. 906.

[62] B. Ackerson, P. Pusey. *Shear-induced order in suspensions of hard-spheres.* Phys. Rev. Lett. **61**, (1988), p. 1033.

[63] M. Haw, W. Poon, P. Pusey. *Direct observation of oscillatory-shear-induced order in colloidal suspensions.* Phys. Rev. E **57**, (1998), p. 6859.

[64] T. Solomon, M. Solomon. *Stacking fault structure in shear-induced colloidal crystallization.* J. Chem. Phys. **124**, (2006), p. 134905.

[65] R. L. Hoffman. *Discontinuous and dilatant viscosity behavior in concentrated suspensions. I. Observation of a flow instability.* Trans. Soc. Rheol. **16**, (1972), p. 155.

[66] X. Cheng, J. H. McCoy, J. N. Israelachvili, I. Cohen. *Imaging the microscopic structure of shear thinning and thickening colloidal suspensions.* Science **333**, (2011), p. 1276.

[67] C. Dekruif, E. Vanlersel, A. Vrij, W. Russel. *Hard-sphere colloidal dispersions - viscosity as a function of shear rate and volume fraction.* J. Chem. Phys. **83**, (1985), p. 4717.

[68] P. H. Walker, J. G. Thompson. *Some physical properties of paints.* P. Am. Soc. Test. Mater. **22**, (1922), p. 465.

[69] A. G. Emslie, F. T. Bonner, L. G. Peck. *Flow of a viscous liquid on a rotation disk.* J. Appl. Phys. **29**, (1958), p. 858.

[70] D. Meyerhofer. *Characteristic of resist films produced by spinning.* J. Appl. Phys. **49**, (1978), p. 3993.

[71] D. P. Birnie III, M. Manley. *Combined flow and evaporation of fluid on spinning disk.* Phys. Fluids **9**, (1997), p. 870.

[72] B. G. Higgins. *Film flow on a rotating disk.* Phys. Fluids **29**, (1986), p. 3522.

[73] A. Acrivos, M. J. Shah, E. E. Petersen. *On the flow of a non-Newtonian liquid on a rotating disk.* J. Appl. Phys **31**, (1960), p. 963.

[74] S. Wahal, A. Oztekin, D. E. Bornside, R. A. Brown, P. K. Seidel, P. W. Ackmann, F. T. Geyling. *Visualization of a gas flow instability in spin coating systems.* Appl. Phys. Lett. **62**, (1993), p. 2584.

[75] H. Furukawa, H. Tsutsui, K. Aoi, T. Watanabe, I. Nakamura. *Visual study of variations of flow patterns around a disk in a casing: Effects of edge of the disk.* J. Phys. Conf. Ser. **14**, (2005), p. 220.

[76] D. E. Bornside, C. W. Macosko, L. E. Scriven. *Spin coating: One-dimensional model.* J. Appl. Phys. **66**, (1989), p. 5185.

[77] N. Fraysse, G. M. Homsy. *An experimental-study of rivulet instabilities in centrifugal spin-coating of viscous Newtonian and non-Newtonian fluids.* Phys. Fluids **6**, (1994), p. 1491.

[78] T. Ohara, Y. Matsumoto, H. Ohashi. *The film formation dynamics in spin-coating.* Phys. of Fluids A **1**, (1989), p. 39937.

[79] V. Cregan, S. O'Brien. *A note on spin-coating with small evaporation.* J. Colloid Interf. Sci. **314**, (2007), p. 324.

[80] A. Münch, C. P. Please, B. Wagner. *Spin-coating of an evaporating polymer solution.* Phys. Fluids **23**, (2011), p. 102101.

[81] F. Melo, J. F. Joanny, S. Fauve. *Fingering instability of spinning drops.* Phys. Rev. Lett. **63**, (1989), p. 1958.

[82] S. Y. Heriot, R. A. L. Jones. *An interfacial instability in a transient wetting layer leads to lateral phase separation in thin spin-cast polymer-blend films.* Nature Mater. **4**, (2005), p. 782.

[83] D. B. Hall, P. Underhill, J. M. Torkelson. *Spin-coating of thin and ultrathin polymer films.* Polym. Eng. Sci. **38**, (1998), p. 2039.

[84] C.-C. Chang, C.-L. Pai, W.-C. Chen, S. A. Jenekhe. *Spin-coating of conjugated polymers for electronic and optoelectronic applications.* Thin solid films **479**, (2005), p. 254.

[85] T. Komikado, A. Inoue, K. Masuda, T. Ando, S. Umegaki. *Multi-layered mirrors fabricated by spin-coating organic polymers.* Thin Solid Films **515**, (2007), p. 3887.

[86] A. Oron, S. Davis, S. Bankoff. *Long-scale evolution of thin liquid films.* Rev. Mod. Phys. **69**, (1997), p. 931.

[87] P. Jiang, M. McFarland. *Large-scale fabrication of wafer-size colloidal crystals, macroporous polymers and nanocomposites by spin-coating.* J. Am. Chem. Soc. **126**, (2004), p. 13778.

[88] A. Mihi, M. Ocaña, H. Míguez. *Oriented colloidal-crystal thin films by spin-coating microspheres dispersed in volatile media.* Adv. Mater. **18**, (2006), p. 2244.

[89] C. Arcos, K. Kumar, W. González-Viñas, R. Sirera, K. M. Poduska, A. Yethiraj. *Orientationally correlated colloidal polycrystals without long-range positional order.* Phys. Rev. E **77**, (2008), p. 050402(R).

[90] M. Giuliani, W. González-Viñas, K. Poduska, A. Yethiraj. *Dynamics of crystal structure formation in spin-coated colloidal films.* J. Phys. Chem. Lett. **1**, (2010), p. 1481.

[91] L. Shereda, R. Larson, M. Solomon. *Local stress control of spatiotemporal ordering of colloidal crystals in complex flows.* Phys. Rev. Lett. **101**, (2008), p. 16.

[92] P. Ilg, M. Kröger, S. Hess. *Magnetoviscosity of semidilute ferrofluids and the role of dipolar interactions: Comparison of molecular simulations and dynamical mean-field theory.* Phys. Rev. E **71**, (2005), p. 031205.

[93] R. Usha, T. Götz. *Spinning of a liquid film from a rotating disc in the presence of a magnetic field - A numerical solution.* Acta Mech. **147**, (2001), p. 137.

[94] C.-K. Chen, D.-Y. Lai. *Weakly nonlinear stability analysis of a thin magnetic fluid during spin-coating.* Math. Probl. Eng. **2010**, (2010), p. 987891.

[95] B. Dandapat, G. Layek. *Spin-coating in the presence of a transverse magnetic field and non-uniform rotation: A numerical study.* J. Phys. D-Appl. Phys. **32**, (1999), p. 2483.

[96] R. Usha, B. Uma. *The role of induced air shear on the development of a conducting fluid film over a rough spinning disk in the presence of a transverse magnetic field.* Z. Angew. Math. Mech. **82**, (2002), p. 211.

[97] F. Zhi-Hui, H. Yan-Bing, S. Quan-Min, Q. Li-Fang, L. Yan, Z. Lei, L. Xiao-Jun, T. Feng, W. Yong-Sheng, X. Rui-Dong. *Polymer solar cells based on a PEDOT:PSS layer spin-coated under the action of an electric field* **19**, (2010), p. 038601.

[98] Y. Bertholet. *Measurement, optimization and multiscale modeling of silicon wafer bonding interface fracture resistance.* Ph.D thesis, Université Catholique de Louvain (2006) .

[99] Y. Han, D. Mayer, A. Offenhäusser, S. Ingebrandt. *Surface activation of thin silicon oxides by wet cleaning and silanization.* Thin Solid Films **510**, (2006), p. 175.

[100] A. Papra, N. Gadegaard, N. Larsen. *Characterization of ultrathin poly(ethylene glycol) monolayers on silicon substrates.* Langmuir **17**, (2001), p. 1457.

[101] M. Giuliani, M. Pichumani, W. González-Viñas. *Impact of electric fields on the speed of contact line in vertical deposition of diluted colloids.* Eur. Phys. J-Spec. Top. **192**, (2011), p. 121.

[102] G. Haller, T. Sapsis. *Where do inertial particles go in fluid flows?* Physica D **237**, (2008), p. 573.

[103] A. V. Delgado, F. González-Caballero, R. J. Hunter, L. K. Koopal, J. Lyklema. *Measurement and interpretation of electrokinetic phenomena (IUPAC technical report).* Pure Appl. Chem. **77**, (2005), p. 1753.

[104] R. Hayward, D. Saville, I. Aksay. *Electrophoretic assembly of colloidal crystals with optically tunable micropatterns.* Nature **404**, (2000), p. 56.

[105] A. Rogach, N. Kotov, D. Koktysh, J. Ostrander, G. Ragoisha. *Electrophoretic deposition of latex-based 3D colloidal photonic crystals: A technique for rapid production of high-quality opals.* Chem. Mater **12**, (2000), p. 2721.

[106] T. Hao. *Electrorheological fluids: The non-aqueous suspensions.* Elsevier Science Ltd. 2005 .

[107] Y. Hu, J. L. Glass, A. E. Griffith, S. Fraden. *Observation and simulation of electrohydrodynamic instabilities in aqueous colloidal suspensions.* J. Chem. Phys. **100**, (1994), p. 4674.

[108] E. Schäffer, T. Thurn-Albrecht, T. P. Russell, U. Steiner. *Electrohydrodynamic instabilities in polymer films.* Europhys. Lett **53**, (2001), p. 518.

[109] J. Yamanaka, H. Matsouka, H. Kitano, N. Ise. *Revisit to the intrinsic viscosity-molecular weight relationship of ionic polymers. I. Viscosity behavior of dilute suspensions of ionic polymer latices.* J. Colloid Interface Sci. **134**, (1990), p. 92.

[110] J. Yamanaka, H. Matsouka, H. Kitano, N. Ise, T. Yamaguchi, S. Saeki, M. Tsubokawa. *Revisit to the intrinsic viscosity-molecular weight relationship of ionic polymers. III. Viscosity behavior of ionic polymer latices in ethylene glycol/water mixtures.* Langmuir **7**, (1991), p. 1928.

[111] B. Ashok, M. Muthukumar. *Crossover behavior of the viscosity of dilute and semidilute polyelectrolyte solutions.* J. Phys. Chem. B **113**, (2009), p. 5736.

[112] G. Voronoi. *Nouvelles applications des parametres continus a la theorie des forms quadratiques. duesieme memoire: Recherches sur les paralleloderes primitifs paralleloderes primitifs.* J. reine angew. Math. **134**, (1908), p. 198.

[113] M. J. McDonald, A. Yethiraj, L. Y. Beaulieu. *A method to characterize structure and symmetry in low-resolution images of colloidal thin films.* Meas. Sci. Technol. **23**, (2012), p. 045606.

[114] T. Rehg, B. Higgins. *Spin-coating of colloidal suspensions.* AIChe J. **38**, (1992), p. 489.

[115] B. J. Ackerson, N. A. Clark. *Shear-induced melting.* Phys. Rev. Lett. **46**, (1981), p. 123.

[116] M. Pichumani, W. González-Viñas. *Customized spin-coating: Superparamagnetic colloids and magnetic fields.* Submitted to Langmuir (2012) .

[117] N. J. Wagner, J. F. Brady. *Shear thickening in colloidal dispersions.* Phys. Today **62**, (2009), p. 27.

[118] Y. L. Wu. *Control over colloidal crystallization by shear and electric fields.* Ph.D. thesis, Utrecht University (2007).

[119] E. Vermolen. *Manipulation of Colloidal Crystallization.* Ph.D. thesis, Utrecht University (2008).

[120] P. V. Braun, P. Wiltzius. *Electrochemically grown photonic crystals.* Nature **402**, (1999), p. 603.

[121] O. D. Velev, E. W. Kaler. *Structured porous materials via colloidal crystal templating: From inorganic oxides to metals.* Adv. Mater. **12**, (2000), p. 531.

[122] D. Joannopoulos. *Photonics: Self-assembly lights up.* Nature **414**, (2001), p. 257.

[123] D. J. Norris, Y. A. Vlasov. *Chemical approaches to three-dimensional semiconductor photonic crystals.* Adv. Mater. **13**, (2001), p. 371.

[124] Y. A. Vlasov, X. Z. Bo, J. C. Sturm, D. J. Norris. *On-chip natural assembly of silicon photonic bandgap crystals.* Nature **414**, (2001), p. 289.

Index

Summary

In this experimental work, the effects of the external fields on the colloidal phase transition from liquid phase to solid deposits (evaporative colloidal phase transition) have been investigated. The external fields are applied while the transition is in process. The experiments are performed with two different transition duration:

(a) In the experiments of long duration, the fluid is allowed to evaporate by exposing the colloidal dispersion (negatively charged polystyrene particles of diameter 1.3 μm dispersed in ultra pure water) to an environment at high temperature (63°C) and low humidity (below 2% RH). The colloidal dispersion is placed between the two vertical conducting substrates. Electric fields (DC) are of the order of 1 V/mm and they are applied perpendicularly to the substrates while the phase transition is in process. When the continuous phase evaporates, the contact line recedes. We measure the speed of the receding contact line for different initial concentrations (0.1%, 0.3% and 0.5% w/w, respectively) as well as for varying electric field. The dried deposits of colloidal particles are then correlated with the initial conditions and electric field strength of the respective experiment. To deepen the understanding of the three phase contact line in vertical deposition of colloids, the meniscus of a colloid is observed while the weak external field (AC) of the order of 1 V/mm and 1 Hz is applied. In this case, the working temperature is relatively low (room temperature) when compared to the previous set of experiments explained above and consequently the contact line does not recede during the measurement time. The applied field generates flows near the meniscus through electrokinetic and electrowetting mechanisms resulting in the formation of clusters of colloidal particles in the fluid matrix along the horizontal contact line. The clusters are separated by a well defined characteristic length and in our experimental conditions, they remain between 5 and 15 minutes.

(b) In the experiments of short duration (spin-coating), the fluid phase of the colloidal dispersion is made to evaporate in fractions of a second by pouring a volume of the dispersion over the spinning substrate (spinning rate is of the order of 1000 rpm). In the absence of the magnetic field, equivalent film thickness for different kinds of colloids (superparamagnetic and nonmagnetic, respectively) are compared. After that, external fields are applied while the dispersion is pipetted onto the spinning substrate. On the one hand, external magnetic fields up to 0.066 T are applied while spin-coating the dilute superparamagnetic colloidal dispersion (polystyrene coated magnetite of diameter 1–2 μm and SiO$_2$ coated magnetite of diameter 1.51 μm dispersed in ultra pure water, respectively). A spin-coating model is constructed by considering the evaporation of the fluid and the particulate characteristics of the spin-coated deposits. Morphological transition from sparse to submonolayer deposits (clusters) of superparamagnetic particles occurs. The magnetic field increases the effective viscosity of the dispersion through magnetic dipole interactions. On the other hand, to overcome the axial symmetry imposed by the spin-coating (in experiments with nonmagnetic particles of high initial concentration, 40% w/w), nonuniform alternating electric fields of the order of 0.1 kV/mm; frequency of the order of 1 kHz are applied while spin-coating the colloidal dispersion (SiO$_2$ particles of diameter 458 nm dispersed in 2-Pentanone) over the patterned conducting substrate. We conclude that the dielectrophoretic confinement of the dispersion affects the hydrodynamic flows resulting in a predefined direction for the colloidal deposits. Thus, the electric field breaks the axial symmetry.

Resumen

En este trabajo experimental, se han investigado los efectos que tienen los campos externos en la transición de fase coloidal de líquido a depósito sólido por evaporación. Los campos externos se aplican durante la transición. Los experimentos se han realizado con dos escalas temporales diferentes:

(a) En los experimentos de larga duración, se deja evaporar el fluido al exponer la dispersión coloidal (partículas de poliestireno cargadas de diámetro 1.3 μm dispersas en agua ultrapura) a un ambiente a alta temperatura (63°C) y baja humedad (menor que 2 % RH). La dispersión coloidal se dispone entre dos substratos conductores colocados verticalmente. Los campos eléctricos (DC) son del orden de 1 V/mm y se aplican perpendicularmente a los substratos durante la transición de fase. Cuando la fase continua se evapora, la linea de contacto retrocede. Se mide la velocidad de la linea de contacto para diferentes concentraciones iniciales (0.1 %, 0.3 % y 0.5 % m/m, respectivamente) así como para diversos campos eléctricos. Los depósitos de partículas coloidales se correlacionan con las condiciones iniciales y el campo eléctrico aplicado de los experimentos correspondientes. Para mejorar la comprensión de la linea de contacto en la deposición vertical de coloides, se observó el menisco de un coloide cuando se aplicaba un campo externo débil (AC) del orden de 1 V/mm y 1 Hz. En este caso, la temperatura de trabajo es relativamente baja comparada con la serie anterior de experimentos. En consecuencia, la linea de contacto no retrocede durante el tiempo de medida. El campo aplicado genera flujos cerca del menisco a través de mecanismos electrocinéticos y de electromojado que resultan en la formación de agregados de partículas coloidales a lo largo de la linea de contacto. Los agregados están separados por una distancia bien definida y, en nuestras condiciones experimentales, permanecen entre 5 y 15 minutos.

(b) En los experimentos de corta duración ("spin-coating"), la fase fluida de la dispersión coloidal se hace evaporar en fracciones de segundo al dejar caer un volumen determinado de la dispersión sobre el substrato giratorio (girando en el orden de 1000 rpm). En ausencia de campo magnético aplicado, se ha comparado el espesor equivalente de la capa para distintos tipos de coloides (superparamagnéticos y no magnéticos, respectivamente). A continuación se aplicaron campos externos mientras se pipeteaba la dispersión sobre el substrato. Por una parte, campos magnéticos de hasta 0.066 T se aplicaron durante el "spin-coating" de dispersiones coloidales superparamagnéticas (magnetita recubierta de poliestireno con diámetros entre 1 y 2 μm y magnetita recubierta de SiO_2 con un diámetro de 1.51 μm ambas dispersadas en agua ultrapura). Un modelo de "spin-coating" se ha construido considerando la evaporación del fluido y el carácter discreto de los depósitos coloidales. Se observa una transición morfológica desde depósitos muy poco densos a submonocapas con agregados de partículas superparamagnéticas. El campo magnético aumenta la viscosidad efectiva de la dispersión a través de interacciones dipolares. Por otra parte, para superar la simetría axial impuesta por el "spin-coating" (en experimentos con partículas no magnéticas a alta concentración, 40 % m/m), se han aplicado campos eléctricos alternos no uniformes del orden de 0.1 kV/mm y 1 kHz durante el proceso de "spin-coating" de la dispersión (partículas de SiO_2 con diámetros de 458 nm dispersados en 2-pentanona) sobre un substrato conductor litografiado. Concluimos que el confinamiento dielectroforético de la dispersión afecta los flujos hidrodinámicos resultando en una dirección privilegiada para los depósitos coloidales. Consecuentemente, el campo eléctrico rompe la simetría axial.